

# Search for (Higgs-like) bosons decaying into a pair of long-lived exotic particles in the LHCb experiment

THIS IS A TEMPORARY TITLE PAGE  
It will be replaced for the final print by a version  
provided by the service academique.

Thèse n.6178 2014  
Présentée le 02 Avril 2014  
à la Faculté des Sciences de Base  
Laboratoire de Physique des Hautes Energies 1  
Programme doctoral de Physique  
École Polytechnique Fédérale de Lausanne  
pour l'obtention du grade de Docteur ès Sciences  
par

Julien Edouard Rouvinet

acceptée sur proposition du jury:

Prof. Georges Meylan, président du jury  
Prof. Aurelio Bay, directeur de thèse  
Prof. Minh Quang Tran, rapporteur  
Dr. Victor Coco, rapporteur  
Dr. Maurizio Martinelli, rapporteur

Lausanne, EPFL, 2014





Marty McFly: *Hey, Doc, we better back up. We don't have enough road to get up to 88.*

Dr. Emmett Brown: *Roads? Where we're going, we don't need roads.*

– Back to the Future (1985)

Dedicated to my family and my friends



# Acknowledgements

Premièrement, je voudrais remercier le Professeur Aurelio Bay qui a dirigé ce travail de thèse. Merci de m'avoir apporté ton soutien et merci de m'avoir guidé avec beaucoup de patience tout au long de ces quatre années. J'ai toujours pu bénéficier de tes conseils et tu as toujours su trouver le temps pour m'aider et m'orienter. J'ai énormément appris de nos discussions! Ensuite, je remercie Victor Coco et Maurizio Martinelli d'avoir accepté la tâche de rapporteur ainsi que pour votre participation aux nombreuses réunions de notre groupe de travail au CERN. Merci spécialement à Victor pour le temps consacré à me guider, entre autres, à travers les méandres des programmes informatiques de l'expérience LHCb. Je souhaite également remercier tous les membres du groupe Exotica, grâce auxquels j'ai beaucoup appris lors de nos nombreux meetings. Merci aussi aux Professeurs Meylan et Tran d'avoir accepté de rejoindre le jury de cette thèse.

Je voudrais particulièrement remercier Pierre Jaton et Bastien Muster, mes collègues de bureaux et amis. Vous m'avez souvent remonté le moral et apporté du réconfort grâce à votre humour toujours très délicat! Travailler avec des amis est un véritable privilège.

Merci à Frédéric Blanc de m'avoir aidé à travers de longues discussions et de m'avoir appris les subtilités des statistiques, de DaVinci et de la physique des particules en général. En plus d'être un fin pédagogue, tu as toujours été disponible pour me donner un coup de main.

Je remercie enfin tous les membres du Laboratoire de Physique des Hautes Energies de l'EPFL, en particulier Erika Lüthi et Esther Hofmann qui m'ont aidé à surmonter les obstacles administratifs et qui avaient toujours un chocolat sous la main lorsqu'elles m'entendaient "pester" devant mon ordinateur. Merci aussi à Frédéric Dupertuis et à Raphaël Märki pour vos connaissances de Roofit. Bonne chance à vous deux pour la suite! Merci également à Stéphane Tourneur pour tes conseils et à Barinjaka Rakotomiarmanana pour nos parties de tennis! Merci à mes amis du "7 ème", Amaury Magnin et Valentin Hirschi pour votre aide.

Pour finir, je remercie mes parents de m'avoir toujours soutenu et surtout d'avoir su implanter chez moi la curiosité qui m'a mené jusqu'ici. Et enfin, un tout grand merci à Naïmi Kaiser pour ton incroyable soutien et pour ta patience.

*Lausanne, 24th February 2013*

J.E.R



# Résumé

Ce travail de thèse présente la recherche de particules à long temps de vie issues de la désintégration de bosons semblables au boson de Higgs. Les données enregistrées par l'expérience LHCb durant l'année 2011 correspondant à  $0.9 \text{ fb}^{-1}$  sont analysées. Cette recherche est motivée par de nombreux développements théoriques dépassant le cadre du Modèle Standard de physique des particules. Plusieurs de ces modèles sont présentés et utilisés comme base pour l'analyse. Le bruit de fond est identifié comme étant issu d'évènements contenant des paires de quark b. Les efficacités de sélections obtenues se situent dans la fourchette 0.1 à 0.7 % et aucun évènement ayant la topologie attendue n'a été mesuré. Des limites supérieures de sections efficaces de productions comprises entre 1 et 100 pb sont obtenues pour des masses de bosons comprises entre 100 et 125  $\text{GeV}/c^2$  et des particules à long temps de vie entre 5 et 50 ps et de masses entre 20 et 50  $\text{GeV}/c^2$ .

**Mots clés :** CERN, LHC, LHCb, Physique au delà du Modèle Standard, Particules à long temps de vie, Vertex Déplacés





# Abstract

This thesis work presents a search for pairs of long-lived exotic particles originating from the decay of Higgs-like bosons. The search is performed using LHCb data corresponding to an integrated luminosity of  $0.9 \text{ fb}^{-1}$ . This study is motivated by many theoretical developments, beyond the Standard Model of particles physics, that predict the existence of non-yet discovered particles with lifetimes larger than those of B-hadrons. An analysis based on several theoretical models is presented and the background contribution is identified to originate from b quarks events. Total selection efficiencies in the range 0.1 to 0.7 % are obtained. No evidence for an event with the expected topology is found. For Higgs-like bosons masses in the range 100 to 125  $\text{GeV}/c^2$ , for long-lived particles masses from 20 to 50  $\text{GeV}/c^2$  and for lifetimes from 5 to 50 ps, upper limits on production cross sections from 1 to 100 pb are obtained.

**Keywords :** CERN, LHC, LHCb, Physics beyond the Standard Model, Long-Lived Particles, Displaced Vertices



# Table of Contents

<b>Acknowledgements</b>	<b>v</b>
<b>Résumé</b>	<b>vii</b>
<b>Abstract</b>	<b>ix</b>
<b>Table of Contents</b>	<b>xii</b>
<b>List of Figures</b>	<b>xviii</b>
<b>List of Tables</b>	<b>xxi</b>
<b>1 Introduction</b>	<b>1</b>
<b>2 Standard Model and Beyond</b>	<b>3</b>
2.1 The Standard Model of Particle Physics: From Quantum Field Theory to Particles	3
2.2 Current shortfalls of the Standard Model	4
2.3 Beyond the Standard Model	6
2.4 Supersymmetry with R-parity violation and Baryon number violation	6
2.4.1 Bilinear <i>R</i> -parity Violation	7
2.5 Hidden Valley	8
2.6 More long-lived particles	9
2.7 Status of exotic searches	9
<b>3 The LHC and the LHCb Experiment</b>	<b>13</b>
3.1 CERN and Large Hadron Collider	13
3.2 The main experiments: ALICE, ATLAS, CMS and LHCb	15
3.2.1 ALICE	15
3.2.2 ATLAS	15
3.2.3 CMS	15
3.2.4 LHCb	16
3.3 LHCb Experiment	17
3.3.1 The Vertex Locator	17
3.3.2 The Magnet	18
3.3.3 The Silicon Trackers	20

## Table of Contents

---

3.3.4	The Outer Tracker . . . . .	21
3.3.5	The Ring Imaging Cherenkov 1 & 2 . . . . .	22
3.3.6	The Electromagnetic and Hadronic Calorimeters . . . . .	23
3.3.7	The Muon System . . . . .	26
3.3.8	The Trigger Systems . . . . .	26
3.3.9	Track Reconstruction . . . . .	28
3.3.10	Stripping . . . . .	29
3.3.11	Monte Carlo Simulation and Analysis Softwares . . . . .	30
<b>4</b>	<b>Search for Long-Lived Particles</b>	<b>31</b>
4.1	Monte Carlo event samples generation and descriptions of data sets . . . . .	31
4.2	Signal model analysis at four-vector level . . . . .	34
4.3	2011 data analysis . . . . .	36
4.3.1	Vertex reconstruction using PatPV algorithms . . . . .	36
4.3.2	Interaction with detector material . . . . .	39
4.3.3	Event preselection . . . . .	42
4.3.4	Higgs-like boson reconstruction . . . . .	46
4.4	Contribution to the detection efficiency and systematics effects . . . . .	50
4.4.1	Trigger efficiency studies . . . . .	51
4.4.2	Systematic uncertainties . . . . .	54
<b>5</b>	<b>Extractions of the Signal Yield from the 2011 Selected Events</b>	<b>57</b>
5.1	Fitting of key variables distributions . . . . .	57
5.1.1	The mass of the di-LLP . . . . .	58
5.1.2	$\Delta\phi$ angle between the two LLPs . . . . .	60
5.1.3	$1/\Sigma_R$ versus the di-LLP mass . . . . .	62
5.1.4	Analytical PDF fit of the mass of the di-LLP . . . . .	65
5.1.5	Simultaneous fit of the mass of the di-LLP . . . . .	68
5.2	ABCD Method . . . . .	72
5.3	The Neural Net method . . . . .	77
5.3.1	Di-LLP mass after NN selection . . . . .	79
5.3.2	NN applied to other signal models . . . . .	81
5.3.3	Production cross section upper limits . . . . .	82
5.4	Summary of the 2011 results . . . . .	83
<b>6</b>	<b>Conclusion</b>	<b>85</b>
<b>A</b>	<b>Appendix</b>	<b>87</b>
A.1	HLT2 Double line discussion . . . . .	87
	<b>Bibliography</b>	<b>94</b>
	<b>Curriculum Vitae</b>	<b>95</b>

# List of Figures

2.1	Particle content of the Standard Model. Left-hand side: Fermions. Right-hand side: Bosons. . . . .	4
2.2	Example of a LLP event in the Baryon Violating SUSY scenario. Here, the $h^0$ decays into two neutralino which are LLPs decaying into two jets containing heavy quarks b and c. . . . .	7
2.3	Example of a possible event in the two-light flavor regime (from [8]). . . . .	8
2.4	The 95% CL expected and observed upper limits from [10]. . . . .	10
2.5	The 95% CL lower limits from ATLAS SUSY Searches as given on the ATLAS public results web page. . . . .	11
3.1	Artistic representation of the LHC . . . . .	14
3.2	Illustration of the different facilities (LINAC, PS, SPS) and of the different experiments around the LHC ring. . . . .	14
3.3	The ALICE experiment . . . . .	15
3.4	Details on the ATLAS experiment . . . . .	16
3.5	Details on the CMS experiment . . . . .	16
3.6	The LHCb experiment with its different sub systems: The VELO (Vertex Locator), the RICH1 (Ring Imaging Cherenkov), the TT (Tracker Turicensis), the Magnet, the Inner and Outer Trackers, the RICH2, the first Muon Chamber, the Scintillating Pad Detector, the PreShower, the Electromagnetic CALorimeter, the Hadronic CALorimeter and the four last Muon Chambers. . . . .	17
3.7	Illustration of the VELO in the $(x,z)$ planes at $y = 0$ and $(x,y)$ . Notice the characteristics of the open and closed VELO positions. Dimensions of a VELO sensor are given. . . . .	18
3.8	Principal VELO sensor characteristics as presented in [11] . . . . .	19
3.9	View of the inside of an RF-foil. The $r$ and $\phi$ sensors are illustrated with different colors. The VELO is here in the fully-closed position. . . . .	19
3.10	Representation of the LHCb magnet. Units are given in mm. . . . .	20
3.11	The top picture displays a perspective view of one of the four boxes of the three IT stations arranged around the beam pipe. The bottom picture is a view in the $(x,y)$ plane of the second IT station. . . . .	21
3.12	Third layer of the TT sub detector. . . . .	21

## List of Figures

---

3.13	The left plot illustrates the arrangement of the three OT stations. The right plot represents the third OT station carried by its bridge into the open position. . .	22
3.14	Cherenkov angle versus particle momentum for different media and particle types. . . . .	23
3.15	(a) Schematic view of the side of RICH1. 3D model (b) and picture (c) of the detector. . . . .	23
3.16	Example of a LHCb event as seen by the RICH1 detector. . . . .	24
3.17	View of the ECAL not completely closed and outer, middle and inner type of ECAL modules on the right-hand side. . . . .	24
3.18	HCAL detector and, on the right-hand side, a schematic view of its internal cell structure. . . . .	25
3.19	(x,y) view of the SPD/PS and ECAL on the left and of the HCAL on the right. Only one fourth of the detector is depicted. Dimensions of the cells are given on the right-hand side of the pictures. . . . .	25
3.20	(y,z) view of the four last muon chambers on the left-hand side. The right-hand side illustrates a face view of one of the muon stations, each of them containing 276 muon chambers. . . . .	26
3.21	Overview of the L0 trigger. . . . .	27
3.22	Flow-diagram of the LHCb trigger system with the rate reduction given after each trigger stage. . . . .	28
3.23	Magnetic field amplitude in function of the z-coordinate (up) and different track types (bottom) . . . . .	29
4.1	Some properties of the Higgs boson determined at generator level: the transverse momentum (left) and the pseudorapidity distributions (right). Plots are normalized to unity. . . . .	34
4.2	Properties of the LLP determined at generator level: the pseudorapidity distributions (top, from [18]) (the cut at 1.8 indicated by a vertical line is not active for this plot), the transverse momentum (bottom left), and the flight length (bottom right). Distributions are normalized to unity. . . . .	35
4.3	Top: decay position of the LLP on the z axis. Bottom: radial position, linear and log scales. Distributions are normalized to unity. . . . .	36
4.4	Distributions of the transverse momentum (top left) and of the mass (top right). For the calculation, charged stable particles produced in the acceptance are selected when passing at less than 2 mm from the position of true decay point of the LLP. The number of particles selected by the procedure is given in the last plot. Distributions are normalized to unity (from [18]). . . . .	37
4.5	Mass of Higgs parent, obtained by combining the two LLP candidates reconstructed from charged particles, as seen in Figure 4.4. Distributions are normalized to unity (from [18]). . . . .	38

4.6	The LLP mass reconstructed using the particles falling in a $R=1$ cone around the LLP direction. All the stable particles have been used with the exception of neutrinos. Distributions are normalized to unity (from [18]). . . . .	38
4.7	Radial position of the reconstructed primary vertices for the 2011 data. . . . .	39
4.8	From preselected 2011 data, the longitudinal (left plot) and radial (right plot) coordinates (lab frame) of the reconstructed secondary vertices with at least four forward tracks, no backward tracks, and an invariant mass larger than $3.5 \text{ GeV}/c^2$ . The structure is due to the production of vertices in the detector material. . . . .	39
4.9	Like Figure 4.8, position of the reconstructed vertices in coordinates $(x,z)$ (lab frame). The data without global event cut are shown in the left plot, and with the cut in the right one. . . . .	40
4.10	Matter distribution inside the VELO for a 1 mm slice in $y$ , for the central (left) and forward (right) regions. The allowed area are colored in green (from [18]). . . . .	40
4.11	Distribution of $D_\phi$ in simulated events (black) and 2011 data selected for the displaced vertex analysis (red and blue). The vertical line corresponds to the cut applied in the analysis (courtesy from Pieter David). . . . .	42
4.12	Like Figure 4.9, after the matter veto. . . . .	42
4.13	Efficiency to find a (MC-true) LLP secondary vertex as a function of its distance from the PV. The left figure gives the efficiency as a function of the (true) longitudinal PV-RV distance $z^{true}$ . The right plot shows the true radial distance $R^{true}$ . The red points have the "matter veto" activated, to discard vertices produced by interactions of particles with the detector material. Here at least 6 charged particles to form the vertex are requested. . . . .	44
4.14	MC events compared to data results. Distributions of (top left) the number of tracks of the LLP candidate, (top right) the transverse momentum, (bottom left) the invariant mass, and (bottom right) the radial distance to the beam line in logarithmic scale are shown. Data and MC distributions are shown with unit normalization. The plots contain $121 \cdot 10^3$ events from data analysis, and about 1600 events of the special $b\bar{b}$ MC sample. Each plot has two LLPs per event. . . . .	45
4.15	Radial and longitudinal errors on the LLP vertex, provided by the vertex algorithm, for data and MC events. . . . .	46
4.16	Average error in $Z$ (left) and $R$ (right) versus number of tracks in the vertex. The difference between HV and BV seems associated with the quark composition of the decay of the LLP: HV contains only $b$ quarks, while BV produces also light quarks. . . . .	46
4.17	$\Delta\phi$ angle between the two LLP candidates for data and MC distributions normalized to unity. Black points are the data, $b\bar{b}$ MC events in red and BV and HV signal MC events in blue and green respectively. . . . .	47
4.18	Linear and log distributions of the distance of flight of the LLP candidates. Data in black, $b\bar{b}$ MC events in red and the BV signal in blue. Data and MC distributions normalized to unity. . . . .	47

**List of Figures**

---

4.19  $p_T$  distribution (left column), and invariant mass (right column) for the Higgs candidates. Result for MC signal and  $b\bar{b}$  events are shown with unit normalization. Plots at the bottom have log scale. Black dots are data, red:  $b\bar{b}$  distributions, blue: BV signal, and green: HV. . . . . 48

4.20 Reconstructed invariant mass  $M$ , transverse momentum  $p_T$ , number of tracks, and pseudorapidity of the single loose LLP candidates. The dots represent the data, the histogram is the result for the MC  $J/\psi$ . The distributions have been normalized to unity. The analysis requires an HLT2 Dimuon  $J/\psi$  positive decision. . . . . 53

4.21 Radial distance to the beam line of the reconstructed  $J/\psi$  with the requirement of the HLT2 DiMuon  $J/\psi$  positive decision. The dots represent the data, the histogram is the MC  $J/\psi$  prediction. The distributions have been normalized to unity. . . . . 54

5.1 Comparison of di-LLP invariant mass distributions for  $b\bar{b}$  MC events selected by increasingly stronger cuts. The grey (1 sigma) band corresponds to condition bb1, blue dots to bb2, and red squares to bb3. The distributions are normalized to one. The statistical uncertainties are correlated. . . . . 58

5.2 Results of the fit of the di-LLP invariant mass distribution for the data events selections given in Table 5.3, linear scale on the left, log scale on the right. The signal component is BV48, the background events are  $b\bar{b}$  MC events selected by the sets of cuts described in the text. The purple error rectangles are the statistical uncertainties propagated from of the original  $b\bar{b}$  events sample and the green rectangles represent the fit uncertainty. . . . . 59

5.3 Comparison of  $\Delta\phi$  distributions for  $b\bar{b}$  events selected by three different analysis conditions. The grey (1 sigma) band corresponds to condition bb1, condition bb2 is shown by blue dots, and bb3 by red squares. The distributions are normalized to one. The errors of the three distributions are correlated. . . . . 60

5.4 The  $\Delta\phi$  data distribution is fitted by a BV48 shape plus a background shape modeled from  $b\bar{b}$  MC events. The data points are shown in black, and the fitted signal component is the histogram in blue. The green and purple rectangles are the total fitted distribution. The purple is the statistical uncertainties propagated from the original  $b\bar{b}$  sample, the green portion is from the fit uncertainty. The three plots assume the background models corresponding to the  $b\bar{b}$  MC selections bb1, bb2, bb3, as described in the text. . . . . 61

5.5 Left: background (contour) and BV48 signal (points) in the (di-LLP mass ,  $1/\Sigma_R$ ) plane. Right: normalized distribution of the variable which combines di-LLP mass and  $1/\Sigma_R$ . The red squares are from  $b\bar{b}$  MC events, the histogram in blue from BV48. . . . . 62

5.6  $1/\Sigma_R$  distribution in the s1 scenario. The distribution on the right-hand side is given in logarithmic scale. Distributions have been normalized to one. . . . . 63



5.7	Fit of the of the variable which combines di-LLP mass and $1/\Sigma_R$ , for the three data events and $b\bar{b}$ events selections as given in Table 5.5. The signal component is from BV48. . . . .	64
5.8	Fit of the of the di-LLP mass for different BV48 model. Top right: BV48 10ps, top left: BV48 5ps, bottom right: BV48 15ps, bottom left: BV48 50ps. . . . .	65
5.9	Signal PDF from the addition of BV48 models with 5ps, 10ps, 15ps and 50ps neutralino lifetimes. . . . .	66
5.10	Fit of the data in the s2 scenario, used for background modeling. Two exponential functions are used. . . . .	66
5.11	Fit of the MC $b\bar{b}$ sample with the scenario bb1. Two exponentials are used and a signal component has been added to test the coherence of the method. NB and NS are respectively the number of background and signal events determined by the fit. . . . .	67
5.12	Result of the fit of the data after s4 selection using the distributions obtained in Figure 5.9 and 5.10. NB and NS are respectively the number of background and signal events determined by the fit. . . . .	67
5.13	Fit of the BV48 MC signal model di-LLP mass (up) and of the data (down) with the selection s2 used as background model. . . . .	68
5.14	Fit of the di-LLP mass for the data in the scenario s4. This is obtained simultaneously with the fits of Figure 5.13. . . . .	68
5.15	Number of signal events extracted from 2000 toy experiments with fixed $N_S^{Gen}$ signal and $N_B^{Gen}$ background events. . . . .	70
5.16	Gaussian fits of the pull distributions obtained from the simultaneous fits of 2000 toy experiments with $N_S^{Gen}$ number of signal events and $N_B^{Gen}$ number of background events. . . . .	71
5.17	Bi-dimensional distribution of the signal BV48 (blue boxes) and $b\bar{b}$ MC background (curves) in the (mass of LLP1, number of tracks in LLP2) plane. . . . .	73
5.18	Distributions of the invariant mass of the LLP1 for different selections on the number of tracks in LLP2. Left: MC events, right is data. The distributions are normalized to one. . . . .	73
5.19	Computed significance values for 200 background events and 5 signal events, as a function of the cuts on the mass of LLP1 and number of tracks of LLP2. The values are multiplied by 10. . . . .	74
5.20	Situation of one toy experiment, with 200 background events (black points) and 5 BV48 events (red rectangles). 4 signal events lie in the D region, and one signal event falls in B. . . . .	75
5.21	Input variables of the NN event classifier. . . . .	77
5.22	Input variables of the NN classifier after normalization. . . . .	78
5.23	Average error evolution during the NN training. . . . .	79
5.24	NN answer to the BV48 test sample (blue histogram), to the $b\bar{b}$ sample (red dashed) and to the data 2011 (dots) distributions. The distributions are normalized to unity. . . . .	79

**List of Figures**

---

5.25 Fraction of events selected above a given cut on the NN variable. The left plot shows the BV48 selection efficiencies indicated with blue triangles (use the right scale); the red open circles are the  $b\bar{b}$  MC events, and the black points correspond to the data (use the left scale). On the right figure, the results for BV48 and  $b\bar{b}$  as before, and also obtained with a NN trained with a background polluted by 4% signal events (dots slightly displaced on the right) are shown. . . . . 80

5.26 Mass and number of tracks of the LLP1 and di-LLP mass for BV48 events, after pre-selection (in black) and after a  $NN > 0.95$  cut (red dashed). . . . . 80

5.27 Left:  $b\bar{b}$  MC di-LLP mass is fitted by a double exponential. Right: the fit of the NN selected di-LLP candidates (dots with error bars). The result of the fit is shown by the purple curve, and the fitted signal by the 0.8 events contained in the blue histogram. . . . . 81

A.1 Mass of the reconstructed LLP for (top left) 2011 data events, (top right) BV48 events and (bottom left) special MC  $b\bar{b}$ . Difference between events selected by any HLT2 physical trigger line (HLT2\_phys) and events selected by the HLT2 double lines are illustrated. The distributions contain events selected by the double displaced vertex stripping line and are normalized to unity. . . . . 88

A.2 Same as in Figure A.1 for the number of tracks of the reconstructed LLP for (top left) 2011 data events, (top right) BV48 events and (bottom left) special MC  $b\bar{b}$ . . . . . 89

A.3 Same as in Figure A.1 for the radial distance to the beam line of the reconstructed LLP for (top left) 2011 data events, (top right) BV48 events and (bottom left) special MC  $b\bar{b}$ . . . . . 89

A.4 Same as in Figure A.1 for the transverse momentum of the reconstructed LLP for (top left) 2011 data events, (top right) BV48 events and (bottom left) special MC  $b\bar{b}$ . . . . . 90

A.5 Same as in Figure A.1 for the  $\Delta\phi$  angle between the pair of reconstructed LLPs for (top left) 2011 data events, (top right) BV48 events and (bottom left) special MC  $b\bar{b}$ . . . . . 90

A.6 Same as in Figure A.1 for the vertex position error in r of the reconstructed LLP for (top left) 2011 data events, (top right) BV48 events and (bottom left) special MC  $b\bar{b}$ . . . . . 91

A.7 Same as in Figure A.1 for the vertex position error in z of the reconstructed LLP for (top left) 2011 data events, (top right) BV48 events and (bottom left) special MC  $b\bar{b}$ . . . . . 91

# List of Tables

4.1	Summary of data and full simulated MC sets of events used in this study. Mass units are $\text{GeV}/c^2$ , lifetimes are given in ps. The last column gives the generator efficiency. . . . .	32
4.2	Parameters of the models considered in this study: B violating processes (BV), and Hidden Valley (HV). Mass units are $\text{GeV}/c^2$ . The LLP of the BV model is the $\tilde{\chi}_1^0$ , the $\pi_\nu^0$ for HV. In the case of BV, M1 and M2 correspond to the Pythia parameters RMSS(1) and RMSS(2), $\mu$ is RMSS(4) and $\tan\beta$ RMSS(5). A Higgs mass of $125 \text{ GeV}/c^2$ requires also RMSS(16) = 2300. The lifetime of the LLP is fixed by hand. HV masses and lifetimes are free, and then set by hand. . . . .	32
4.3	Cross section upper limits, in pb, valid for a LLP lifetime of 10 ps. Results as they are presented in [16], from the 2010 data set analysis. . . . .	33
4.4	Cross section upper limits in pb inferred from the results of the 2010 analysis presented in [16] with a Higgs-boson mass of $114 \text{ GeV}/c^2$ . . . . .	33
4.5	HLT2 and stripping configurations in 2011 for the selection of couples of LLPs. At least one candidate must be found outside the detector material. . . . .	43
4.6	Statistics at the input of the procedure for Higgs selection for the MC background sets. A positive decision from the HLT2 double trigger is required. . . . .	48
4.7	Number of events at different selection stages for data and MC background. MV stands for the matter veto. For the MC sample, the number of generated events is also given. Triggered means that one of the HLT2 physical lines must give a physical decision. The bottom part of the table is specifically for HLT2 comparison. Only the more restrictive conditions are presented here. . . . .	49
4.8	Number of events at different selection stages of the analysis (see Table 4.7), compared to MC predictions between brackets, assuming a pure $b\bar{b}$ background. . . . .	49
4.9	Number of data events selected for some values of $N_{min}^{track}$ and $M_{min}^{LLP1/2}$ (in $\text{GeV}/c^2$ ), and $\sigma_R^{max}$ , $\sigma_Z^{max}$ (in mm). The 7th column (MV) says that the material veto was active for only one or both candidate. Alternatively, the restriction applied on the radial position of the second vertices (in mm) is indicated. For each set of cuts, the LLP candidates have a minimum radial distance of 0.4 mm. $\epsilon^{BV48}(\epsilon^{HV10})$ is the efficiency in percent estimated from the analysis of BV48 (HV10) events. The events are requested to pass the HLT2 double trigger line and a cut of 2.8 radians is made on the angle $\Delta\phi$ formed by the pair of LLPs. . . . .	50

**List of Tables**

---

4.10 Contributions to  $\epsilon$  at different stages of the event selection, based on MC BV48 events and with the cuts given on line 6 of Table 4.9. . . . . 50

4.11 Total detection efficiency  $\epsilon$  for MC BV and HV models with selection cuts corresponding to line 6 of Table 4.9 given with statistical uncertainties. . . . . 51

4.12 Comparison between data and MC fraction of events which are selected by categories of HLT1 lines, for different analysis conditions. The three analysis have  $\sigma_R=0.1$  mm and  $\sigma_Z = 1$  mm. Analysis 1 has  $N_{min}^{track}=4$ , and  $M_{min}^{LLP}=4$  GeV/c<sup>2</sup>; 73kevents have been found in data and 23 MC. Analysis 2 has  $N_{min}^{track}=5$ , and  $M_{min}^{LLP}=4$  GeV/c<sup>2</sup> 52kevents data, and 15 MC. Analysis 3 has  $N_{min}^{track}=5$ , and  $M_{min}^{LLP}=6$  GeV/c<sup>2</sup> 39kevents data, and 0 MC. . . . . 52

4.13 Number of events at different stage of the analysis for the  $J/\psi$  MC sample and the 2011 Data. The HLT2DiMuonJPsi trigger line is used to filter the data events and a single loose candidate with  $N_{min}^{track}=4$ ,  $M_{min}^{LLP}=3$  GeV/c<sup>2</sup>,  $R_{min}^{LLP}=0.4$  mm (and  $\Sigma pT_{min}=3$  GeV/c) is reconstructed. Furthermore, the  $J/\psi$  is required to be prompt (ie to decay at a maximum radial distance  $R < 0.4$  mm). . . . . 52

4.14 Contributions to the error on the efficiency, assuming the BV48 model. . . . . 54

5.1 Different scenarii of cuts for the selection of events. In addition  $R > 0.4$  mm is imposed on both candidates and the requirement of a HLT2Double trigger line positive decision can be added. Cuts on  $\sigma_R$  and  $\sigma_Z$  are not applied except for s4 that requires  $\sigma_R < 0.05$  mm and  $\sigma_Z < 0.25$  mm. . . . . 57

5.2 Details of the different selections for  $b\bar{b}$  MC events. All HLT2 physical trigger lines have been activated, and  $\Delta\phi > 2$  is imposed. . . . . 60

5.3 Results of the fit of the di-LLP invariant mass. . . . . 60

5.4 Results of the fit of the  $\Delta\phi$  distribution of 243 data events with a signal component for BV48, and a background from  $b\bar{b}$  MC events, selected by the three sets of cuts described in the text. . . . . 62

5.5 Results of the fit of the of the variable which combines di-LLP mass and  $1/\Sigma R$ . For the fit 3, the  $b\bar{b}$  background was shifted by 2 channels, to compensate for the difference in the selection criteria. . . . . 63

5.6 Fit parameters determined from the addition of BV48 models with  $\chi$  lifetimes of 5, 10, 15 and 50 ps.  $mu1$  and  $mu2$  are the means of the two gaussian functions,  $sigma1$  and  $sigma2$  are their respective width,  $taum$  is the decay function slope and, finally,  $u$  is the fraction between the red and green curves drawn in Figure 5.9 . . . . . 65

5.7 Fit parameters determined for the data in the scenario s2. Two exponential functions are used,  $tau$  and  $tau2$  being their respective slopes.  $f$  is the fraction between the two functions. . . . . 66

5.8	Fit parameters determined by the simultaneous fit of the BV48 signal sample in scenario s3, the background model from data s2 and the data s4. $\mu_1$ and $\sigma_1$ are the mean and width of the signal PDF, $\tau_{sum}$ being the slope of its decay function. $\tau_1$ is the slope of the first background exponential and $\tau_2$ is the ratio between it and the second exponential slope. $f$ is the ratio between the two background exponentials. $N_{BV}$ is the number of events in the fit of the signal component and $N_{Back}$ is the computed number of events in the background fit. $N_S$ and $N_B$ are respectively the extracted number of signal and background events found in the data s4. . . . .	69
5.9	Results of the simultaneous fits for different BV MC models. $N_S$ and $N_B$ are respectively the extracted number of signal and background events found in the data s4. . . . .	69
5.10	Total selection efficiency (in [%]) for different BV MC models, with s4 selections and for a di-LLP mass between 20 and 120 GeV/c <sup>2</sup> and upper limits on production cross sections at 95 % CL from the results of the simultaneous fits. . . . .	70
5.11	Number of events in the four regions for the toy experiment of Figure 5.20. . . . .	74
5.12	Number of events in the four regions, averaged over 1000 toy experiments. . . . .	75
5.13	Upper limits for cross section times branching fraction assuming various theoretical models. $\epsilon$ is the total selection efficiency. Upper limits are computed at 95 % CL with 21% total systematic uncertainty. . . . .	76
5.14	Same as in Table 5.13 for the complementary couple of variables. . . . .	76
5.15	Number of events used in the different samples, $N_{gen}$ , and selected by s3, $N_{s3}$ . $\epsilon_{gen}$ is the generator efficiency for the MC samples in %. $\epsilon_{s3}$ is the fraction $N_{s3}/N_{gen}$ , also in %. Finally, $\epsilon_{MC} = \epsilon_{gen} \times \epsilon_{s3}$ . . . . .	81
5.16	Fraction (in %) of MC signal and 2011 data events selected by a $NN > 0.85$ cut. $N_S$ is the number of signal events from the fit of the di-LLP invariant mass distribution. The last column is the corresponding $\chi^2/NDoF$ . The MC and data sets are pre-selected under s3 conditions. . . . .	82
5.17	Upper limits for cross section times branching fraction assuming various theoretical models. $\epsilon$ is the total selection efficiency, $N_S$ the number of signal events from the di-LLP mass fit. A 21% total systematic uncertainty is assumed. . . . .	82
5.18	Upper limits for cross section times branching fraction assuming various theoretical models. $\sigma_{max}^{fit}$ is the upper limit from the simultaneous fit, $\sigma_{max}^{ABCD}$ from the ABCD method and $\sigma_{max}^{NN}$ from the neural network, computed at 95% CL. . . . .	83



# 1 Introduction

This work presents the search for pairs of exotic Long-Lived Particles (LLP) produced by the decay of Higgs-like bosons, using data collected by the LHCb experiment in 2011. Various theoretical models beyond the Standard Model of particle physics predict the existence of new exotic particles with lifetimes larger than those of B-hadrons.

Chapter 2 presents an overview of different classes of models along with a very brief description of the Standard Model. References towards previous works addressing those theoretical developments are given with a summary of recent searches performed by other CERN experiments.

Chapter 3 describes the CERN organization and the LHC complex hosting the world biggest particles physics experiments. The LHCb experiment is described in details: its sub-detectors, the trigger system and the software tools that have been developed for the analysis are presented.

Chapter 4 describes the theoretical models considered as well as the strategy developed to separate interesting events with LLP candidates from the expected background. A study of the main characteristics of the expected topologies is made based on simulated Monte Carlo events. A full description of the selection procedure and of the algorithms used to reconstruct displaced vertices corresponding to the decay positions of the expected LLP are given. Different selections with their respective efficiencies are presented as well as the background estimate.

Chapter 5 regroups a collection of statistical methods used to extract physical informations from the previously selected events. Among those approaches, different fitting procedures of the key variables distributions are discussed. Then, an attempt to quantify the signal and

## **Chapter 1. Introduction**

---

background yields is made using an "ABCD" method. Finally, an example of an event classifier based on a neural network is made. Those different methods give results that are used to compute upper limits on production cross sections for different set of theoretical models.

This thesis work is directly related to the work of Dr. Neal Gauvin, presented in [1] which set up the path towards exotic particles searches at LHCb.



## 2 Standard Model and Beyond

An introduction to the Standard Model of particle physics (SM) is given in this chapter. Its limitations are the motivation that leads to new theories including exotic particles with significant lifetimes. Two classes of models beyond the SM are presented. Finally, the current status of the search for long-lived particles is addressed.

### 2.1 The Standard Model of Particle Physics: From Quantum Field Theory to Particles

During the 20th century, the developments of quantum physics and of special and general relativity lead the way to the understanding of the structure of matter as well as the interaction between the microscopic constituents of the Universe. The combination of quantum mechanics and special relativity gives rise to a complete and elegant mathematical description of space-time, called quantum field theory. This description is based on symmetry principles that drive the Lagrangian formulation of the theory. Its formulation should respect the special relativity postulate of invariance of the speed of light and the four-dimensional nature of space-time. It is therefore implied that the theory must respect the Poincaré symmetry. Then, by quantization, it is possible to write down the equations of motion of the large variety of fields/particles known to this day.

In parallel to these theoretical considerations, numerous experiments showed the existence of a wide panel of atoms (over 90) as well as the existence of many other particles, like electrons and photons. Noting a certain regularity in the relative weight of these atoms, the discovery of the electron by Thomson, of X-rays by Rontgen as well as the discovery of radioactivity, an unified description had to be formulated, taking into account the discovery of the positron, the antiparticle of the electron.

Born from this context, the Standard Model of particle physics is a relativistic quantum field theory which describes three of the four fundamental interactions of Nature and the elementary particles that undergo these interactions. This model is a gauge theory which is in

## Chapter 2. Standard Model and Beyond

extremely good agreement with the present (beginning of 2014) experimental results. The SM gauge group is:

$$G_{SM} = SU(3)_c \otimes SU(2)_L \otimes U(1)_Y \quad (2.1)$$

$SU(3)_c$  is the group representing the strong interaction, and the index  $c$  stands for *color* which corresponds to the strong charge.  $SU(2)_L \otimes U(1)_Y$  is the group corresponding to the electroweak interaction, which unifies the weak and the electromagnetic forces.

Two different groups of particles can be found; the fermions divided into quarks and leptons and the bosons that mediates the electromagnetic (through the photon), the weak (through the boson  $Z^0$  and the  $W^\pm$ ) and the strong (through the gluons) forces. For each particle it exists a corresponding antiparticle.

	Particle	Mass [MeV/c <sup>2</sup> ]
Leptons	e <sup>-</sup>	0.511
	ν <sub>e</sub>	<3 · 10 <sup>-6</sup>
	μ <sup>-</sup>	105.6
	ν <sub>μ</sub>	<0.19
	τ <sup>-</sup>	1777
	ν <sub>τ</sub>	<18.2
Quarks	u	1.5 - 3.3
	d	3.5 - 6.0
	c	1160 - 1340
	s	70 - 130
	t	171.2 ± 2.1 · 10 <sup>3</sup>
	b	4130-4370

	Particle	Interaction	Mass [GeV/c <sup>2</sup> ]
Bosons	g	strong	0
	γ	electromagnetic	0
	W <sup>±</sup>	weak	80.4
	Z <sup>0</sup>		91.2
	graviton	gravitational	0

Figure 2.1: Particle content of the Standard Model. Left-hand side: Fermions. Right-hand side: Bosons.

Details on the mass and properties of those fundamental constituents can be found in [2].

In addition to the particles and interactions aforementioned, a new type a field (and particle) to produce mass terms for the three gauge bosons, and also to fermions has to be introduced. This Higgs mechanism is on the verge to be confirmed thanks to the recent (4th of July 2012) discovery of a potential candidate for the Higgs boson, at CERN by both ATLAS and CMS experiments. For an overview of the SM, see [3].

## 2.2 Current shortfalls of the Standard Model

The SM has been able to explain, with a unbelievable level of accuracy, all the results obtained in experimental particle physics during the last century and also recently by the LHC. Nevertheless, it contains a certain number of limitations, some of these being of theoretical matter but also coming from observations. The principal issues are discussed in the following.

### **Hierarchy problem and Fine-Tuning**

The hierarchy problem arises when comparing the strength and scale between interactions. One should better consider that there exists many hierarchy problems. For example, the weak interaction is  $10^{32}$  times stronger than gravity. This can be translated into the question of the Higgs boson mass being much lighter than the Planck scale, due to cancellation between quadratic radiative corrections and bare mass. These quantum contributions must be very well adjusted. These kinds of improbable adjustments are called *fine-tuning*.

Fine-tuning is a problem in the sense that it seems unnatural that some fundamental parameters of the SM must acquire a very precise value that can only be deduced from experimental evidence and not computed from the fundamental principles of the theory. Extensions of the SM such as Supersymmetry bring mechanisms that allow to understand those precise cancellations rather than by an ad-hoc experimental tuning. In that context, these extensions appear as being more *fundamental*.

### **Dark Matter and Dark Energy**

Only taking into account luminous matter cannot explain the observed rotational speed of the galaxies, when assuming that the laws of General Relativity are correct. To explain the data, a large amount of "invisible" matter must have a gravitational effect on galaxies. This so-called "dark" matter was first postulated in 1932 by Jan Oort and in 1933 by Fritz Zwicky to account for evidence of "missing mass" in the orbital velocities of galaxies in clusters. Cosmologists think that dark matter is composed primarily of a non-yet characterized type of subatomic particles missing from the SM zoo. It is believed that this type of matter makes up to 21.4% of the total energy of the Universe. Supersymmetric or Hidden Valley theories, for instance, introduce potential dark matter candidates. Those candidates undergo gravitational interaction while being "transparent" to the other type of interactions, making them difficult to detect.

On the other hand, cosmological data indicates that, from supernovae observations, the Universe is presently undergoing an accelerated expansion postulated to be due to the existence of a "dark" energy making up 74.2% of the total energy density of the Universe. These considerations show that the baryonic matter described by the SM constitutes only 4.4% of the energy content of the Universe.

### **Incapacity to include gravitation**

Numerous efforts have been made to try to include the gravitational interaction to the Standard Model. Nevertheless, no one has been able to formulate a quantum field theory that consistently includes the four fundamental forces of Nature. The Standard Model does not provide a complete description of all known physical phenomena, neither explains the early universe, close to the Big Bang, when gravity plays a dominant role with respect to the other interactions.

The most famous theory that bounds General Relativity with quantum field theory is String Theory, whose formulation lies also on Supersymmetric principles.

### 2.3 Beyond the Standard Model

In an attempt to complete and take into account the current limitations of the Standard Model of particle physics, theoreticians have developed numerous models. Some of the most popular are based on the generalization of the Poincaré group called Supersymmetry (abbreviated SUSY). A certain class of SUSY models are described here, because the phenomenology they imply leads to the existence of new particles with lifetimes compatible with decays inside the Vertex detector of the LHCb experiment. Another class of popular models that theoreticians have developed are Hidden Valley models. This name comes from analogy with a valley hidden from another by a mountain, a barrier of potential in the theory. The phenomenology predicted is quite comparable to the one aforementioned.

### 2.4 Supersymmetry with R-parity violation and Baryon number violation

Supersymmetry is a very popular class of models based on a symmetry relating fermions and bosons, through a new operator (or more)  $Q$ :

$$Q|Boson\rangle = |Fermion\rangle \quad Q|Fermion\rangle = |Boson\rangle \quad (2.2)$$

In the supersymmetric extensions of the SM, each known fundamental particle fits into a supermultiplet and has a superpartner with a spin different by a half unit. The spin-0 superpartner names correspond to their SM partner names plus a "s" prefix: selectron, squark, slepton, ... Spin- $\frac{1}{2}$  superpartners have SM names plus a "ino" suffix: higgsino, zino, wino, ...

This principle gives birth to a large number of phenomenologies depending on the chosen mechanism of symmetry breaking. Numerous references towards the main principles of SUSY are available, see for example [4] for a nice review of its fundamentals. A new symmetry, named  $R$ -parity, is introduced forbidding all of the baryon and lepton number violating terms. But this symmetry is not imposed by the data and models as the one presented hereafter exploit this opportunity. Moreover, baryon number and lepton number violations are required by baryogenesis (together with C and CP violations) ([5]).

2.4.1 Bilinear R-parity Violation

The simplest implementation of SUSY is the Minimal Supersymmetric Standard Model (MSSM) (for details see for example [6]). It constitutes the minimal declination of the SUSY principle while still incorporating its attractive features, such as gauge coupling unification. This framework has nevertheless taken a large draw-back from recent measurements at the LHC. But its R-parity violating extension is still valid when taking into account the past year results. The possibility for the lightest superparticle to decay into SM particles, *de facto* violating the R-parity symmetry through baryon or lepton number violation gives birth to a new interesting phenomenology. While this R-parity violation leaves the theory without a dark matter candidate (except when lifetimes of the Lightest SuperParticle are sufficiently long), it helps the theory explain some features of the baryogenesis (see for example [5]). R-parity violation must be introduced with care, to still insure the stability of the proton. Following the simple description presented in [7], it is possible to introduce the Lagrangian term:

$$W_{\Delta B \neq 0} = \frac{1}{2} \lambda_{ijk} U_i D_j D_k \tag{2.3}$$

where the indices  $i, j, k$  run over the three generations of fermions. This term is responsible for the baryon number violation (a similar term can be added for the lepton number violation). To prevent proton decay, lepton or baryon violation terms must be added without one another. The simplest model of this kind is called bilinear R-parity violation (BRPV or simply BV in the following). This model implies that R-parity violating processes will dominantly involve fermions of the third generation, in particular the bottom quark ([7]).

In the context of BV, neutralinos are the Long-Lived Particles (LLPs). An event topology is shown in Figure 2.2, with an Higgs decaying into two LLPs. The LLPs decay into six jets. Typical values in BV are  $m(h^0) \geq 100 \text{ GeV}/c^2$ ,  $m(\chi) \geq 20 \text{ GeV}/c^2$  and lifetimes  $\tau \geq 1 \text{ ps}$ .

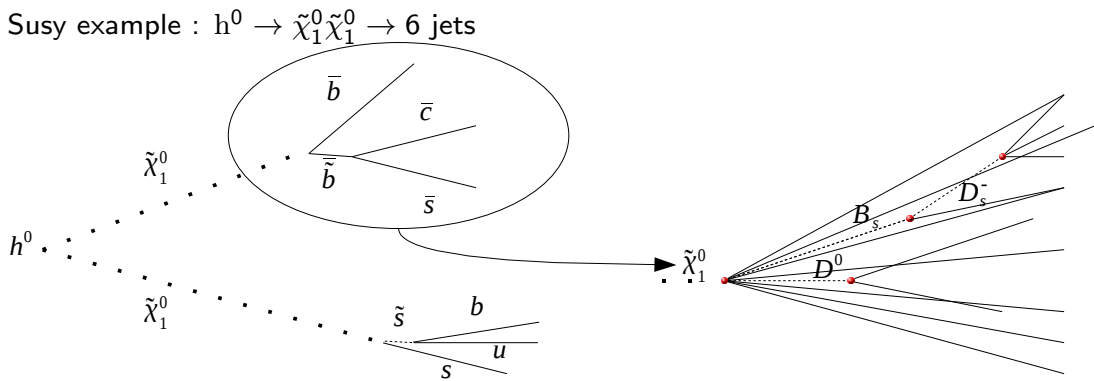


Figure 2.2: Example of a LLP event in the Baryon Violating SUSY scenario. Here, the  $h^0$  decays into two neutralino which are LLPs decaying into two jets containing heavy quarks b and c.

## 2.5 Hidden Valley

Arising from many top-down theories, for example string-theory, the hidden-valley scenario is well motivated and consistent with most methods for solving the hierarchy problem. Still consistent with data, its complex phenomenology usually predicts the existence of massive particles with lifetimes that can be in the range 1 to 100 ps. Reviews of its generic properties can be found in [8] and [9].

These models are created by adding to the SM gauge group  $G_{SM}$  a non-abelian group  $G_\nu$ , giving birth to new particles ("v-particles") charged under  $G_\nu$  and neutral under  $G_{SM}$ . SM particles are neutral under the  $G_\nu$  group. Interactions between SM fields and the new particles are allowed by higher dimension operators. The v-particles assemble themselves into  $G_\nu$ -neutral "v-hadrons" that can decay into gauge invariant combinations of SM particles with observable lifetimes.

A generic signal model including several long-lived v-hadrons that can generate displaced vertices through heavy flavor decay channels is proposed in [8]. A simple v-model obtained by adding a  $U(1) \times SU(n_\nu)$  gauge group to the SM, implying the existence of two v-quark flavors, U and C is presented. Three v-pions are created,  $\pi_\nu^\pm$  and  $\pi_\nu^0$ . The later can decay, for example into a  $b\bar{b}$  pair if its mass is below the  $ZZ$  mass threshold and produce a displaced vertex as illustrated in Figure 2.3.

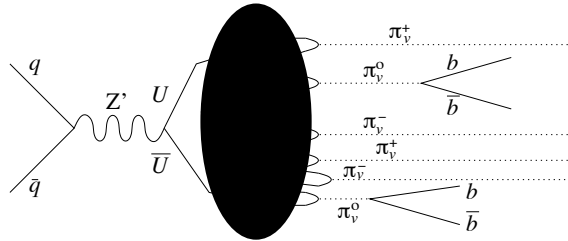


Figure 2.3: Example of a possible event in the two-light flavor regime (from [8]).

The dominant signal exhibits multiple pairs of b-jets from  $\pi_\nu^0$  decays plus missing energy from  $\pi_\nu^\pm$ .

As explained in [9], the Higgs boson would possibly decay through  $h^0 \rightarrow \pi_\nu^0 \pi_\nu^0 \rightarrow b\bar{b}b\bar{b}$  with a significant branching ratio.

To include these phenomenologies in the present study, an example of Hidden Valley model, named HV10, has been considered with  $m_{\pi_\nu^0} = 35 \text{ GeV}/c^2$ ,  $\tau_{\pi_\nu^0} = 10 \text{ ps}$  and  $m_h^0 = 120 \text{ GeV}/c^2$ .

## 2.6 More long-lived particles

Many other models imply the existence of non-yet discovered exotic long-lived particles. The interested reader is referred to [1] to find more informations and more references towards this thriving subject.

## 2.7 Status of exotic searches

Before summarizing the recent results published by ATLAS and CMS, it is worth pointing out their different sensitivities. ATLAS is focussing on models predicting LLPs with low masses, around  $20 \text{ GeV}/c^2$ , a high number of tracks (many jets) and a lot of muons. The considered high lifetimes imply displaced vertices at meter-long distances. CMS is more suited for searches of LLPs with low lifetimes and high masses, involving displaced lepton pairs and jet pairs with transverse momentum greater than  $60 \text{ GeV}/c$ . Those two experiments encounter a very hard triggering problem for low energy processes. Multiple clustered vertices appear confusing for them.

The CMS experiment has performed several searches for heavy long-lived particles. One recent example can be found in [10]. A search for long-lived particles has been performed with the 2012 proton-proton collisions at 8 TeV corresponding to an integrated luminosity of  $18.6 \text{ fb}^{-1}$ . In the considered models, the long-lived particles decay to quark-antiquark pairs. The presented results are consistent with the SM expectations and the CMS collaboration has been able to set upper limits on the product of cross section times branching fraction for a scalar particle,  $H^0$ , in the mass range 200 to 1000  $\text{GeV}/c^2$ , mass range being higher than the one considered in this thesis. The  $H^0$  is decaying into a pair of  $\chi^0$  in the mass range from 50 to 350  $\text{GeV}/c^2$  which then decay into a quark-antiquark pair. The obtained results are that for a  $H^0$  mass of 400-1000  $\text{GeV}/c^2$ , for  $\chi^0$  masses of 50-350  $\text{GeV}/c^2$  and for lifetimes of  $0.1 < c\tau < 200 \text{ cm}$ , the upper limits are typically 0.3 to 100 fb. For  $H^0$  mass of 200  $\text{GeV}/c^2$ , the limits are in the range 0.08 to 0.3 pb for  $\chi^0$  lifetimes of 0.2 to 10 cm (which is roughly compatible with the parameters considered in this thesis). These results are illustrated in Figure 2.4.

The ATLAS experiment also produced interesting results on the subject from collisions at 7 and 8 TeV, using an integrated luminosity of 4.6 to 22.9  $\text{fb}^{-1}$ . Those results are summarized on Figure 2.5.

The LHCb experiment has as crucial role to play on setting upper limits on a complementary range of low masses and especially lifetimes from 1 to 100 ps. Thanks to its very unique vertex detector and to its trigger system interesting results can help physicists to complete their search of new fundamental processes. The results obtained with the 2010 data are presented in Chapter 4.

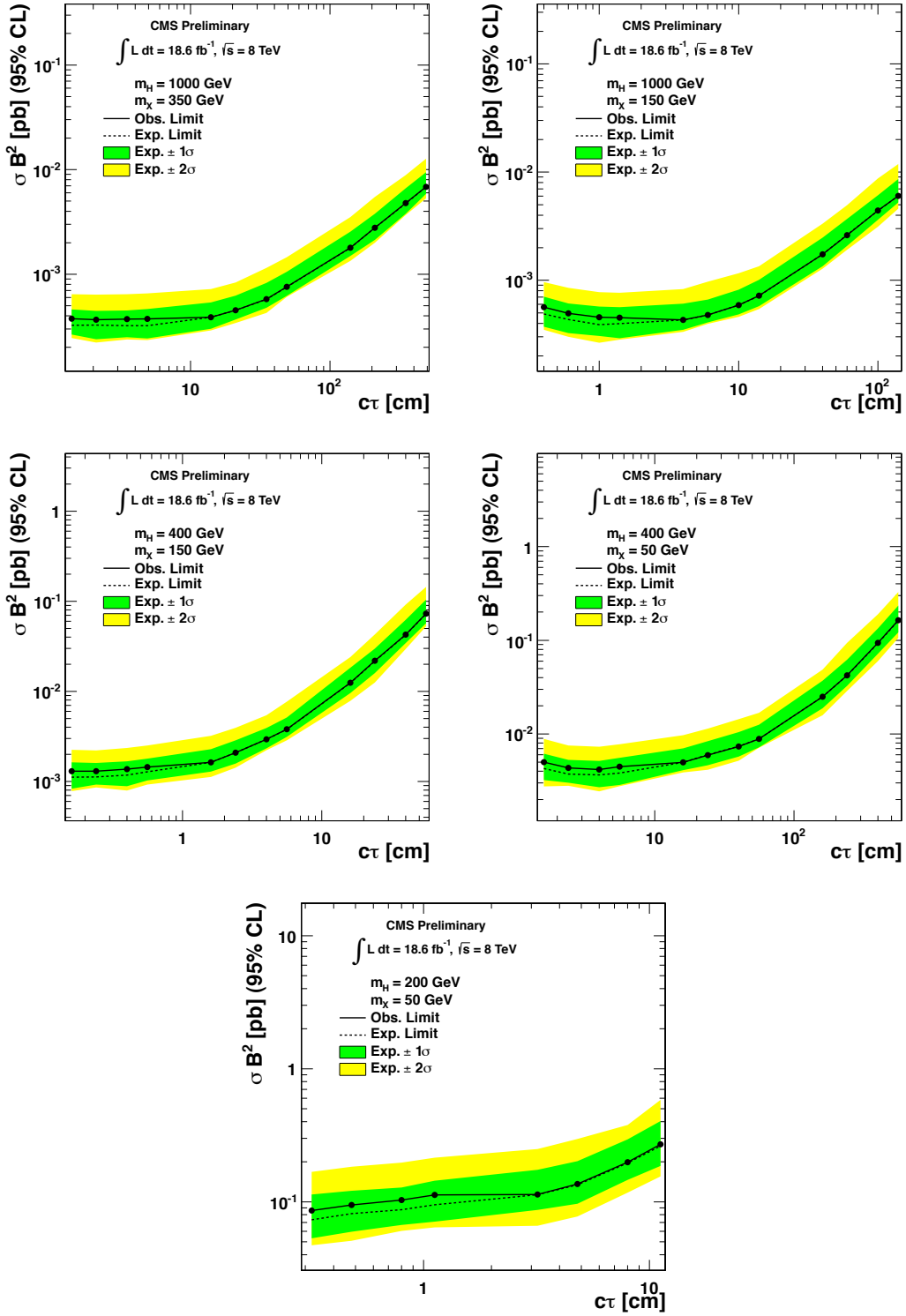


Figure 2.4: The 95% CL expected and observed upper limits from [10].



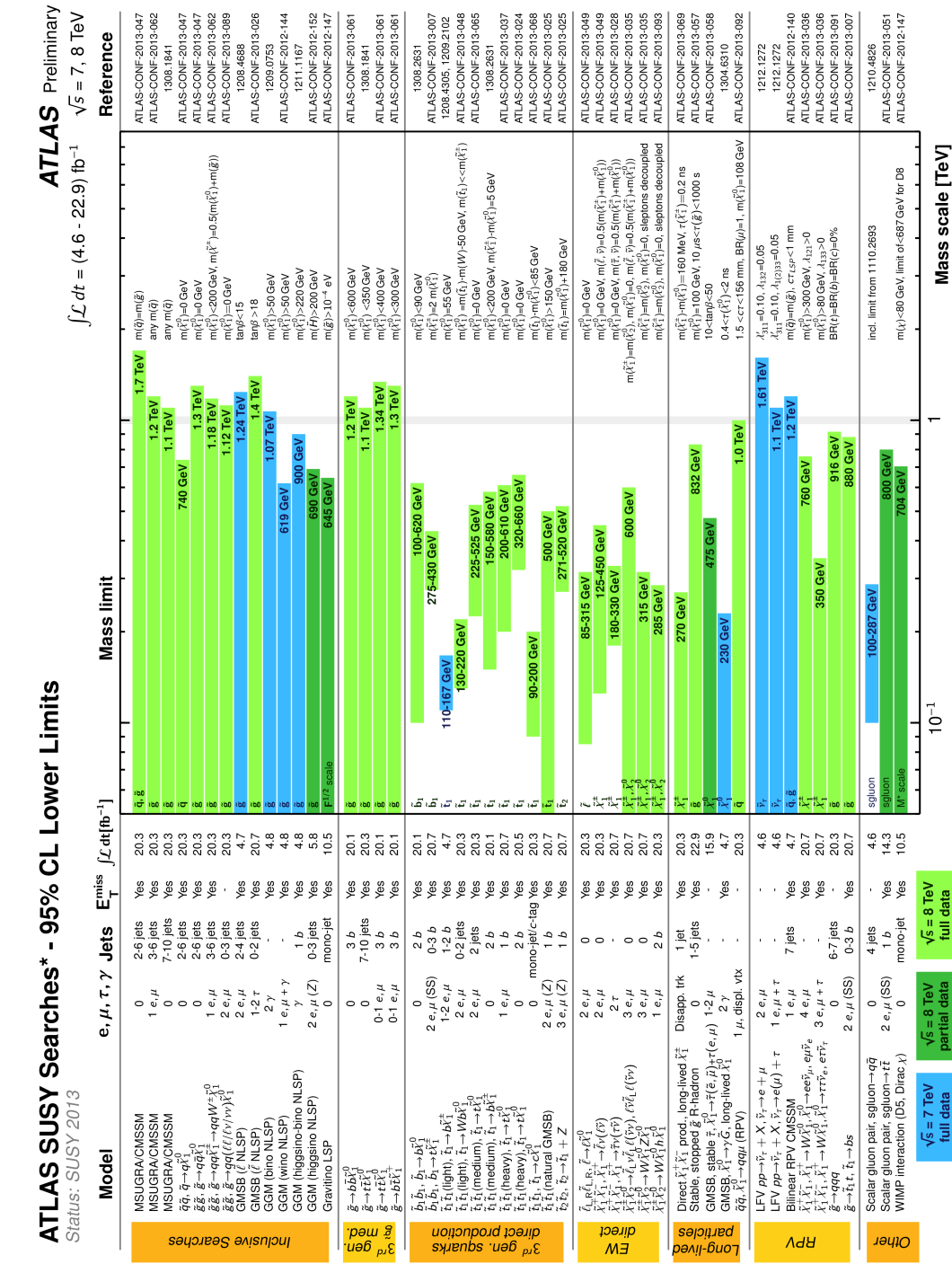


Figure 2.5: The 95% CL lower limits from ATLAS SUSY Searches as given on the ATLAS public results web page.



## 3 The LHC and the LHCb Experiment

This chapter presents a description of the Large Hadron Collider (LHC) as well as the four main experiments hosted by the European Organization for Nuclear Research (CERN) in Geneva, Switzerland. More details are given on the LHCb experiment which is the detector used within this thesis. Descriptions of its sub-detectors, the data acquisition and trigger systems are presented.

### 3.1 CERN and Large Hadron Collider

The European Organization for Nuclear Research (CERN) was founded in 1954 to be a world-class fundamental physics research organization in Europe. The laboratory site is located across the Franco-Swiss border in Meyrin, near Geneva in Switzerland. In 2014, the organization is constituted of twenty European states and 7 non-European observer states. About 2'400 full-time employees and 1'500 part-time employees are directly working for the organization while more than 10'000 visiting scientists are taking part in the different research projects that are conducted to investigate the fundamental Nature of the Universe. This represents about 113 different nationalities and about 608 different universities.

The major part of the CERN activities are devoted to the Large Hadron Collider (LHC). Today, the LHC is the highest energy particle collider in the world producing collisions between bunches of 115 billion of protons. Up to the year 2013, the energy reached is 8 TeV in the center of mass (13 TeV are expected in 2015). The LHC is a synchrotron of 27 km of circumference located in a tunnel, more than 100 m underground.

Eight points of interaction are distributed around the LHC ring and four of them are occupied by big detectors: ATLAS, CMS, ALICE and LHCb. LHCf and TOTEM are located near, respectively, ATLAS and CMS.

LHCf (Large Hadron Collider forward) uses forward generated particles to simulate and study

**Chapter 3. The LHC and the LHCb Experiment**

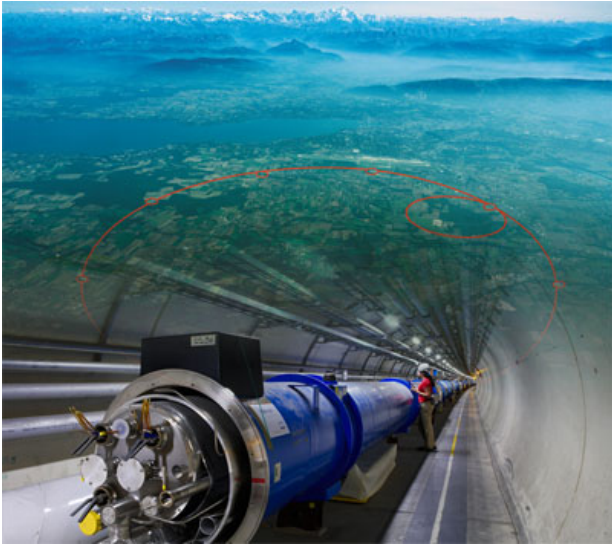


Figure 3.1: Artistic representation of the LHC

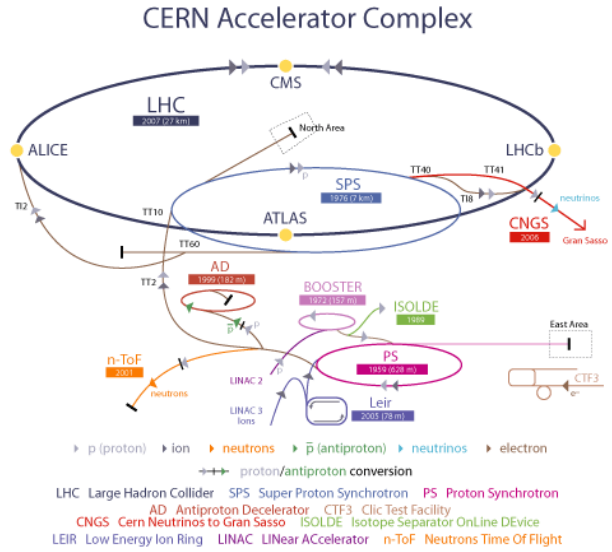


Figure 3.2: Illustration of the different facilities (LINAC, PS, SPS) and of the different experiments around the LHC ring.

interactions between cosmic particles and matter. TOTEM (TOTAl Elastic and diffractive cross section Measurement) is devoted to the study of diffractive events to evaluate the luminosity delivered by the LHC.

## 3.2 The main experiments: ALICE, ATLAS, CMS and LHCb

### 3.2.1 ALICE

A Large Ion Collider Experiment (ALICE) is dedicated to the study of the quark and gluon plasma, which is a state of matter believed to have existed at the very beginning of the Universe, between  $10^{-6}$  second and 1 second after the Big Bang. This experiment requires the LHC to accelerate and collide ions of lead instead of protons at a centre of mass energy of 2.76 TeV per nucleon pair. More details and characteristics about ALICE are given in Figure 3.3.

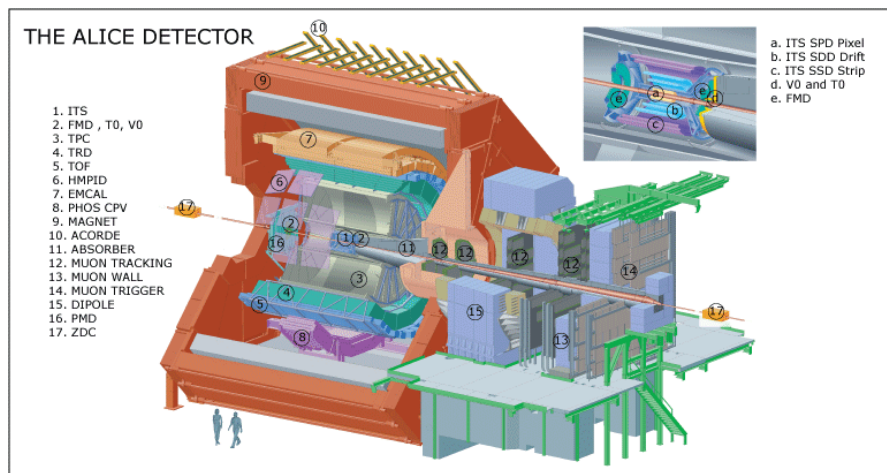


Figure 3.3: The ALICE experiment

### 3.2.2 ATLAS

A Toroidal LHC Apparatus (ATLAS) is the biggest of all the LHC detectors with its 45 m in length, its 25 m in diameter and its 7000 tons. It is a general-purpose detector dedicated to the search of the Higgs boson as well as the quest for new particles predicted by physics models beyond the Standard Model, for instance Supersymmetric particles. Moreover, some of the ATLAS measurements imply improvements on our knowledge of the Standard Model. Details on the ATLAS structure are given in Figure 3.4.

### 3.2.3 CMS

The Compact Muon Solenoid is also a general-purpose detector which main goals are the searches for Higgs bosons as well as new physics. It is the heavier LHC detector with its 12'500 tons. Along with ATLAS, CMS announced the discovery of a new boson in July 2012. This new particle is very likely believed to be the Standard Model Higgs boson. More details on the CMS experiment are given in Figure 3.5.

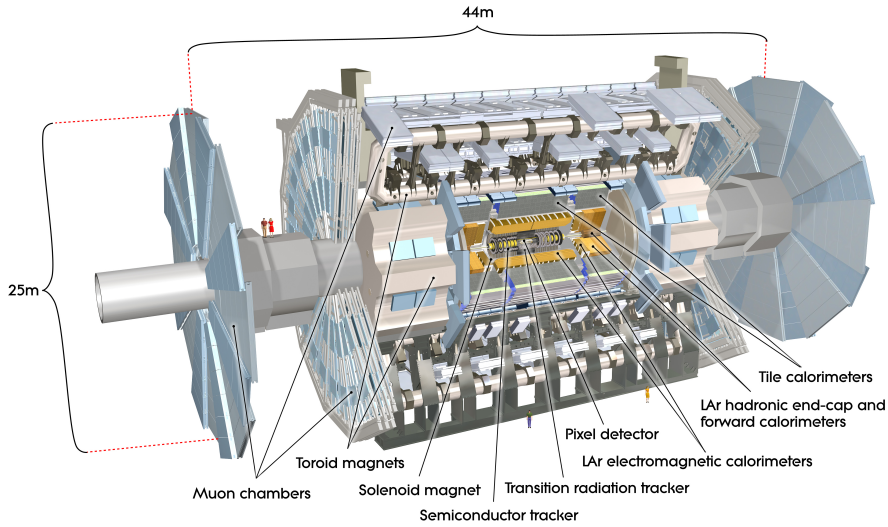


Figure 3.4: Details on the ATLAS experiment

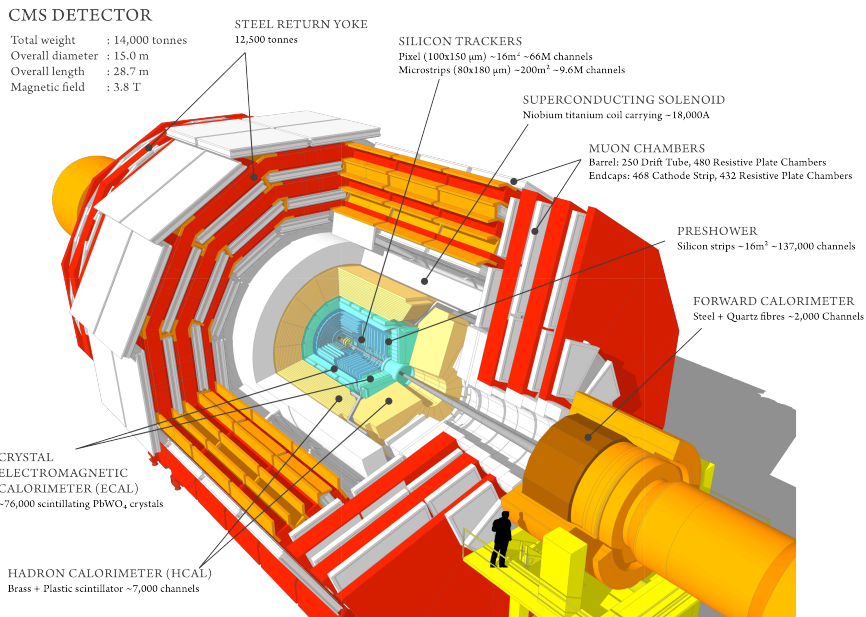


Figure 3.5: Details on the CMS experiment

### 3.2.4 LHCb

The Large Hadron Collider beauty experiment is a single arm forward spectrometer which main goal is the study of CP violation through B-hadrons decays. This detector is described in section 3.3.

### 3.3 LHCb Experiment

The LHCb detector is illustrated in Figure 3.6 and technical details can be found in [11]. Its angular coverage (acceptance) goes from 15 mrad to 250 mrad vertically and 300 mrad horizontally, corresponding to a pseudo rapidity range of  $1.8 < \eta < 4.9$  where  $\eta = -\ln(\tan(\theta/2))$ . Its geometrical design is motivated by the fact that B-hadrons have a transverse momentum smaller than their longitudinal momentum. The detector is optimized to exploit the large number of b quarks produced in the forward region. The LHCb luminosity is lower than the luminosity potential of the LHC and of the order of  $\mathcal{L}^{LHCb} = 2 \cdot 10^{32} \text{ cm}^{-2} \text{ s}^{-1}$ .

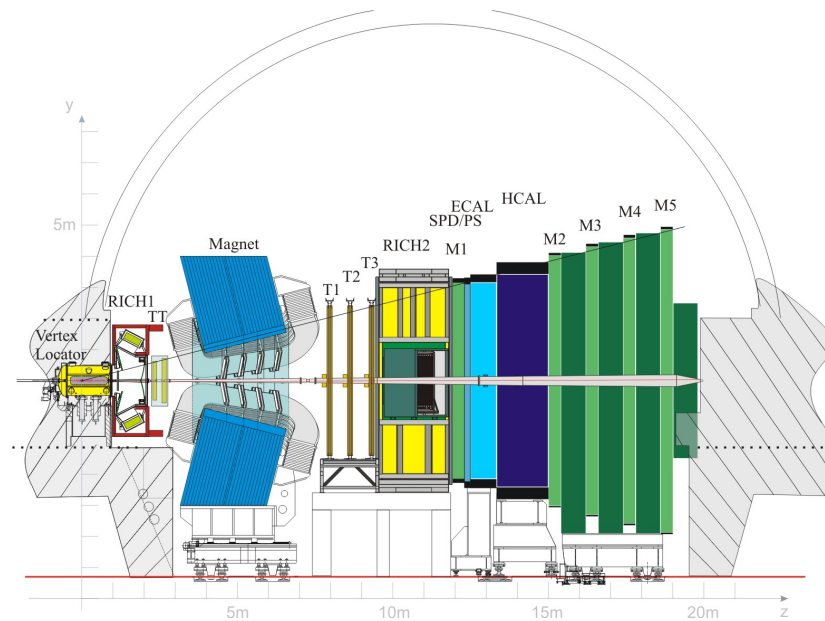


Figure 3.6: The LHCb experiment with its different sub systems: The VELO (Vertex Locator), the RICH1 (Ring Imaging Cherenkov), the TT (Tracker Turicenis), the Magnet, the Inner and Outer Trackers, the RICH2, the first Muon Chamber, the Scintillating Pad Detector, the PreShower, the Electromagnetic CALorimeter, the Hadronic CALorimeter and the four last Muon Chambers.

The next sections describe the different sub detectors mentioned in Figure 3.6 starting from the interaction point on the left. Technical details as well as general descriptions of the sub systems are strongly inspired by [11] and [12].

#### 3.3.1 The Vertex Locator

The Vertex Locator (VELO) is the detector that surrounds the interaction point. Its role is to provide precise measurements of charged particle track coordinates close to the interaction point. To achieve this ambitious mission, the VELO is constituted of a series of silicon sensors arranged along the beam axis and providing precise measurement of the  $r$  and  $\phi$  coordinates

## Chapter 3. The LHC and the LHCb Experiment

of a crossing charged particle. The third spatial coordinate is simply given by the position of each sensor plane within the experiment. A high precision is required to reconstruct decay and production vertices of beauty and charmed hadrons in order to measure their lifetimes and tag their flavor. The VELO is a crucial element on which the search for LLPs strongly relies.

As illustrated on the right plot of Figure 3.7, a module is made of azimuthal and quasi-radial detection strips. Those strips are located from 8 to 41.9 mm in radial distance and the azimuthal strips are thinner as the radial distance gets smaller.

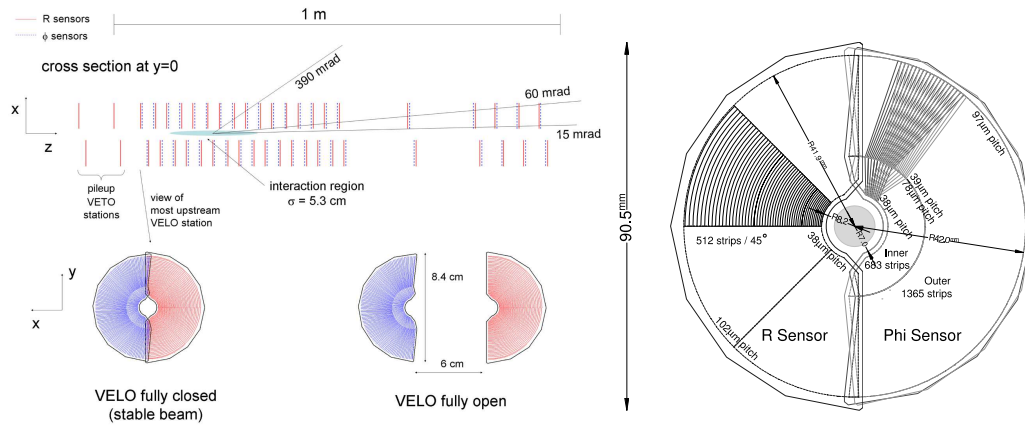


Figure 3.7: Illustration of the VELO in the  $(x,z)$  planes at  $y = 0$  and  $(x,y)$ . Notice the characteristics of the open and closed VELO positions. Dimensions of a VELO sensor are given.

The geometrical acceptance of the detector covers a pseudorapidity region of  $1.6 < \eta < 4.9$  and each track should at least intersect with three VELO modules to be reconstructed. Due to the evolution of occupancy in this region, the width of each strip decreases from 101.6 to  $38 \mu\text{m}$ . A resolution as small as  $7 \mu\text{m}$  can be reached. The temperature of the sensors is controlled between  $-10$  to  $0^\circ\text{C}$  by a cooling system. Details on the modules can be found in Figure 3.8.

During beam injection into the LHC, the VELO must be kept into the shadow of the LHCb Beryllium beam pipe to protect it from damage. Therefore the detector halves can be retracted by 3 cm, into an open position. This is achieved thanks to a remote controllable positioning system. It is also important to notice that the detector is isolated from the interaction region by a thin foil of aluminum (referred as RF-foil) to protect it against RF pickup and the RMS spread of the beam just after the injection. This RF-foil structure is represented as modeled in the software simulation tool in Figure 3.9.

### 3.3.2 The Magnet

A dipole magnet is needed to produce a strong magnetic field in order to bend the charged particles trajectories to measure their momentum. The integrated magnetic field generated by the LHCb magnet has a magnitude of 4 Tm for tracks of 10 m length. The measurement covers



	R sensor	$\phi$ -sensor
number of sensors	42 + 4 (VETO)	42
readout channels per sensor	2048	2048
sensor thickness	300 $\mu\text{m}$	300 $\mu\text{m}$
smallest pitch	40 $\mu\text{m}$	38 $\mu\text{m}$
largest pitch	102 $\mu\text{m}$	97 $\mu\text{m}$
length of shortest strip	3.8 mm	5.9 mm
length of longest strip	33.8 mm	24.9 mm
inner radius of active area	8.2 mm	8.2 mm
outer radius of active area	42 mm	42 mm
angular coverage	182 deg	$\approx$ 182 deg
stereo angle	-	10–20 deg
double metal layer	yes	yes
average occupancy	1.1%	1.1/0.7% inner/outer

Figure 3.8: Principal VELO sensor characteristics as presented in [11]

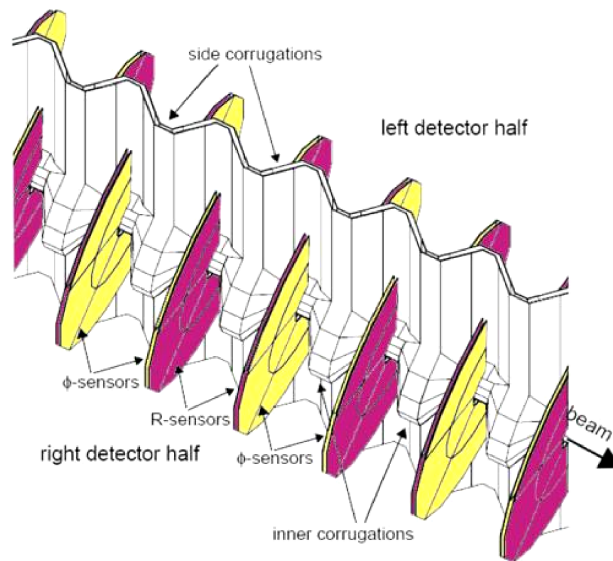


Figure 3.9: View of the inside of an RF-foil. The  $r$  and  $\phi$  sensors are illustrated with different colors. The VELO is here in the fully-closed position.

an acceptance of  $\pm 250$  mrad vertically and  $\pm 300$  mrad horizontally. The magnet is situated between the first (TT) and the second tracking station (T1) at about 5 m of the interaction point. It is 11 m wide, 8 m high and 5 m thick and weighs about 1600 tons. The temperature of the magnet is kept at 20 °C by a water cooling system at a pressure of 11 bar with an output of 150 m<sup>3</sup>/h.

To obtain the required resolution on the momentum measurements, the magnetic field integral

must be known with a precision of about  $10^{-4}$ . Thanks to measurement campaigns made with Hall probes, the precision of the field map is about  $4 \times 10^{-4}$ . It is also important to notice that measurements of CP violation need an important control of systematic effects of the detector. This is achieved by changing periodically the direction of the magnetic field by inverting the magnet polarity.

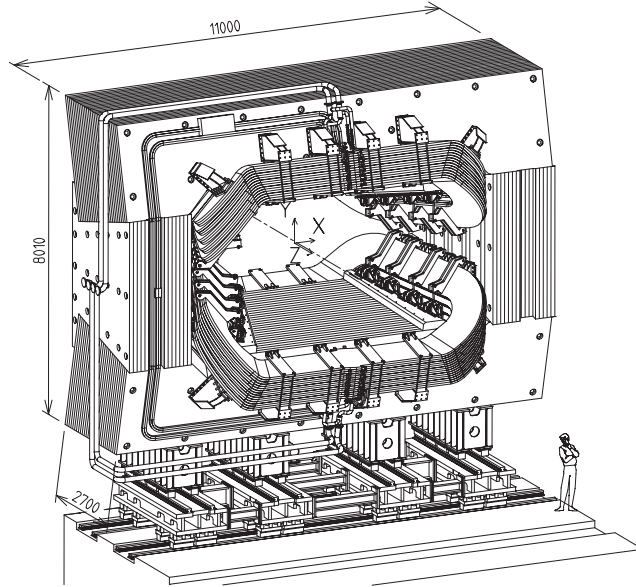


Figure 3.10: Representation of the LHCb magnet. Units are given in mm.

### 3.3.3 The Silicon Trackers

The Tracker Turicensis (TT) and the Inner Tracker (IT) are two detectors that use silicon microstrip sensors with a strip pitch of about  $200 \mu\text{m}$ . The TT is located upstream of the magnet and is a 150 cm wide and 130 cm high planar tracking station. Meanwhile, the IT is 120 cm wide and 40 cm high, cross shaped, and located in the center of the three tracking stations. The IT is made of four individual detector boxes arranged along the beam pipe. Figure 3.11 and 3.12 illustrate IT and TT geometries.

The four detection layers are arranged in a (x-u-v-x) configuration with vertical strips in the x region while the strips are rotated by a stereo angle of  $\pm 5^\circ$  in respectively the u/v region. The single hit spatial resolution of  $50 \mu\text{m}$  is achieved by readout strip pitches of  $200 \mu\text{m}$ . A better resolution would be dominated by multiple scattering effects and therefore be useless. The hit occupancy is expected to reach  $5 \cdot 10^{-2}$  per  $\text{cm}^2$  in the innermost regions while it is expected to reach  $5 \cdot 10^{-4}$  per  $\text{cm}^2$  in the outermost regions of the TT. For the IT, the occupancy is about  $1.5 \cdot 10^{-2}$  per  $\text{cm}^2$  close to the beam region while it is expected to be of about  $2 \cdot 10^{-3}$  per  $\text{cm}^2$  in the outer regions. Therefore, the strip geometry is adapted to keep a maximum strip occupancy that does not exceed a few percent.

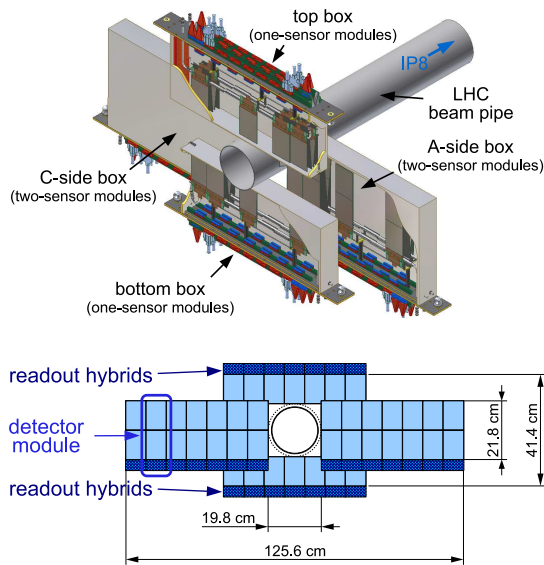


Figure 3.11: The top picture displays a perspective view of one of the four boxes of the three IT stations arranged around the beam pipe. The bottom picture is a view in the  $(x,y)$  plane of the second IT station.

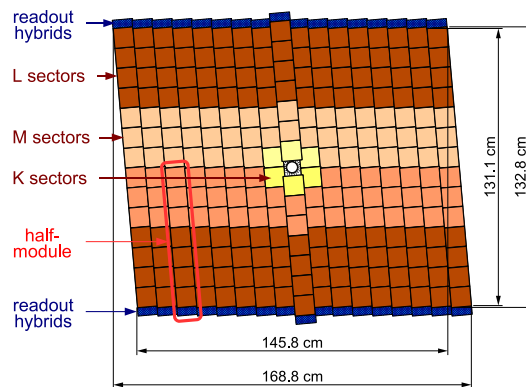


Figure 3.12: Third layer of the TT sub detector.

The TT temperature is maintained below  $5^{\circ}\text{C}$  to limit radiation damage and the TT volume is constantly flushed with nitrogen to avoid condensation. The IT is equipped with a  $\text{C}_6\text{F}_{14}$  cooling system to keep its temperature at  $-15^{\circ}\text{C}$ .

### 3.3.4 The Outer Tracker

The Outer tracker (OT) is a drift detector providing the excellent momentum measurement resolution needed for the determination of the invariant mass of B-hadrons. At  $10 \text{ MeV}/c^2$ , the relative resolution reaches about 0.4%.

The OT is basically an array of individual gas-tight straw-tube modules, each of them containing two staggered monolayers of drift tubes of 4.9 mm in diameter. The tubes contain a mixture of 70% of Argon and 30% of Carbon dioxide insuring a fast drift time of less than 50 ns. The modules are arranged into three stations of four layers in a (x-u-v-x) configuration similar to the IT/TT configurations. The acceptance of the detector is 300 mrad in the horizontal plane and 250 mrad in the vertical plane to ensure a maximal occupancy of 10% at a luminosity of  $2 \times 10^{32} \text{ cm}^{-2} \text{ s}^{-1}$ . A station has two retractable halves on either side of the beam pipe as illustrated in the Figure 3.13.

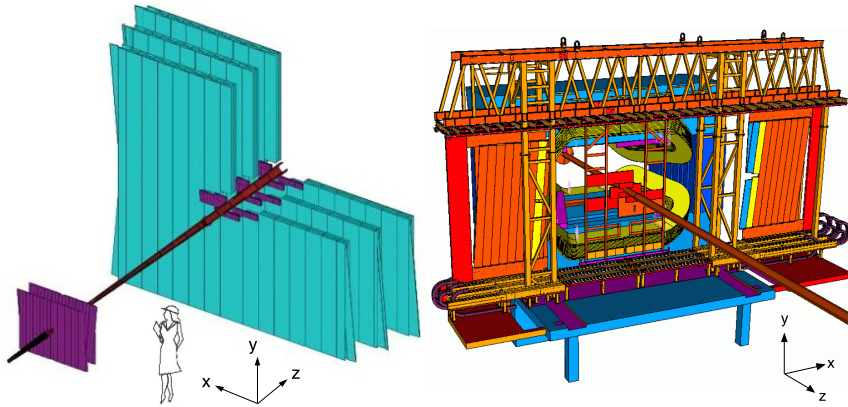


Figure 3.13: The left plot illustrates the arrangement of the three OT stations. The right plot represents the third OT station carried by its bridge into the open position.

### 3.3.5 The Ring Imaging Cherenkov 1 & 2

The Particle IDentification (PID) system consists on two Ring Imaging Cherenkov (RICH 1 and 2) detectors situated between the VELO and the TT for the first one and between the last tracking station and the first muon station for the later.

When a particle goes through a medium with a velocity greater than the speed of light in this particular medium, it emits a cone of light which emission angle directly depends of the  $\gamma$ -factor of the crossing particle. This is illustrated in Figure 3.14.

The RICH 1 covers a low momentum range from 1 GeV/c to 60 GeV/c using a  $C_4F_{10}$  gas and an aerogel as radiators. The RICH 2 covers high momenta, from 15 GeV/c to beyond 100 GeV/c using a  $CF_4$  radiator. The RICH 1 acceptance covers the full LHCb acceptance while RICH 2 has a limited acceptance of about  $\pm 15$  mrad to  $\pm 120$  mrad horizontally and  $\pm 100$  mrad vertically (which matches the region where high momentum particles are produced).

To detected the emitted Cherenkov photons, Hybrid Photon Detectors (HPDs) covering the wavelength range 200 to 600 nm are used. They are located outside the LHCb acceptance along with the spherical and planar mirrors used to reflect and focalize the emitted light.

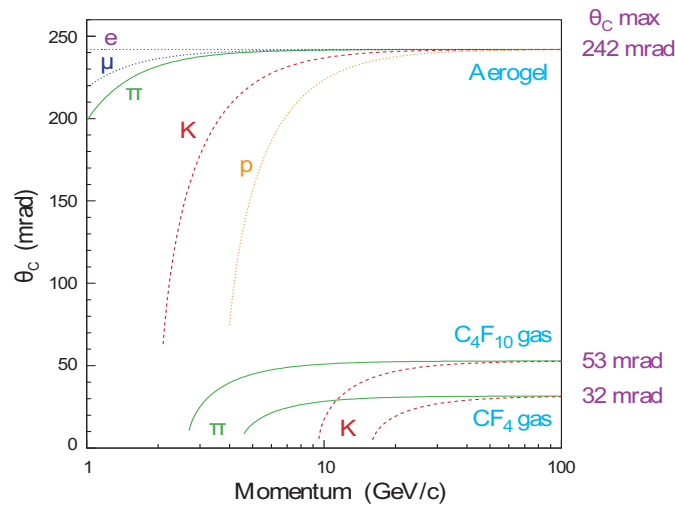


Figure 3.14: Cherenkov angle versus particle momentum for different media and particle types.

Illustrations RICH1 are given in the Figure 3.15. An example of event as seen by RICH1 is given

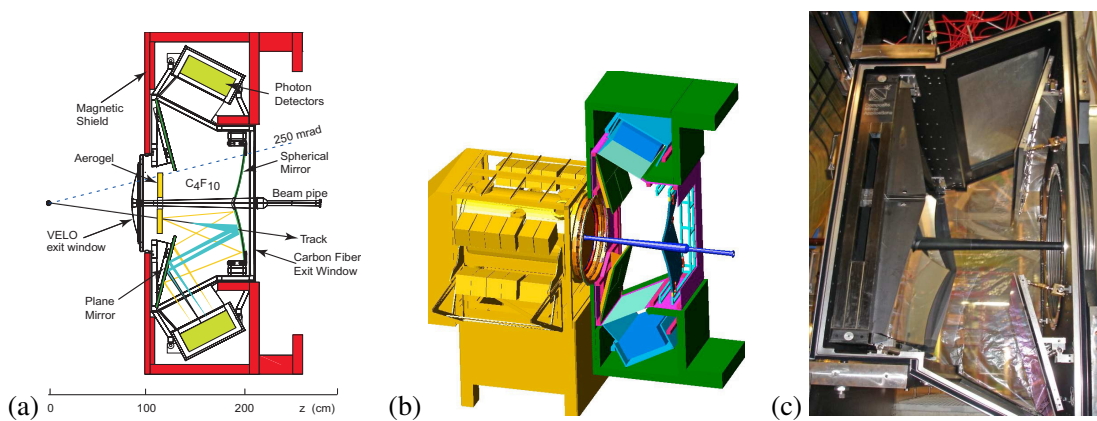


Figure 3.15: (a) Schematic view of the side of RICH1. 3D model (b) and picture (c) of the detector.

in Figure 3.16.

### 3.3.6 The Electromagnetic and Hadronic Calorimeters

The calorimeter system collects and analyses identification informations of electrons and hadrons and measures photons and neutral pions energies. It provides measurements of the energy and position of the incoming particles. Unlike the tracking system, the calorimeter system objective is to collect the energy of a particle and so has to stop it completely. It is tuned to give good background rejection and reasonable efficiency for B decays through resolution and shower separation. The separation between pions and electrons for momentum of 10,

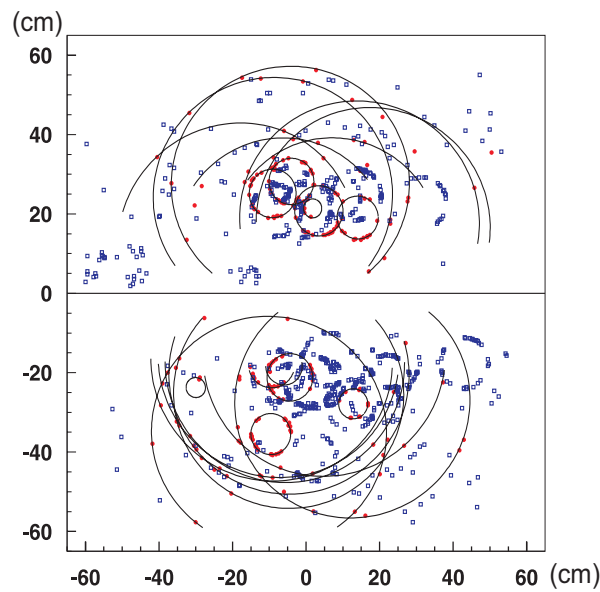


Figure 3.16: Example of a LHCb event as seen by the RICH1 detector.

20 and 50 GeV/c translates in pions rejection factors of 99.6%, 99.6% and 99.7% while the retention rates of electrons are respectively of 91%, 92% and 97%. The basic principle of a calorimeter is that the scintillating light produced within the shower is transmitted to a photomultiplier (PMT) by wavelength-shifting (WLS) fibers. The calorimeter system is made of Scintillating Pad Detectors (SPD)/PreShower (PS), the Electromagnetic Calorimeter (ECAL) and the Hadronic Calorimeter (HCAL) arranged in this order from the interaction point. Figure 3.17 and 3.18 give an illustration of, respectively, the ECAL and the HCAL.

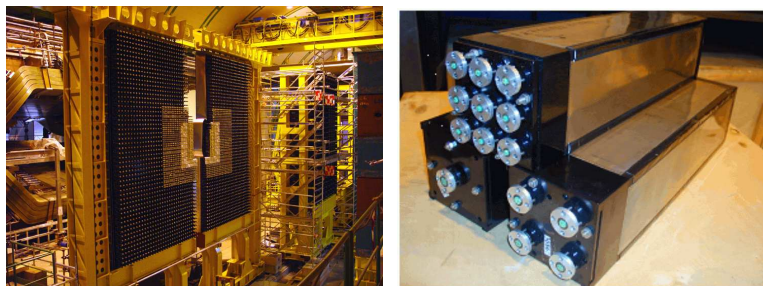


Figure 3.17: View of the ECAL not completely closed and outer, middle and inner type of ECAL modules on the right-hand side.

The SPD/PS is useful for the selection of charged particles and the distinction between electrons and photons taking advantage of the different longitudinal profiles of the electromagnetic and hadronic showers. The PS is located beyond a thin layer of lead.

The ECAL is designed to contain a whole electromagnetic shower and therefore, measures 25

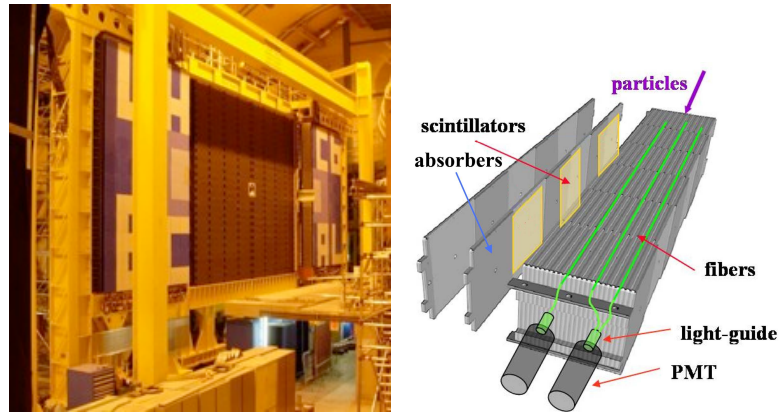


Figure 3.18: HCAL detector and, on the right-hand side, a schematic view of its internal cell structure.

radiation lengths while the HCAL being mainly used by the trigger system measures only 5.6 interaction lengths to meet with space saving purposes. To keep a constant occupancy of the cells, three regions for the ECAL and two regions for the HCAL of different sections have been designed in function of their distance to the beam line. The sections are therefore smaller for the inner part and larger for the outer part of the detector as illustrated by Figure 3.19.

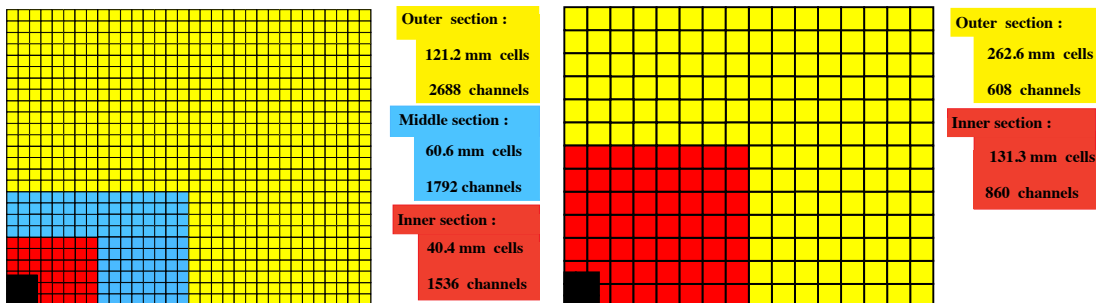


Figure 3.19: (x,y) view of the SPD/PS and ECAL on the left and of the HCAL on the right. Only one fourth of the detector is depicted. Dimensions of the cells are given on the right-hand side of the pictures.

The energy resolution of the ECAL is  $\sigma_E/E = 10\% \oplus 1\%$  (E in GeV) and its acceptance is  $\pm 25$  mrad to  $\pm 300$  mrad horizontally and  $\pm 250$  mrad vertically. A saturation of the cells appears when the transverse momentum of the particle initiating the shower is greater or equal to 10 GeV/c.

The HCAL energy resolution is  $\sigma_E/E = (69.5 \pm 5\%) \oplus (9 \pm 2)\%$  (E in GeV) and its geometrical acceptance is the same as the one of the ECAL.

### 3.3.7 The Muon System

Five plans of muon chambers are installed, one of them is inserted before the calorimeters (to improve the transverse momentum measurements in the trigger system) while the four other chambers are located in the most upstream part of the detector because the muons are the most penetrating detectable particles. The muon system includes 1380 muon chambers and cover a total surface of  $435 \text{ m}^2$ . Its acceptance goes from 16 mrad to 258 mrad vertically and 20 mrad to 306 mrad horizontally. An illustration is presented in Figure 3.20.

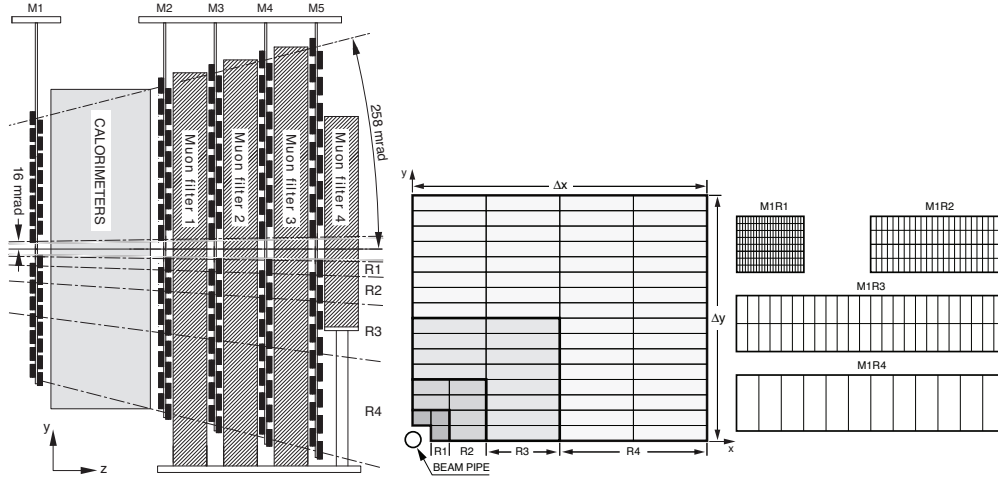


Figure 3.20: (y,z) view of the four last muon chambers on the left-hand side. The right-hand side illustrates a face view of one of the muon stations, each of them containing 276 muon chambers.

To stop the hadrons punching through the hadronic calorimeter and select only penetrating muons, an iron absorber of 80 cm in thickness is inserted between each muon stations. The minimum momentum that a muon should possess to cross each station is 6 GeV/c since the total absorber thickness is about 20 interaction lengths. The  $p_T$  resolution is about 20% while the efficiency of detection is greater than 95%. A station is divided into four regions with dimension designed to ensure a constant particle flux and occupancy. The technology used by this detector is based on multi-wire proportional chambers except for the first station where the expected particle rate impose the use of triple-GEM detectors. The temporal resolution of the detector is 25 ns.

### 3.3.8 The Trigger Systems

As previously stated, the designed instantaneous luminosity of LHCb is a lot smaller than the one delivered by the LHC, being  $2 \times 10^{32} \text{ cm}^{-2} \text{ s}^{-1}$ . The bunch crossing rate is 40 MHz. It is impossible to store all produced events into disk at this frequency. Moreover, only a small fraction of the events is relevant for b physics analyses. Therefore, a drastic rate reduction is needed, which is the role of the three levels of the trigger system.



The Level-0 trigger (L0) achieves a rate reduction from 40 to 1 MHz. At this rate, the entire detector can be read-out. The L0 trigger reconstructs the highest  $E_T$  hadron, electron and photon clusters in the calorimeter system and the two highest  $p_T$  muons in the muon chambers with a  $\sim 20\%$  resolution. In addition, the pile-up system in the VELO estimates the number of pp interactions in each bunch crossing. This constitutes the three components of the L0 trigger system as illustrated in the Figure 3.21

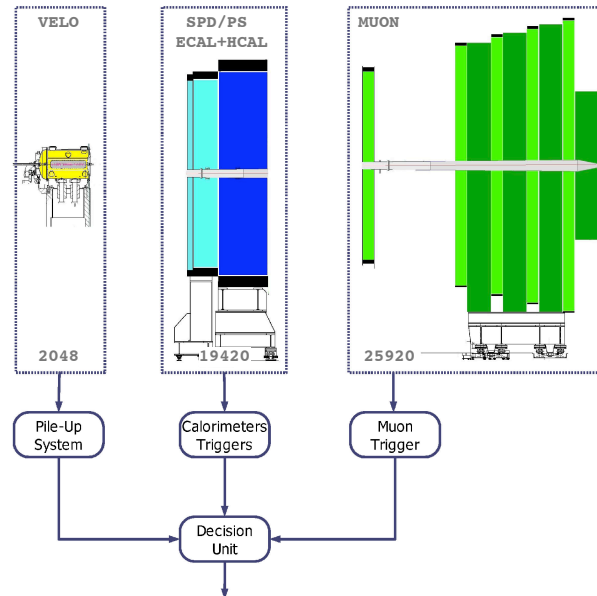


Figure 3.21: Overview of the L0 trigger.

The L0 trigger is full synchronous with the 40 MHz bunch crossing rate. If one or all of the three L0 components give a positive response, the event is passed to the High Level Trigger (HLT) sequences. Examples of typical L0 criteria are: at least one cluster in the HCAL with  $E_T^{hadron} > 3.5$  GeV or in the ECAL with  $E_T^{\gamma, e, \pi^0} > 2.5$  GeV or a muon candidate with  $p_T^\mu > 1.2$  GeV or  $p_T^{\mu_1} + p_T^{\mu_2} > 1$  GeV with  $\mu_{1,2}$  being the two muons with the largest  $p_T$ .

To further reduce the rate from 1 MHz to 5 KHz, the HLT uses the full event information. High level triggers are C++ applications running on every CPU of up to 2000 computing nodes. The HLT is divided into "alleys" to refine the L0 candidates. The selections are made based on confirmation of the precedent trigger stage by requiring tracks in the VELO or T-stations, with a combination of high  $p_T$  or large impact parameters. By doing so, the rate is already lowered to 30 KHz. Then, interesting final states are selected using inclusive or exclusive criteria. Those criteria are of course less constraining than those of the offline analyses to let space for adjustments and refinements.

The HLT1, given the 1 MHz rate of L0 and CPU power limitations, uses only part of the full event data. Its aim is to reconstruct particles corresponding to L0 objects in the VELO and in

the T1, T2 and T3 stations. For photons and  $\pi^0$ , HLT1 must confirm that no charged particles can be associated to their signature in the calorimeters.

Then, the HLT2 combines inclusive algorithms where B and C-hadrons are reconstructed partially and exclusive algorithms in which final states of B-hadron and C-hadron decays as well as LLPs are fully reconstructed. Therefore, the rate is lowered to 5 KHz and the event is stored on disk for further off-line analysis. Finally, it must be noted that a fraction of the bandwidth is devoted to calibration and monitoring.

A summary of the LHCb trigger system is given in Figure 3.22.

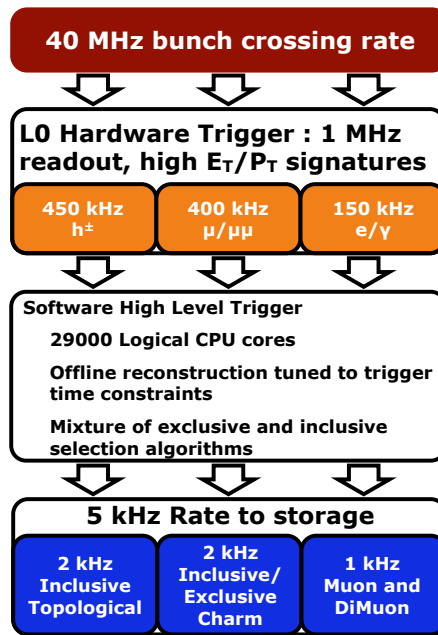


Figure 3.22: Flow-diagram of the LHCb trigger system with the rate reduction given after each trigger stage.

### 3.3.9 Track Reconstruction

To reconstruct the tracks of charged particles, the software combines the hits in the VELO, TT and T1, T2, T3 tracking stations. There exists different types of tracks in function of their trajectories inside the detector as represented in Figure 3.23:

- **Long tracks** traversing the full tracking system, from the VELO to the T stations. Naturally those are the tracks giving the most accurate momentum measurement.
- **Upstream tracks** reconstructed only by hits in the VELO and the TT, this type is in general of lower momentum but may generate Cherenkov photons passing through the RICH1. However their momentum resolution is rather poor.

- **Downstream tracks** traversing only the TT and the T stations most probably due to decays of particles outside the VELO acceptance.
- **VELO tracks** useful for primary vertex reconstruction, they are typically large angle or backward tracks.
- **T tracks** are only measured in the T stations

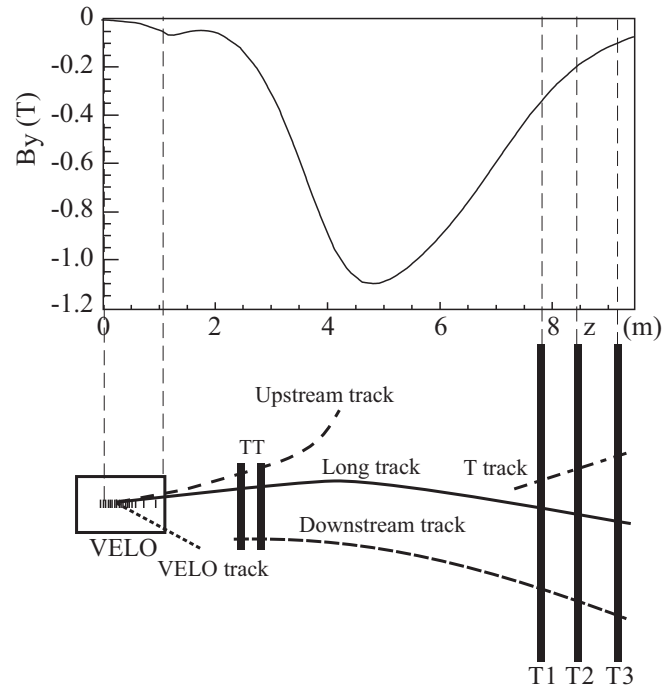


Figure 3.23: Magnetic field amplitude in function of the z-coordinate (up) and different track types (bottom)

To reconstruct a track, the software start with *seeds* that are the initial track candidates in the VELO and the T stations where the magnetic field is low. Then the trajectories are refined using Kalman filters (see for example [13]). The quality of the reconstruction is given by the  $\chi^2$  of the fit and the *pull* distribution of the track parameters. The performance of the pattern recognition is evaluated in terms of efficiencies and ghost rates.

### 3.3.10 Stripping

In order to save computing time and avoid treating a too large amount of irrelevant events, the data are classified and organized according to stripping lines. Each of those lines are dedicated to specific physics analyses. For instance, the search for new long lived exotic particles has dedicated stripping lines that selects relevant events for further studies. The stripping lines are grouped onto "streams" in function of their overlaps. The streams are named Bhadron, semileptonic, leptonic, PID, dimuon, calibration, radiative, CharmCompleteEvent, charm,

MinBias and electroweak. The latter contains lines dedicated to  $Z^0$  and  $W^\pm$  bosons analyses, the Drell Yann process analyses, the high  $p_T$  jets analyses and the displaced vertices analyses. These lines change and develop over time and new versions of the stripping are frequently released (results presented in this thesis are obtained working with the stripping version 17). The stripping process uses the same framework than HLT but incorporates all the offline available tools and resources. The data directly coming from specific stripping lines are often called "preselected" data. The stripping efficiency strongly depends on the available storage and bandwidth capacities associated to it and therefore implies that a part of the considered signal is inevitably lost compared with the HLT2 output.

### 3.3.11 Monte Carlo Simulation and Analysis Softwares

To produce Monte Carlo simulated data, many different softwares are used one after another to reproduce the physics but also the detector response to the generated processes. Those software are named Gauss, Boole, Moore, Brunel and DaVinci.

Gauss is the project regrouping every aspects of the event generation, from the physical process generation by Pythia or Alpgen from Feynman diagrams and matrix elements, to the simulation of the interaction of the generated particle with the detector by GEANT 4.

Then, Boole is the software producing the digitalization of the event. It simulates the electrical response of each detector while crossed by a particle. This step concludes the simulation part of the physical processes of Monte Carlo events. Brunel is the software responsible for the reconstruction of the tracks from Boole data and for the clustering of calorimeter signals.

The next step is performed by Moore that reproduces the trigger decision for each event.

To conclude, DaVinci is the software used for the stripping and the analysis of the data, offering a wide range of mathematical functions to combine, study and understand the physical content of a LHCb event, real or simulated.

## 4 Search for Long-Lived Particles

This chapter presents the selection of events relevant for the search of a pair of long-lived exotic particles produced by the decay of a Higgs-like boson.

First, a study of Monte Carlo data samples corresponding to the models described in Chapter 2 with some parameters chosen as benchmark values is presented. A four vector analysis is performed to characterize such events. Then, on this basis, the strategy for the selection of events is described. Finally, the corresponding efficiencies are estimated.

### 4.1 Monte Carlo event samples generation and descriptions of data sets

Following the description of different theoretical models given in Chapter 2, a large variety of MC samples corresponding to a various range of lifetimes and masses of LSP and Higgs-like boson have been produced with Pythia 6423 (see [14]) and GEANT4 (see [15]). Those models along with background samples are listed in Table 4.1. The parameters used for the signal events generation are given in Table 4.2. It is worth noting that it is possible to extrapolate the expected results for other points in the parameter space. Moreover, the search is performed only for LLPs produced by the decay of a Higgs-like boson.

The data sample corresponds to the events recorded by the LHCb experiment from June 2011 to the end of the year<sup>1</sup>. Its integrated luminosity corresponds to  $0.9 \text{ fb}^{-1}$ .

The background MC set includes two kinds of  $b\bar{b}$  processes, "inclusive" but also biased by the requirement of two b-hadrons decaying in the detector "enlarged" acceptance ( $1.5 \leq \eta \leq 5$ ). A  $c\bar{c}$  sample with the same requirement on the c-hadron is also analyzed.

---

<sup>1</sup>It has been processed by the 12th version of the reconstruction software and by the version 17 of the electroweak stripping.

## Chapter 4. Search for Long-Lived Particles

Set	Type	N events		$\epsilon_{gen}$
HV10	MC11a	64.2k	Hidden valley $\tau=10$ $m(\pi_\nu)=35$ $m(H_{30})=120$	
BV48_5	MC11a	63.3k	$m(\chi)=48$ $\tau=5$ $m(h^0)=114$	0.28
BV48	MC11a	64.5k	$m(\chi)=48$ $\tau=10$ $m(h^0)=114$	0.28
BV48_15	MC11a	62.1k	$m(\chi)=48$ $\tau=15$ $m(h^0)=114$	0.28
BV48_50	MC11a	64k	$m(\chi)=48$ $\tau=50$ $m(h^0)=114$	0.28
BV20_10	MC11a	65.4k	$m(\chi)=20$ $\tau=10$ $m(h^0)=114$	0.26
BV35_10	MC11a	65.4k	$m(\chi)=35$ $\tau=10$ $m(h^0)=114$	0.27
BV48_mh100	MC11a	64.8k	$m(\chi)=48$ $\tau=10$ $m(h^0)=100$	0.33
BV48_mh125	MC11a	300.2k	$m(\chi)=48$ $\tau=10$ $m(h^0)=125$	0.27
$t\bar{t}$	MC11a	509.6k	$t \rightarrow b\bar{b} + 1 \text{ lepton}(p_T > 10 \text{ GeV})$	0.01
$b\bar{b}$	MC11a	200.6k		
$b\bar{b}$	MC11a	17.1M	two b in acceptance $1.5 \leq \eta \leq 5$	0.22
$c\bar{c}$	MC11a	9.1M	two c in acceptance $1.5 \leq \eta \leq 5$	0.25
$J/\psi$	MC11a	20M	$J/\psi(1S) \rightarrow \mu^+ \mu^-$	
Data 2011	Reco12 (EW)Strip17		$\int L dt = 0.9 \text{ fb}^{-1}$	

Table 4.1: Summary of data and full simulated MC sets of events used in this study. Mass units are  $\text{GeV}/c^2$ , lifetimes are given in ps. The last column gives the generator efficiency.

Model	$\tau$ [ps]	M1	M2	$\tan \beta$	$\mu$	$m_{LLP}$	$m_{h^0}$
BV48	10	62	250	5	140	48	114
BV48-5	5	62	250	5	140	48	114
BV48-15	15	62	250	5	140	48	114
BV48-50	50	62	250	5	140	48	114
BV20-10	10	28	250	5	140	20	114
BV35-10	10	46	250	5	140	35	114
BV48-mh100	10	71	250	2.4	140	48	100
BV48_mh125	10	60	250	8	140	48	125
HV10	10					35	120

Table 4.2: Parameters of the models considered in this study: B violating processes (BV), and Hidden Valley (HV). Mass units are  $\text{GeV}/c^2$ . The LLP of the BV model is the  $\tilde{\chi}_1^0$ , the  $\pi_\nu^0$  for HV. In the case of BV, M1 and M2 correspond to the Pythia parameters RMSS(1) and RMSS(2),  $\mu$  is RMSS(4) and  $\tan \beta$  RMSS(5). A Higgs mass of  $125 \text{ GeV}/c^2$  requires also RMSS(16) = 2300. The lifetime of the LLP is fixed by hand. HV masses and lifetimes are free, and then set by hand.

Table 4.3 and Table 4.4 give the cross-section upper limits obtained from the analysis made using the data taken by LHCb in 2010 and presented in [16]. From the 32 pb upper limit of 2010, a maximal number of 7820 events with two LLPs in the LHCb acceptance is expected for the BV48 model in 2011 (if we assume a branching ratio equal to one for the decay of the Higgs boson to a pair of neutralino).

#### 4.1. Monte Carlo event samples generation and descriptions of data sets

$m_{h^0} / m_{LLP} =$	20	25	30	35	40	48	55
100	371	189	101	58	44	58	
105	585	210	100	75	44	39	
110	618	265	132	75	56	34	
114	618	237	128	91	47	32	46
120	556	359	148	93	58	34	31
125	618	301	179	90	61	41	29

Table 4.3: Cross section upper limits, in pb, valid for a LLP lifetime of 10 ps. Results as they are presented in [16], from the 2010 data set analysis.

$\tau_{LLP} / m_{LLP} =$	20	25	30	35	40	48	55
3	1183	362	210	156	136	168	410
5	588	278	145	101	68	58	137
10	636	238	129	91	47	32	46
15	687	260	155	90	49	31	33
20	687	260	131	93	63	32	31
25	824	298	142	100	61	34	25
30	752	309	150	100	56	35	24
50	919	417	200	108	72	40	29

Table 4.4: Cross section upper limits in pb inferred from the results of the 2010 analysis presented in [16] with a Higgs-boson mass of 114 GeV/c<sup>2</sup>.

In [16], the two LLP candidates are required to be reconstructed from at least six charged tracks. The six tracks must have a total invariant mass of at least 6 GeV/c<sup>2</sup> and the vertices must have a radial distance R from the beam line of at least 0.4 mm.

## 4.2 Signal model analysis at four-vector level

This section aims at giving a general idea of the properties of the theoretical models using only the 4-vector informations provided by the event generator. An early generator level analysis is available in [17]. Results are mostly identical to the ones shown in [16] and [18] from the 2010 data analysis, but some of them have been updated to match the conditions of 2011.

In the BV48 case, the generated quark composition is around 18.5% for the combinations with a b quark, (udb, usb, cdb, csb) and 13% for udq and cdq, where q is not a b quark. This means that about 70% of the LLPs have a b quark in the decay.

Some kinematical properties of the Higgs bosons and of the LLP can be found in the Figures 4.1 to 4.6, for the BV48 and HV10 models but also for other BV models when significant differences appear between them. The observed differences are essentially due to the choice of the LLP masses and lifetimes.

The distributions of the Figures 4.1 to 4.3 have been calculated with the unique requirement that the two LLP particles are flying with a pseudorapidity larger than 1.8. This requirement selects 19.8 % of the events.

Figure 4.1 shows the transverse momentum and pseudorapidity distributions of the mother boson, when the two daughters satisfy the above condition. The boson is produced in the forward direction with a transverse momentum which is in general quite low: below 10 GeV/c.

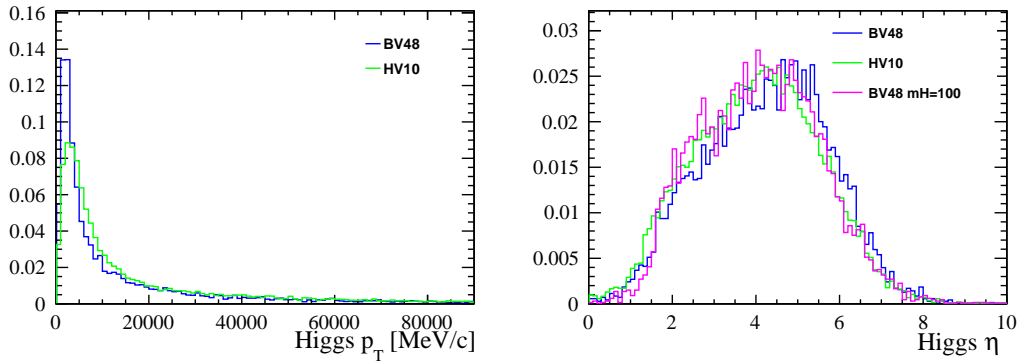


Figure 4.1: Some properties of the Higgs boson determined at generator level: the transverse momentum (left) and the pseudorapidity distributions (right). Plots are normalized to unity.

Figure 4.2 displays the pseudorapidity, the transverse momentum and the flight length of the LLP.

Figure 4.3 gives the generated decay coordinates of the LLP in z and r. The radial decay position is a crucial observable to select LLPs.

In order to get closer to the experimental conditions, the transverse momentum distributions of the reconstructed LLP in Figure 4.4 is obtained using only charged tracks in acceptance, and



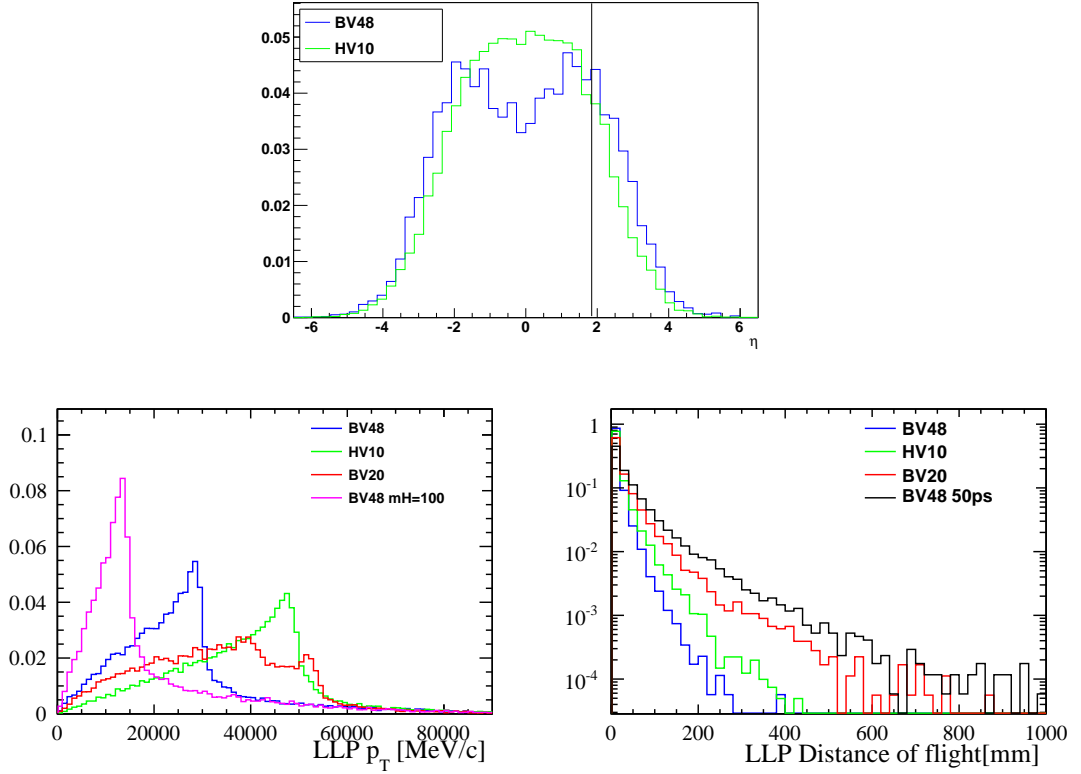


Figure 4.2: Properties of the LLP determined at generator level: the pseudorapidity distributions (top, from [18]) (the cut at 1.8 indicated by a vertical line is not active for this plot), the transverse momentum (bottom left), and the flight length (bottom right). Distributions are normalized to unity.

compatible with the displaced vertices. For this, the selected tracks are those passing within 2 mm from the (true) decay position of the LLP. The other plots are the mass distribution obtained from this set of charged particles, and the number of charged particles selected by the procedure. Because the LLP is neutral, when all the charged particles from the decay are properly considered, only the even bins are expected to be filled in. The counts in the odd bins happen when an odd number of tracks is lost because falling outside acceptance or when produced from tertiary vertices falling outside the 2 mm window.

Figure 4.5 shows the Higgs mass reconstructed using the LLP candidates of Figure 4.4.

Finally, Figure 4.6 is an attempt to reconstruct the LLP mass by gathering all the stable particles (except neutrinos) falling in a cone of radius  $R=1$  in  $(\eta, \phi)$  around the LLP momentum direction. In practice, the LLP is considered to be a broad jet. The resolution is much worse than what has been obtained before, using charged particles from the decay. This is due to the relatively large mass of the LLP, and its decay into several partons.

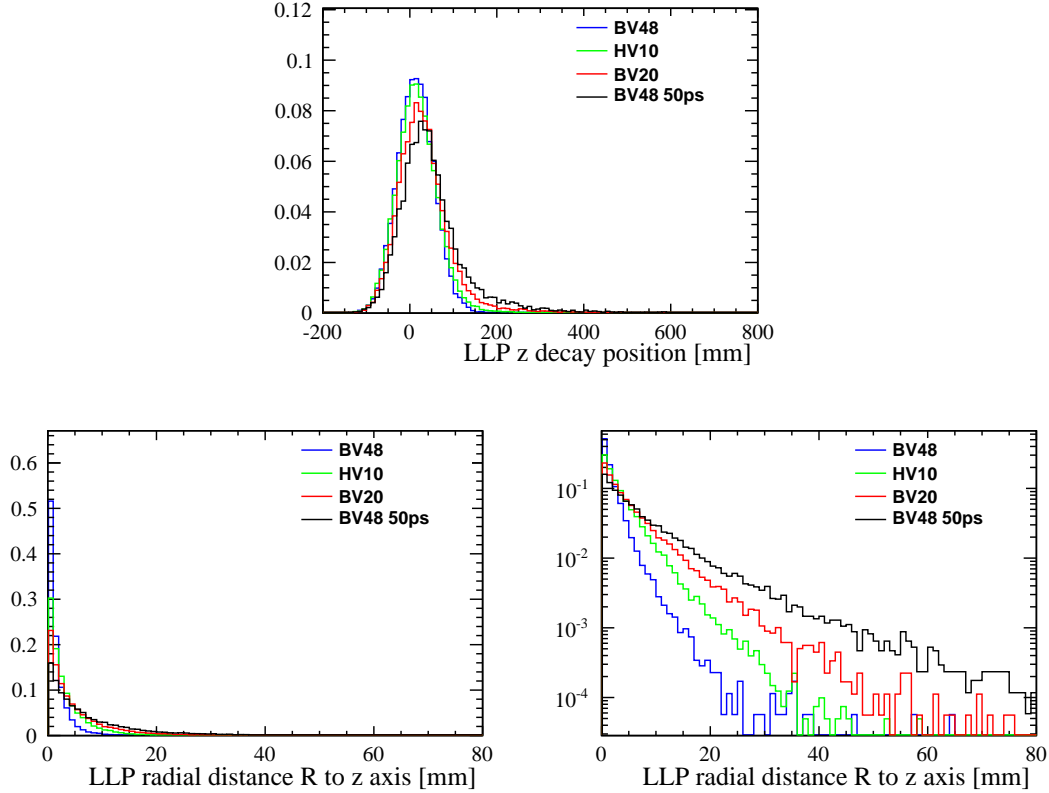


Figure 4.3: Top: decay position of the LLP on the z axis. Bottom: radial position, linear and log scales. Distributions are normalized to unity.

### 4.3 2011 data analysis

Inferred from the 4-vector analysis of MC generated events, the selection technique is based on the identification of massive secondary vertices. The document [19] describes in details the vertex reconstruction both at trigger and stripping levels.

#### 4.3.1 Vertex reconstruction using PatPV algorithms

The main difference between the trigger and stripping contexts comes from the fact that, online, the algorithms rely on the tracks found by the VELO while the whole reconstructed tracks are used offline. In practice, the same sequence of algorithm is used for primary and secondary vertex reconstruction. Two subsequent steps are executed. First an algorithm (**PVSeed3DTool**) creates *seeds* by looking for points at which a sufficient number of tracks pass close to each others. It starts from a track, called *base track*, and determines the number of close tracks. Close means a distance of closest approach (DOCA) smaller than 0.3 mm. Then, if the number of close tracks is too small ( in general smaller than 4), another base track is considered. Then, for every track pair, the average point of closest approach (POCA) is

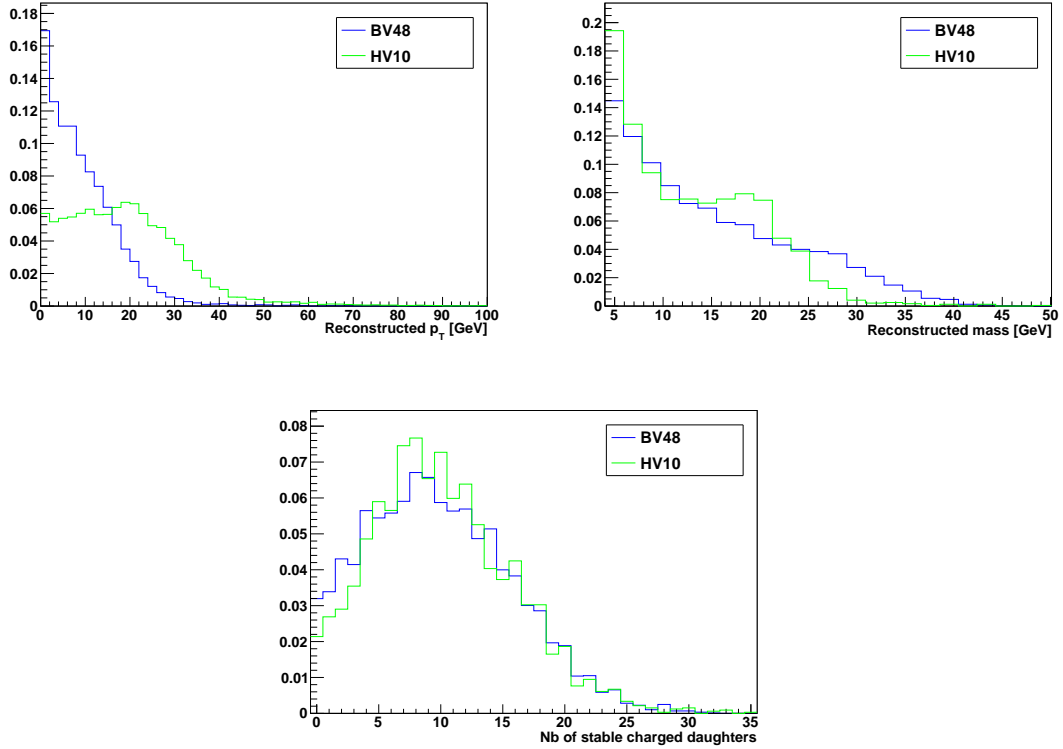


Figure 4.4: Distributions of the transverse momentum (top left) and of the mass (top right). For the calculation, charged stable particles produced in the acceptance are selected when passing at less than 2 mm from the position of true decay point of the LLP. The number of particles selected by the procedure is given in the last plot. Distributions are normalized to unity (from [18]).

calculated and an average is made in a two-steps procedure. POCA with distance larger than 3 mm to the mean are removed and the calculation is done again. A weight is then associated to each POCA entry, taking typical track parameter errors and opening angle of the track into account. When the number of close tracks with maximal  $z$  spread distance exceeds the minimal number of close tracks required, the seed is accepted. The tuning of this procedure is designed to maximize the seeding efficiency, allowing for some fake seeds. This has been proven not to affect much the performance of the PV reconstruction (see [19]).

The second step consists on an adaptive least square fit (performed by the **LSAdaptPVFitter** algorithm) from the combination of seeds. The procedure has been developed to avoid systematic shifts of the PV due to a fraction of badly measured tracks (ghosts and multiple scattering effects). An adaptive weight least square method, the Tukey biweight method, is used to assign a  $(1 - \chi_{IP}^2/C_T^2)^2$  weight to a track according to its  $\chi_{IP}^2$ .  $C_T$  is the Tukey constant. The procedure requires a minimum number of tracks (generally 5 for primary and 4 for displaced vertices) with a maximum  $\chi^2$  (typically 9) and a minimum track weight of  $1 \times 10^{-8}$ .

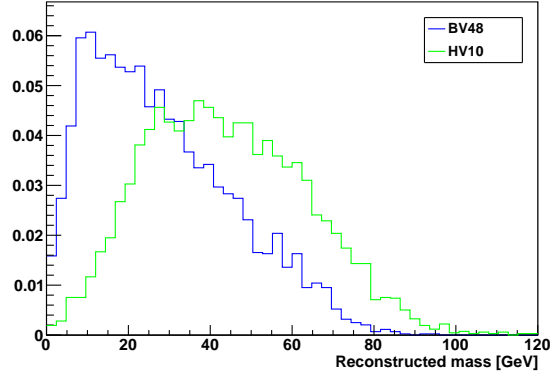


Figure 4.5: Mass of Higgs parent, obtained by combining the two LLP candidates reconstructed from charged particles, as seen in Figure 4.4. Distributions are normalized to unity (from [18]).

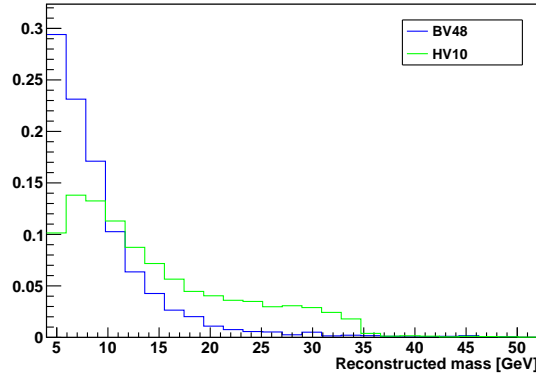


Figure 4.6: The LLP mass reconstructed using the particles falling in a R=1 cone around the LLP direction. All the stable particles have been used with the exception of neutrinos. Distributions are normalized to unity (from [18]).

Afterwards, tracks that have a maximum  $\chi^2$  larger than 25 are removed from the list used for further vertex searches. It has to be noticed that the displaced vertex stripping uses a slightly different algorithm (**LSAdaptPV3DFitter**) mainly for its reduced CPU time consumption. This algorithm is the online version of the fitter described before. The main difference between those algorithms is that the online version relies on straight-line extrapolation of tracks and makes less use of estimate tracks uncertainties. This results on a poor efficiency for vertices further than 200 mm of the interaction point, very weakly affecting the detection efficiency for the models considered in this work (as illustrated in Figure 4.2).

In this analysis, the position of the LLP is compared to the beam line position, based on the position of the VELO<sup>2</sup> and stored for each event. Primary vertices positions for the 2011 data

<sup>2</sup>The VELO is centered around the beam at the beginning of each run.

are illustrated in Figure 4.7, showing an average radial offset of about 0.4 mm with respect to the nominal zero.

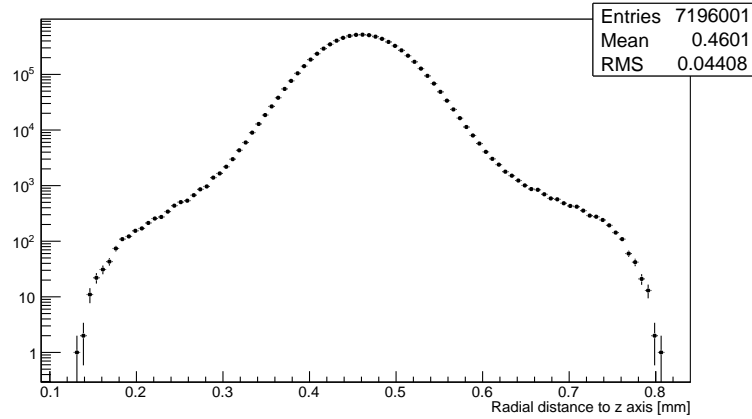


Figure 4.7: Radial position of the reconstructed primary vertices for the 2011 data.

### 4.3.2 Interaction with detector material

One of the major sources of background<sup>3</sup> when reconstructing displaced vertices comes from particles produced by interactions with detector material. To deal with this, a **matter veto** procedure has been developed. The idea is to use a map of the detector material in order to discard vertices reconstructed inside or in the immediate vicinity of parts of detector where particles can interact with the matter. Most vertices found above approximately 5 mm from the beam pipe come from matter interactions. They can clearly be identified by their position, has illustrated in Figure 4.8.

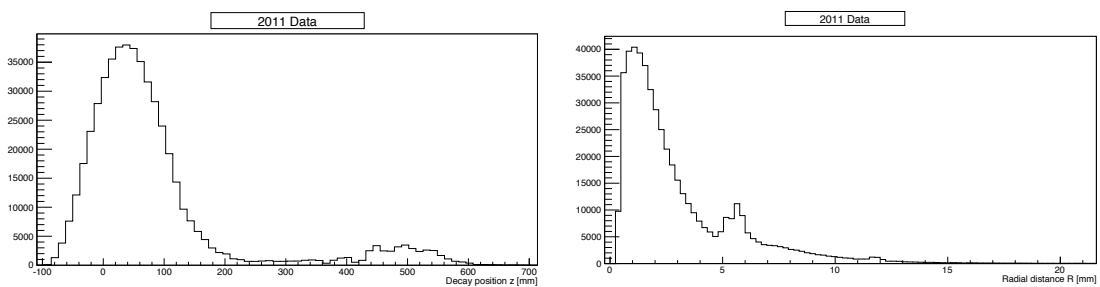


Figure 4.8: From preselected 2011 data, the longitudinal (left plot) and radial (right plot) coordinates (lab frame) of the reconstructed secondary vertices with at least four forward tracks, no backward tracks, and an invariant mass larger than  $3.5 \text{ GeV}/c^2$ . The structure is due to the production of vertices in the detector material.

<sup>3</sup>The other main sources of background originate from Primary Vertices and from beam-gas interactions. They can be suppressed by a cut on the radial position  $R$  of the vertex candidate.

## Chapter 4. Search for Long-Lived Particles

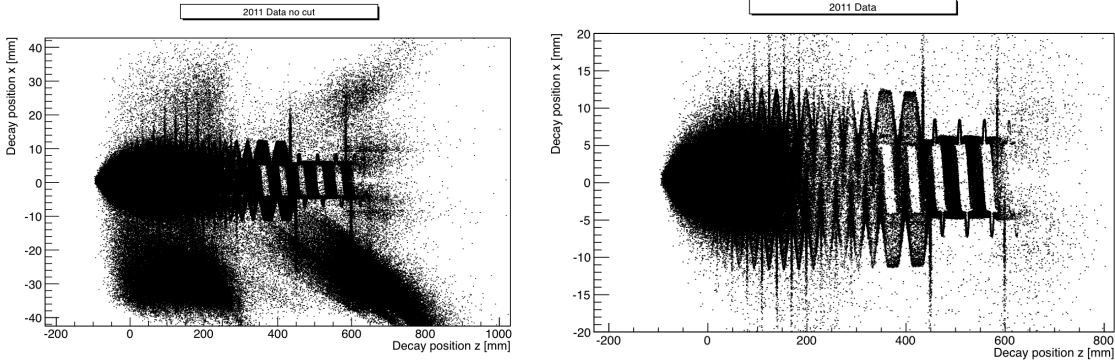


Figure 4.9: Like Figure 4.8, position of the reconstructed vertices in coordinates  $(x,z)$  (lab frame). The data without global event cut are shown in the left plot, and with the cut in the right one.

Figure 4.8 shows that the region beyond  $R \sim 5$  mm is heavily polluted by interactions with matter.

### Matter Veto description

A matter veto has been developed to remove such background by discarding vertices falling in a region with material. The detector structure is determined from real data (see [18]).

As explained in Chapter 3 section 3.3.1, the RF-shield separates the halves of the VELO from the interaction region with two aluminum foils. The geometry of the Rf-shield changes (at  $z \sim 400$  mm) from the central to the forward regions. Hence the matter veto procedure is different in those two regions.

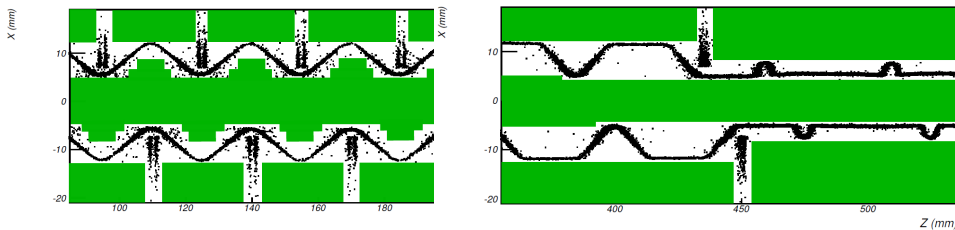


Figure 4.10: Matter distribution inside the VELO for a 1 mm slice in  $y$ , for the central (left) and forward (right) regions. The allowed area are colored in green (from [18]).

- Interactions with side corrugations are rejected by discarding vertices in the VELO region with  $|x| < 5.5$  mm (8.5 mm) and  $|y| > 10$  mm for  $z < 440$  mm ( $z > 440$  mm).
- Interactions with VELO sensors are rejected by discarding vertices with  $|z - z_{sensor}| < 1.75$  mm and a radial position bigger than 6 mm.

- In the central region, vertices with a radial displacement of less than 5 mm (4.3 mm) for  $z < 370$  mm ( $z > 370$  mm) are accepted while those in between 5 mm (4.3 mm) and 12.5 mm (8.5 mm) are rejected. Nonetheless, some exceptions are made to follow the inner corrugations for  $z < \sim 380$  mm.
- In between sensors, the volumes defined by two cylinders centered on the beam line distant from the sensors by 8 mm and 11 mm, and of radii of 7 mm and 9 mm are allowed if  $x > 4$  mm ( $< -4$  mm) for the left side (right side) sensors.

The total volume allowed by this set of cut is illustrated in Figure 4.10 by the green area. This cut has been optimized on data to reject the full RF-shield and sensor structures. Results of this procedure can be seen in Figure 4.12.

### Global Event Cuts

In 2011, a large background contribution comes from events polluted by material interactions of beam-halo upstream or downstream of the VELO, called "beam-splash". It induces near-parallel charged tracks on one side of the VELO. This affects the number of fake reconstructed vertices at large distance to the beam, as can be seen in the left plot of Figure 4.9. Therefore some global event cuts have been set to remove such events. The first condition is that the number of VELO tracks does not exceed one-tenth of the number of VELO clusters. This requirement allows to avoid too much near-parallel tracks reconstructed from the large number of hits in the polluted region. In addition, noticing that the hits associated to beam-splash particles are all close in  $\phi$  in the VELO, the vector sum in the transverse plane is defined:

$$\vec{\phi}_{\text{tot}} = \sum_{\phi \text{ hits } i} \begin{pmatrix} \cos \phi_i \\ \sin \phi_i \end{pmatrix} \quad (4.1)$$

where the sum runs over all hits in VELO  $\phi$ -strips and  $\phi_i$  is the direction of the strip. Since beam-splash events are also characterized by many hits in  $R$  strips, the quantity illustrated in Figure 4.11 is also defined:

$$D_\phi = \frac{n_\phi + n_R}{n_\phi} |\vec{\phi}_{\text{tot}}| \quad (4.2)$$

Then, the average size of the vector  $\phi$  times the number of clusters is required smaller than 250. The combined effect of those requirements can be seen on the right plot of Figure 4.9.

The global event cuts leave the signal efficiency quasi unmodified (less than 1% of signal event loss).

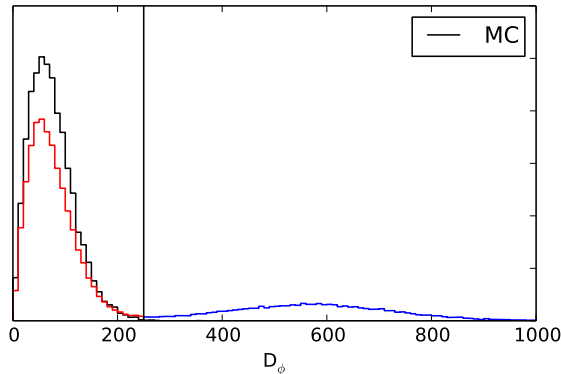


Figure 4.11: Distribution of  $D_\phi$  in simulated events (black) and 2011 data selected for the displaced vertex analysis (red and blue). The vertical line corresponds to the cut applied in the analysis (courtesy from Pieter David).

After carrying out the matter veto procedure, the scatter plots of Figure 4.12 show that most of the structure has disappeared but not completely, most likely because of reconstruction errors. For the present study the matter veto is applied for at least one candidate at the preselection stage (to keep some matter interactions for further tests). In parallel a control analysis is carried out, selecting only reconstructed vertices in the vacuum region by cutting at  $R < 4.8$  mm. In addition, a lower cut at  $R > 0.4$  mm is applied to stay away from the PV region.

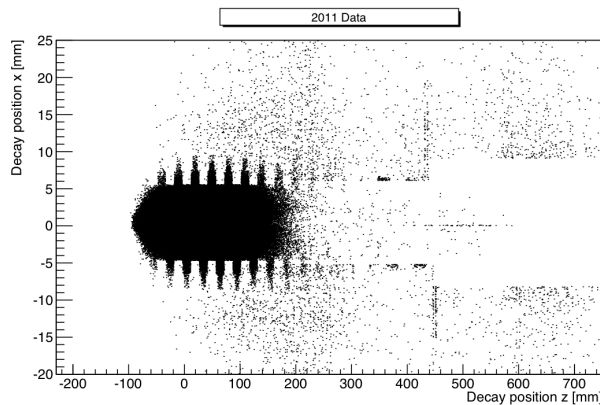


Figure 4.12: Like Figure 4.9, after the matter veto.

### 4.3.3 Event preselection

Events that have passed the triggers and the "double displaced vertices" stripping algorithms are called "preselected" events. No dedicated L0 or HLT1 triggers are implemented. Therefore, all events leading to a positive decision for any physical triggers (only events



accepted by calibrations or "non-physical" lines are rejected) are analyzed. A dedicated HLT2 trigger, "HLT2DisplVerticesDouble", exists and its configuration is given in Table 4.5. Only data starting from June 2011 are analyzed. This choice is motivated by the fact that the Hlt2DisplVerticesDouble trigger line has only been correctly set from that period (run number  $\geq 92821$ ). This requirement implies the loss of about  $0.1 \text{ fb}^{-1}$  of luminosity. The recorded luminosity that corresponds to this analysis is then  $0.9 \text{ fb}^{-1}$ .

Eight triggers configurations were used in the period considered (named TCK 0x710035, TCK 0x6D0032, TCK 0x730035, TCK 0x740036, TCK 0x760037, TCK 0x790037, TCK 0x790038 and TCK 0x561710). A comparative analysis between events filtered by these different configurations has shown no significant change on the BV48 MC sample.

The event preselection is implemented in the "ElectroWeak stripping" stream and performed by the "DoubleDisplacedVertices" stripping line.

Line name	$N_{min}^{track}$	$M_{minMass}^{LLP}$ GeV/c <sup>2</sup>	$M_{HighestMass}^{LLP}$ GeV/c <sup>2</sup>	$\text{SumpT}_{min}$ GeV/c	$R_{min}$ mm	Matter Veto
HLT2 Double	4	3	4.5	3	0.4	one candidate
Strip Double	4	3.5	4	3	0.4	one candidate

Table 4.5: HLT2 and stripping configurations in 2011 for the selection of couples of LLPs. At least one candidate must be found outside the detector material.

Two LLP candidates are requested with conditions summarized in Table 4.5. In the stripping sequences, the input tracks have quality cuts applied<sup>4</sup>. Primary and secondary vertices are found. At least one Primary Vertex reconstructed with more than 10 tracks and at least 1 backward and 1 forward tracks is requested. Its radial position should be at a maximum of 0.3 mm from the beam line position. While the number of tracks required to reconstruct both candidates is the same for HLT2 and stripping, the conditions applied on the masses are rather different for both contexts. It has been found that to respect the retention rate constraint of HLT2, the cut on the mass of the heaviest vertex had to be pushed to  $4.5 \text{ GeV}/c^2$ . The  $\text{SumpT}_{min}$  cut is applied to the scalar sum of transverse momenta of the LLP tracks. The candidate with the highest mass has to be found outside the detector material. The response of the Matter Veto for the second candidate is stored and can be used later on to perform cross checks, whenever a set of vertices coming from matter interactions is needed.

Figure 4.13 illustrates the effect of the Matter Veto procedure on preselected MC events. True MC values are used to define the coordinates of the PV and of the LLP vertices and it is necessary that the decay leaves at least 6 charged particles in the acceptance. The efficiency is defined as the number of reconstructed vertices divided by the number of vertices from MC truth. Small differences in the efficiencies can be observed out of the matter region when

<sup>4</sup>These tracks are all the reconstructed tracks from the */Rec/Track/Best* list.

the reconstructed position of the vertex is different from the true MC position. To get rid of this effect while preserving enough statistics, the reconstructed radial position must lie at a maximum of 0.05 mm from the MC true radial position of the corresponding LLP. The reconstructed vertex is declared detected when reconstructed with at least four forward tracks and no backward track (the cuts on the mass and the distance to the beam are not active). The plots of Figure 4.13 are made from the addition of four BV48 models with respectively 5, 10, 15 and 50 ps LLP's lifetimes.

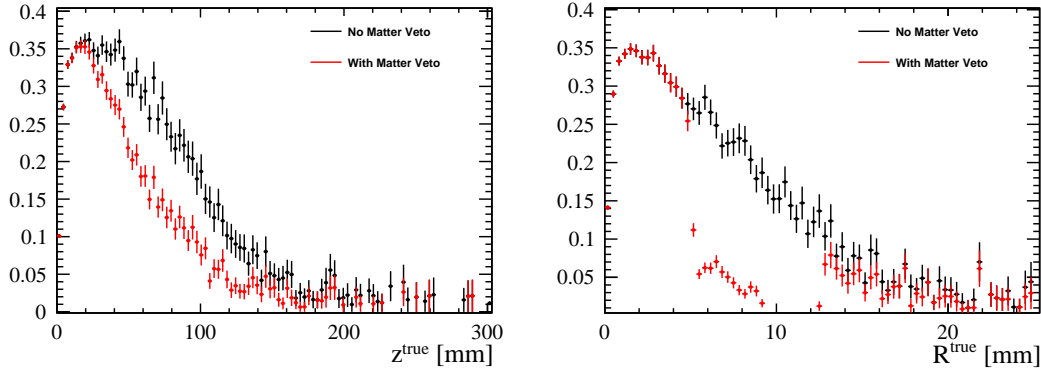


Figure 4.13: Efficiency to find a (MC-true) LLP secondary vertex as a function of its distance from the PV. The left figure gives the efficiency as a function of the (true) longitudinal PV-RV distance  $z^{true}$ . The right plot shows the true radial distance  $R^{true}$ . The red points have the "matter veto" activated, to discard vertices produced by interactions of particles with the detector material. Here at least 6 charged particles to form the vertex are requested.

### Analysis of preselected events

In the following, events with two LLPs both falling outside the matter region are selected.

Figure 4.14 presents the number of tracks that have been used to reconstruct the vertex candidate, the reconstructed transverse momentum of the LLP, the reconstructed mass of the candidate and the radial distance to the beam line of the reconstructed vertex. The data (selected by all the physics trigger lines) are compared to BV48 and HV10 models and to  $b\bar{b}$  inclusive MC. The distributions are normalized to unity. The form of the inclusive b sample matches well the data as already observed in [18]. Notice the effect of the Matter Veto procedure in the R plot.

The variables  $\sigma_R$  and  $\sigma_Z$  of Figure 4.15 correspond to the position uncertainties provided by the vertex algorithm. Those are two variables of crucial importance to distinguish signal from background events. It appears that the error on the position is smaller for signal than for  $b\bar{b}$  events. This effect may be proportional to the mass of the LLP that decays producing less parallel tracks creating a better reconstructed vertex. Again, the shapes of data and beauty events match well. The value of the vertex error is related to the number of tracks, as can be

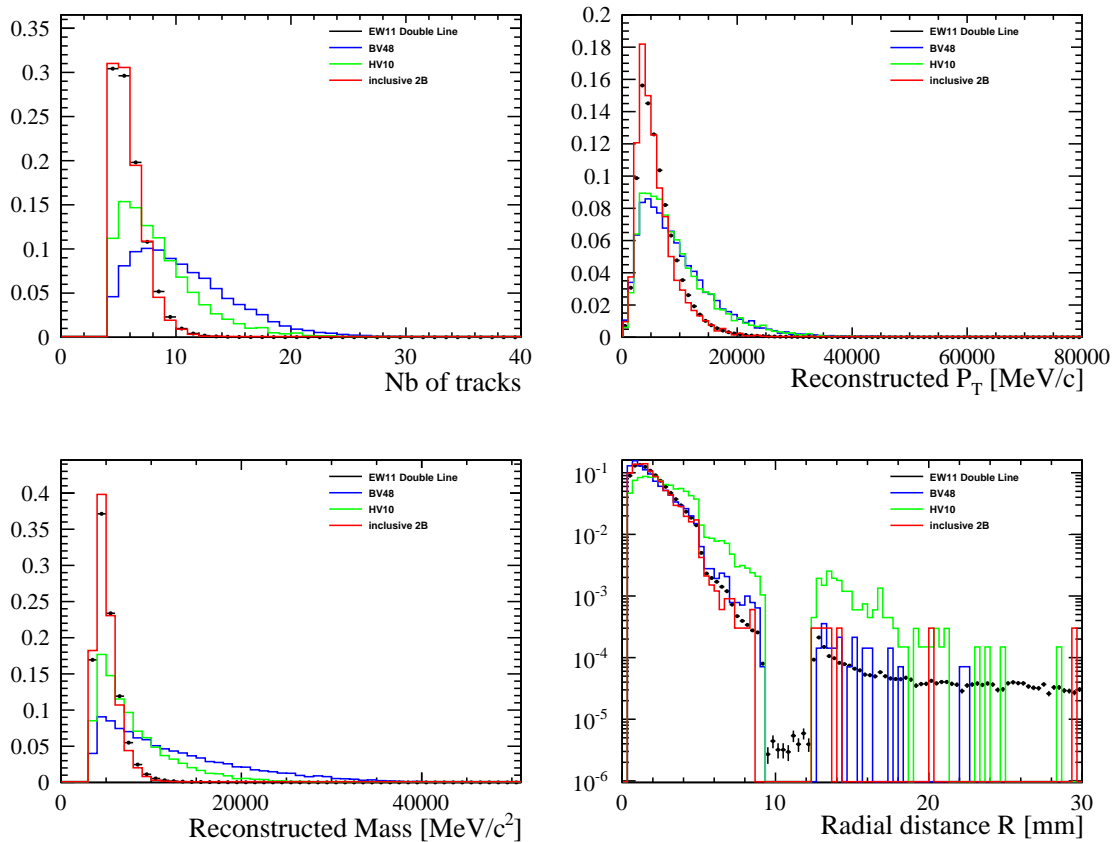


Figure 4.14: MC events compared to data results. Distributions of (top left) the number of tracks of the LLP candidate, (top right) the transverse momentum, (bottom left) the invariant mass, and (bottom right) the radial distance to the beam line in logarithmic scale are shown. Data and MC distributions are shown with unit normalization. The plots contain  $121 \cdot 10^3$  events from data analysis, and about 1600 events of the special  $b\bar{b}$  MC sample. Each plot has two LLPs per event.

seen in the profiles of Figure 4.16. In general, the two  $\sigma$  decrease with the number of tracks but, in the data, the dependency is inverted after 10 tracks. This is an highlight that a displaced vertex can be made of wrongly associated tracks. A track from the PV can be amalgamated to the displaced vertex when passing close to it, increasing the error on the position by worsening the vertex fit.

The angle between the two LLP candidates is considered in Figure 4.17. The difference between background and signal is clearly shown and the beauty events match well the data. This angle is computed from the associated PV to the LLP vertices rather than from the momenta. In case of multiple PVs, the momentum vectors of the two candidates is extrapolated in order to find their point of closest approach. Then, this point is compared to the list of primary vertices and the closest PV is chosen.

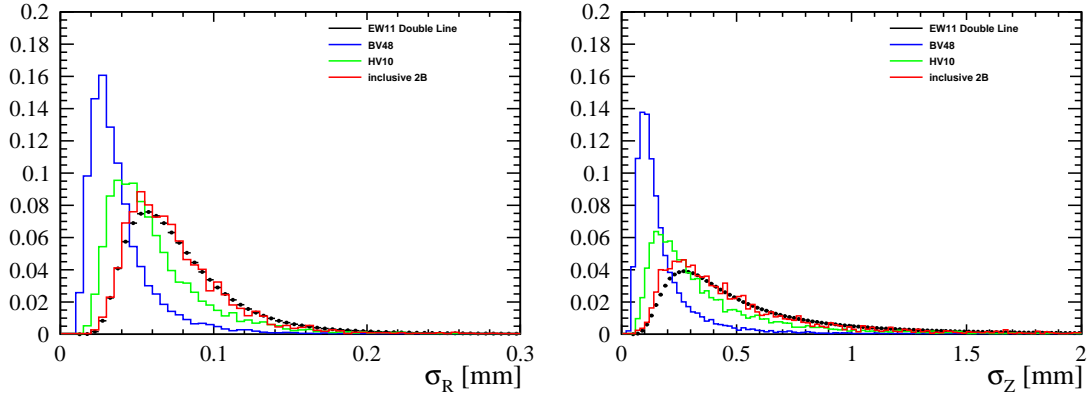


Figure 4.15: Radial and longitudinal errors on the LLP vertex, provided by the vertex algorithm, for data and MC events.

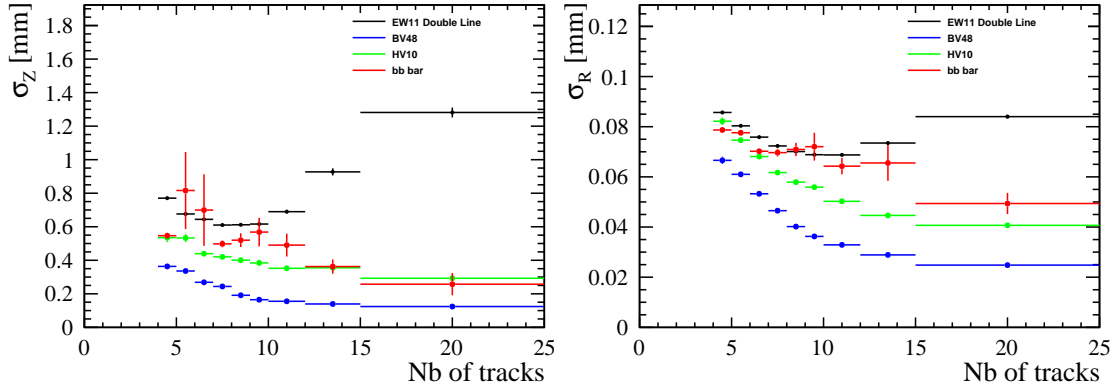


Figure 4.16: Average error in Z (left) and R (right) versus number of tracks in the vertex. The difference between HV and BV seems associated with the quark composition of the decay of the LLP: HV contains only b quarks, while BV produces also light quarks.

Figure 4.18 presents the distance of flight of the LLP candidates with respect to the associated PV. Again, the distribution of  $b\bar{b}$  events is well compatible with what is observed in the data.

### 4.3.4 Higgs-like boson reconstruction

To reconstruct the mother Higgs-like boson, two LLP are combined. 2035034 events have at least one Higgs candidate. A fraction (0.6%) of events has more than two LLP candidates. The mass and  $p_T$  distributions for the combination of two LLPs are shown in Figure 4.19. In the case where more than two LLP candidates are found in the event, the combination is made with the two candidates having the largest reconstructed transverse momentum.

The same procedure is applied to the signal and background MC samples. The situation at this

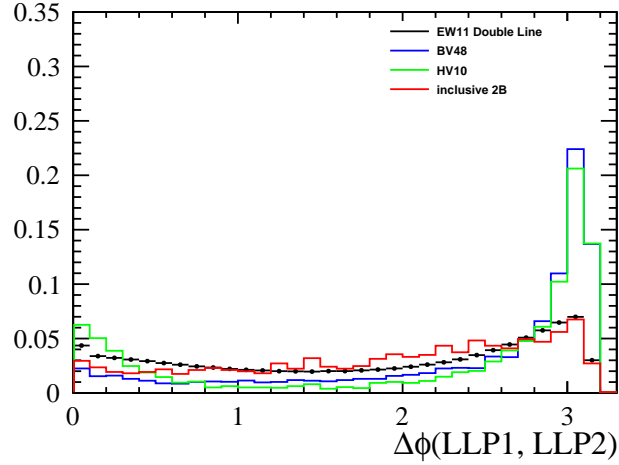


Figure 4.17:  $\Delta\phi$  angle between the two LLP candidates for data and MC distributions normalized to unity. Black points are the data,  $b\bar{b}$  MC events in red and BV and HV signal MC events in blue and green respectively.

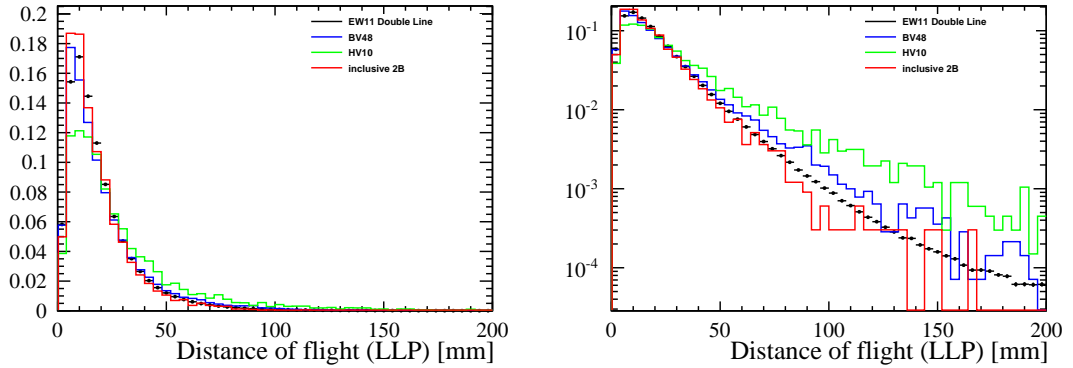


Figure 4.18: Linear and log distributions of the distance of flight of the LLP candidates. Data in black,  $b\bar{b}$  MC events in red and the BV signal in blue. Data and MC distributions normalized to unity.

stage of the analysis is presented in Table 4.6 for  $b\bar{b}$  inclusive events, special  $b\bar{b}$  production,  $t\bar{t}$  and special  $c\bar{c}$ . The MC information can be used to estimate the detection efficiency and to predict the number of  $b\bar{b}$ . The experimental inclusive  $b\bar{b}$  cross section values measured by LHCb are [20, 21]:  $284 \pm 20 \pm 49 \mu\text{b}$  and  $288 \pm 4 \pm 48 \mu\text{b}$  (the first uncertainty is statistical and the second systematic). The value of  $287 \pm 40 \mu\text{b}$  is adopted for the tests.

If we consider only events passing our dedicated HLT2 trigger line, 132129 events are selected. This additional requirement selects 37 MC  $b\bar{b}$  events allowing us to predict  $(121 \pm 20) \times 10^3$  data events. The events selected in the  $c\bar{c}$  sample all contain b decays and are therefore a subset of inclusive b events. The same applies for the two events selected from the  $t\bar{t}$  sample. Compared

## Chapter 4. Search for Long-Lived Particles

with the number actually measured, it appears that mainly beauty events are selected in this particular region of phase space. This conclusion was also made for the 2010 data analysis, with a larger MC statistics available at that time.

MC kind	Generated	Selected
$b\bar{b}$ inclusive	200.6 k	0
$b\bar{b}$ special	17.1 M	37
$t\bar{t}$	510 k	2
$c\bar{c}$ special	9.15 M	3

Table 4.6: Statistics at the input of the procedure for Higgs selection for the MC background sets. A positive decision from the HLT2 double trigger is required.

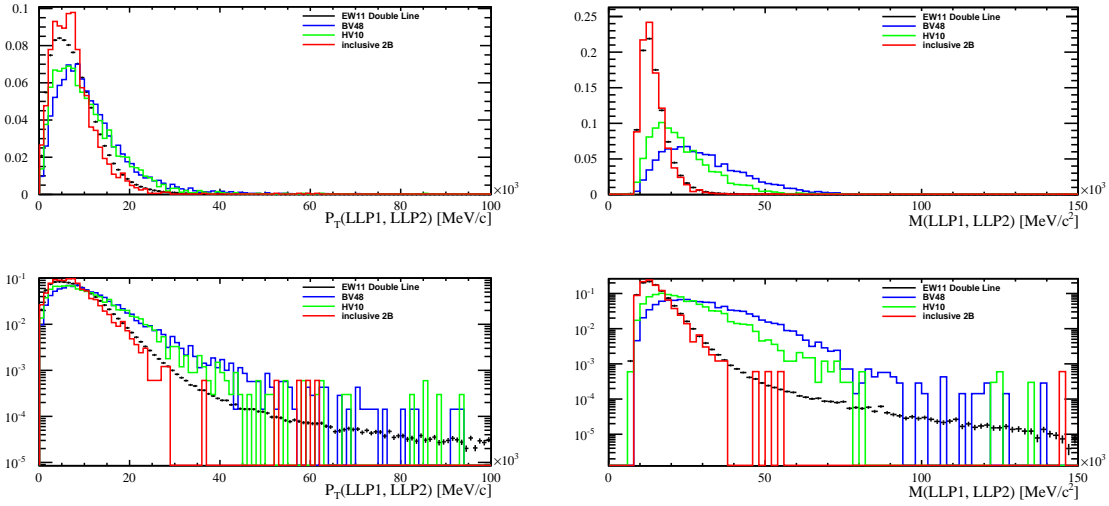


Figure 4.19:  $p_T$  distribution (left column), and invariant mass (right column) for the Higgs candidates. Result for MC signal and  $b\bar{b}$  events are shown with unit normalization. Plots at the bottom have log scale. Black dots are data, red:  $b\bar{b}$  distributions, blue: BV signal, and green: HV.

Different set of cuts have been tested to purify the data sample while preserving an acceptable efficiency for the considered signals. Table 4.7 shows the evolution of the selected number of events for increasingly stronger cuts and Table 4.8 gives a comparison with the predicted background assuming pure  $b\bar{b}$ .

The Higgs is produced with rather small transverse momentum (as shown in Figure 4.1) and therefore its decay products are almost produced back to back as illustrated in Figure 4.17. This allows to purify the signal by a selection of  $\Delta\phi > 2.8$ .

The HLT2 double trigger line is rather efficient to suppress the  $b\bar{b}$  background, see Appendix A for a discussion of this point. Also notice that the predictions given in Table 4.8 for events that

Selection	Data	$\bar{b}\bar{b}$ 2 B-hadrons in acceptance
Generated:	-	17.1 M
$R > 0.4$ mm, one MV, triggered	3211815	2237
$R > 0.4$ mm, two MV, triggered	2035034	1659
$R > 1$ mm, two MV, triggered	1227807	959
$0.4 < R < 4$ mm, one MV, triggered	1740597	1442
$1 < R < 4$ mm, one MV, triggered	1001702	804
$R > 0.4$ mm, two MV, $\Delta\phi > 2.8$ , triggered	452170	328
$M_{min}^{LLP}=4$ , two MV, HLT2_phys	1345942	1054
$M_{min}^{LLP}=4$ , two MV, HLT2 Double	94654	30

Table 4.7: Number of events at different selection stages for data and MC background. MV stands for the matter veto. For the MC sample, the number of generated events is also given. Triggered means that one of the HLT2 physical lines must give a physical decision. The bottom part of the table is specifically for HLT2 comparison. Only the more restrictive conditions are presented here.

Selection	Data	$\bar{b}\bar{b}$ 2 B-hadrons in acceptance
$R > 0.4$ mm, one MV, HLT2 Double	371207	75 (246008 $\pm$ 28407)
$R > 0.4$ mm, two MV, HLT2 Double	132129	37 (121364 $\pm$ 19952)
$0.4 < R < 4$ mm, two MV, HLT2 Double	110635	29 (95124 $\pm$ 17664)
$R > 0.4$ mm, two MV, $\Delta\phi > 2.8$ , HLT2 Double	31107	6(21868 $\pm$ 8035)
$R > 0.4$ mm, two MV, $\Delta\phi > 2.8$ , HLT2_phys	452170	328 (1075879 $\pm$ 59405)

Table 4.8: Number of events at different selection stages of the analysis (see Table 4.7), compared to MC predictions between brackets, assuming a pure  $\bar{b}\bar{b}$  background.

pass any of the HLT2 physical lines is unsatisfactory. This is probably due to differences in the emulation of some of the trigger lines in the Monte Carlo samples, compared to data.

Table 4.9 gives the total selection efficiencies for the HV10 and BV48 models for various combinations of cuts in addition to a R cut set at 0.4 mm and considering only events passing the HLT2 double trigger line. The selection presented in line 6 will be used in Chapter 5 as the most restrictive selection.

## Chapter 4. Search for Long-Lived Particles

	$N_{min}^{track}$	$M_{min}^{LLP1}$	$M_{min}^{LLP2}$	$\sigma_R^{max}$	$\sigma_Z^{max}$	MV	$N_{evts}$	$\epsilon^{HV10}$ [%]	$\epsilon^{BV48}$ [%]
1	4	3.5	4	$\infty$	$\infty$	One	72313	1.67	1.12
2	4	3.5	4	$\infty$	$\infty$	Both	31107	1.09	1.03
3	4	3.5	4	$\infty$	$\infty$	One, $R < 4.8$	30951	1.03	1.01
4	5	5	5	$\infty$	$\infty$	Both	15159	0.798	0.906
5	8	7.5	7.5	0.1	1.0	Both	57	0.274	0.549
6	6	6	6	0.05	0.25	Both	65	0.143	<b>0.626</b>
7	6	6	6	0.05	0.25	One, $R < 4.8$	65	0.132	0.617
8	6	6	6	0.06	0.25	Both	86	0.168	0.647
9	6	6	6	0.04	0.25	Both	30	0.09	0.535
10	6	6	6	0.05	0.26	Both	78	0.150	0.634
11	6	6	6	0.05	0.24	Both	51	0.139	0.603

Table 4.9: Number of data events selected for some values of  $N_{min}^{track}$  and  $M_{min}^{LLP1/2}$  (in  $\text{GeV}/c^2$ ), and  $\sigma_R^{max}$ ,  $\sigma_Z^{max}$  (in mm). The 7th column (MV) says that the material veto was active for only one or both candidate. Alternatively, the restriction applied on the radial position of the second vertices (in mm) is indicated. For each set of cuts, the LLP candidates have a minimum radial distance of 0.4 mm.  $\epsilon^{BV48}(\epsilon^{HV10})$  is the efficiency in percent estimated from the analysis of BV48 (HV10) events. The events are requested to pass the HLT2 double trigger line and a cut of 2.8 radians is made on the angle  $\Delta\phi$  formed by the pair of LLPs.

### 4.4 Contribution to the detection efficiency and systematics effects

An estimate of the efficiencies and related systematic uncertainties is presented in this section, following and re-interpreting the work presented in [18]. Similar results are obtained, the situation being very close in 2010 and 2011.

The determination of the detection efficiency is based on the analysis of MC events and, therefore, it is important to estimate the discrepancy that can exist between MC simulation and data. The main point is the vertex reconstruction, for which the efficiency has to be determined in a region which is beyond the average b-hadron decay.

	Source	$\epsilon$ [%]
1	one LLP in acceptance (generator cut)	28.4
2	LLP preselection (Stripping Double)	14.16
3	Matter veto on the second LLP	88
4	Trigger (L0, HLT1 and HLT2 double)	49.5
5	LLP final selection	35.7
	Total	0.626
	Total w/o trigger	0.876

Table 4.10: Contributions to  $\epsilon$  at different stages of the event selection, based on MC BV48 events and with the cuts given on line 6 of Table 4.9.

Table 4.10 presents the contributions to the detection efficiency of different items, computed



#### 4.4. Contribution to the detection efficiency and systematics effects

from the BV48 model and with the selection detailed on line 6 of Table 4.9. Table 4.11 gives the total detection efficiency for various signal models. One can see, compared to the 2010 analysis, an increase of efficiency by a factor 1.6, essentially due to an improvement of the trigger selection (about 15 to 20%) and a better vertex reconstruction.

Model	Total $\epsilon$ [%]
BV48	$0.626 \pm 0.017$
BV48-5	$0.356 \pm 0.013$
BV48-15	$0.661 \pm 0.018$
BV48-50	$0.307 \pm 0.012$
BV20-10	$0.023 \pm 0.003$
BV35-10	$0.343 \pm 0.012$
BV48-mh100	$0.372 \pm 0.014$
BV48_mh125	$0.399 \pm 0.007$
HV10	$0.143 \pm 0.015$

Table 4.11: Total detection efficiency  $\epsilon$  for MC BV and HV models with selection cuts corresponding to line 6 of Table 4.9 given with statistical uncertainties.

##### 4.4.1 Trigger efficiency studies

The goal is to validate the MC trigger simulation by comparing its behavior for event kinematics which are similar to the expected signal. The method is comparable to the one presented in [18]. Again the main sources of events will be  $b\bar{b}$  events. The background from interaction with the detector material is suppressed by switching on the matter veto procedure for both candidates.

##### L0

The L0 trigger has been found to be about 95% efficient on BV48 events with the criteria of line 6 of Table 4.9 .

##### HLT1

In the case of HLT1, the relative consistency of different categories of lines for data and MC events is tested. Several analysis in which events have a positive decision from e.m. triggers (photon or electron), or muonic triggers, or the addition of hadronic lines and the "trackAll" line have been made. Results are shown in Table 4.12 for three sets of increasingly restrictive analysis conditions. Data and MC  $b\bar{b}$  events populations in the different sectors are very close, within 10-20%. Unfortunately, the statistical error is large due to a lack of beauty MC events.

## Chapter 4. Search for Long-Lived Particles

	analysis 1 [%]		analysis 2 [%]		analysis 3 [%]	
	data	MC	data	MC	data	MC
HLT1 has muons	22.8 ± 0.2	30.4 ± 11.5	20.1 ± 0.2	20 ± 11.5	19.6 ± 0.6	-
has trackAll or hadron	95.4 ± 0.4	91.3 ± 19.9	95.5 ± 0.4	86.7 ± 24	96.9 ± 1.2	-
has photon or electron	9.7 ± 0.1	4.35 ± 4.35	10 ± 0.1	6.7 ± 6.7	9.8 ± 0.4	-

Table 4.12: Comparison between data and MC fraction of events which are selected by categories of HLT1 lines, for different analysis conditions. The three analysis have  $\sigma_R=0.1$  mm and  $\sigma_Z = 1$  mm. Analysis 1 has  $N_{min}^{track}=4$ , and  $M_{min}^{LLP}=4$  GeV/c<sup>2</sup>; 73kevents have been found in data and 23 MC. Analysis 2 has  $N_{min}^{track}=5$ , and  $M_{min}^{LLP}=4$  GeV/c<sup>2</sup> 52kevents data, and 15 MC. Analysis 3 has  $N_{min}^{track}=5$ , and  $M_{min}^{LLP}=6$  GeV/c<sup>2</sup> 39kevents data, and 0 MC.

	MC J/ψ	Data
at least one LLP	88319	3049713
and at least one selected J/ψ	27082	1736187
and two LLP	102	8606
two LLP passing the selection	63	5040
HLT2Double triggered	1 (± 1.65)	499(± 41.6)
HLT2Double efficiencies	1.6 ± 3.1 %	9.9 ± 0.83 %

Table 4.13: Number of events at different stage of the analysis for the J/ψ MC sample and the 2011 Data. The HLT2DiMuonJpsi trigger line is used to filter the data events and a single loose candidate with  $N_{min}^{track}=4$ ,  $M_{min}^{LLP}=3$  GeV/c<sup>2</sup>,  $R_{min}^{LLP}=0.4$  mm (and  $\Sigma pT_{min}=3$  GeV/c) is reconstructed. Furthermore, the J/ψ is required to be prompt (ie to decay at a maximum radial distance R < 0.4 mm).

### HLT2

Because the *TISTOS* procedure<sup>5</sup> is not implemented for our type of signal candidate, the idea is to use an independent trigger as a sampling tool. The ideal trigger is the J/ψ prompt algorithm. Given the fact that the amount of such events is scarce in the  $b\bar{b}$  MC sample, a large set of MC inclusive J/ψ is analyzed. First, events triggering the "HLT2DiMuonJpsi" trigger are selected ([23] for details on this specific trigger). This trigger is prescaled by 20 %, it requires two good muons (track  $\chi^2/ndf < 5$ ) forming two vertices (vertex  $\chi^2 < 25$ ) and a mass window of 120 MeV/c<sup>2</sup> around the J/ψ mass.

Then, a dedicated stripping algorithm looks for candidate vertices with quite loose conditions:

- at least 4 charged tracks
- a minimal mass of 3 GeV/c<sup>2</sup>
- a radial distance to the beam line of at least 0.4 mm
- a minimal sum  $p_T$  of the combined tracks of 3 GeV/c

<sup>5</sup>For a standard example of trigger systematics study see [22].

#### 4.4. Contribution to the detection efficiency and systematics effects

To ensure that the sampling of events is independent from a typical displaced vertices sample, the  $J/\psi$  is required to be prompt. Hence, its decay must happen at a radial distance smaller than 0.4 mm from the beam line, see Figure 4.21. It is also possible to ask for the  $J/\psi$  to be the particle which activated ("TOS") the HLT2DiMuonJpsi trigger line as well as all the HLT1 muon lines and the L0 muon triggers. Comparisons between MC and data mass and radial distributions of the  $J/\psi$  are made and distributions of the reconstructed LLP are given in Figure 4.20.

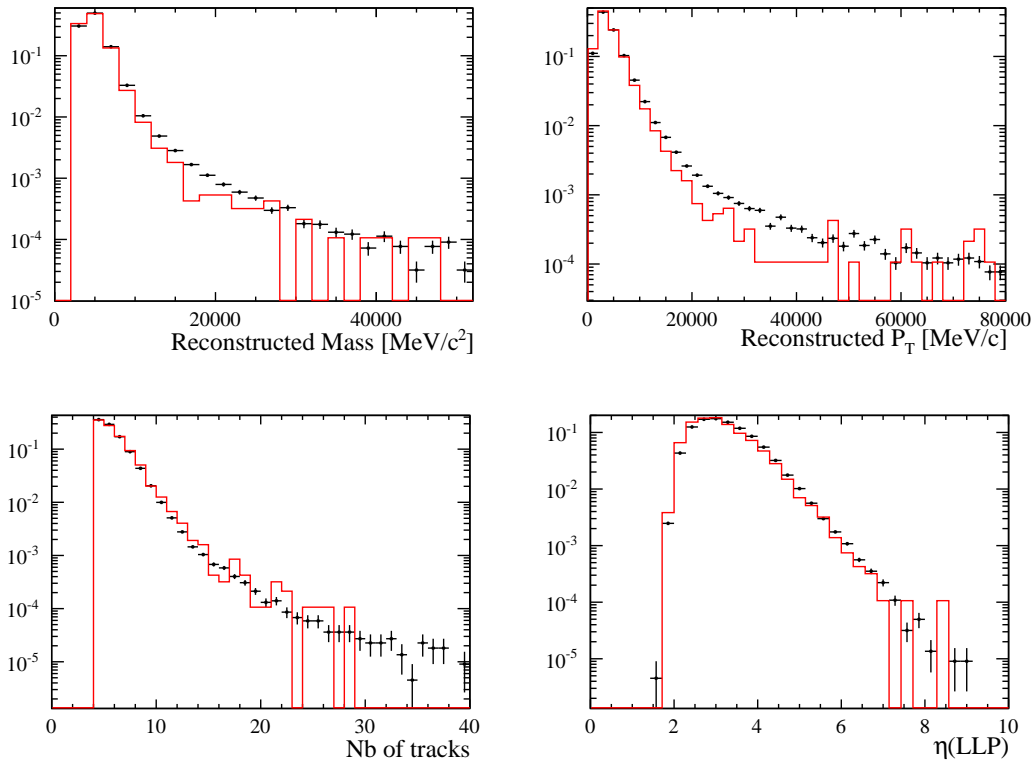


Figure 4.20: Reconstructed invariant mass  $M$ , transverse momentum  $p_T$ , number of tracks, and pseudorapidity of the single loose LLP candidates. The dots represent the data, the histogram is the result for the MC  $J/\psi$ . The distributions have been normalized to unity. The analysis requires an HLT2 Dimuon  $J/\psi$  positive decision.

Conditions comparable with the HLT2 double line are imposed: two LLPs satisfying  $N_{min}^{track}=4$ ,  $M_{min1}^{LLP}=4.5 \text{ GeV}/c^2$ ,  $M_{min2}^{LLP}=3 \text{ GeV}/c^2$ ,  $R_{min}^{LLP}=0.4 \text{ mm}$ , and the first LLP must be found outside of the detector material. The number of events at each stage of the analysis is given in Table 4.13. Unfortunately, only one event survives in the MC sample, and this does not allow to draw significant conclusion. Nevertheless, in the more favorable analysis of 2010, the result was that MC and data were in agreement within a statistical precision of 15 %. There is no reason to believe, looking at the overall good agreement between MC and data distributions, that the situation is different in 2011. The same 15% systematics as in 2010 is therefore assumed. Considering that the trigger is now 70% efficient, compared to the 40% of 2010, a

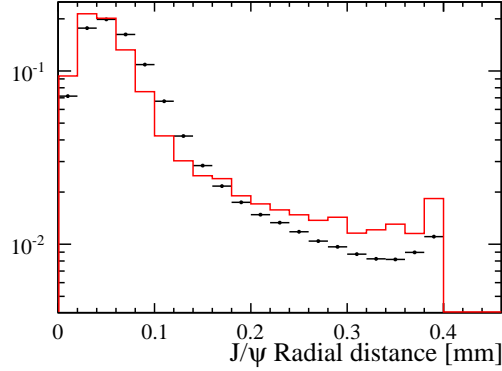


Figure 4.21: Radial distance to the beam line of the reconstructed  $J/\psi$  with the requirement of the HLT2 DiMuon  $J/\psi$  positive decision. The dots represent the data, the histogram is the MC  $J/\psi$  prediction. The distributions have been normalized to unity.

15% systematics can be considered as a conservative estimate.

#### 4.4.2 Systematic uncertainties

Table 4.14 summarizes the contributions of the systematics uncertainties to the detection efficiencies.

	Source	%
1	Integrated Luminosity	3.5
2	Trigger	15
3	Track reconstruction	5
4	VELO tracks	5
5	Vertex reconstruction	9.5
6	$p_T$ and mass calibration	6
7	Matter veto	4
8	Beam line position	1.5
	Total	21

Table 4.14: Contributions to the error on the efficiency, assuming the BV48 model.

The different contributions are :

- The discrepancy between the simulation and the implementation of the trigger selection is assumed to be at most 15%.
- By comparing the distributions presented in Figure 4.14 for the number of tracks between MC  $b\bar{b}$  and the data, the observed difference in track reconstruction is assumed to contribute at most by 5% to the uncertainties.

#### 4.4. Contribution to the detection efficiency and systematics effects

---

- When VELO tracks with no momentum information are used, a default  $p_T$  value of 400 MeV/c is assigned. A difference in the number of VELO tracks between data and MC might introduce a bias. This has been evaluated at 5%.
- Figure 4.15 shows that the calibrations in the vertex reconstruction errors are in good agreement ( $\pm 0.01$  mm) when comparing data and MC  $b\bar{b}$ . Taking half the difference between lines 8 and 9 of Table 4.9 gives a 9% contribution and half the difference between lines 10 and 11 gives a 2.5% contribution. By adding them quadratically, a 9.5% systematics uncertainty is assigned.
- A maximal mismatch of 10% in  $p_T$  and mass calibration is inferred from Figure 4.14. By moving the cuts by this amount, the difference in efficiency is of 6%.
- A study has been made for the 2010 data in which the matter veto has been switched off and a control region,  $1 < R < 4$  mm, has been set. The corresponding uncertainty has been found to be 4%. Because it is impossible to totally de-activate the Matter Veto in 2011 and by looking at the results presented in Table 4.7 showing that the Matter Veto description is very close to the 2010 description, the 4% value is kept.
- Assuming a 1% inaccuracy in the position of the beam line, a 1.5% systematic is added by estimating its effect on the radial cut of the LLP.



# 5 Extractions of the Signal Yield from the 2011 Selected Events

Extracting physical results from the 2011 data is a delicate operation. Indeed, no satisfactory background model exists despite the fact that it is strongly reasonable to believe that the main Standard Model component comes from  $b\bar{b}$  events. Unfortunately, the production of  $b\bar{b}$  events corresponding to 2011 data is of only 17 M events, while in 2010 there existed 100M events along with trigger conditions that were much less restrictive. To partially cope with this fact, specially biased events were produced to foster the MC LLP candidates yield.

The following chapter presents some attempts to extract the signal component from the 2011 data based on fitting variables distributions, on an ABCD statistical method and on a multivariate analysis using a Neural-Network(NN) events classifier. Finally, examples of calculations of upper limits on the production cross-sections of long-lived particles are given.

Four different selections have been implemented, dubbed s1, s2, s3 and s4. The selection s1 corresponds to the stripping output. Details of the selections criteria are given in Table 5.1.

selection	$N_{min}^{track}$	$M_{min}^{LLP}$ GeV/ $c^2$	$\Delta\phi_{min}$ rad	N data 2011
s1	presel	presel	presel	131129
s2	4	4	2	51243
s3	5	5	2	15159
s4	6	6	2.8	65

Table 5.1: Different scenarii of cuts for the selection of events. In addition  $R > 0.4$  mm is imposed on both candidates and the requirement of a HLT2Double trigger line positive decision can be added. Cuts on  $\sigma_R$  and  $\sigma_Z$  are not applied except for s4 that requires  $\sigma_R < 0.05$  mm and  $\sigma_Z < 0.25$  mm.

## 5.1 Fitting of key variables distributions

Different distributions have been fitted and are presented in the following. The di-LLP invariant mass as well as the  $\Delta\phi$  angle between the pair of candidates have been considered. It has

also been noticed that combining the di-LLP invariant mass and the vertex fit uncertainties of the two LLPs is a good way to distinguish signal from background events.

The fitting procedure consists on adjusting to the data distribution a theoretical shape which contains a signal component and a background component. The total number of events is constrained to the data. Because the number of events in the MC  $b\bar{b}$  sample is limited, the cuts are kept open and the requirement of the HLT2 Double line selection is not requested. Of course, this implies a risk of biasing the theoretical shape but produce a statistically significant background model.

### 5.1.1 The mass of the di-LLP

The distribution of the di-LLP mass is clearly cut dependents, as can be seen in Figure 5.1. The figure was obtained with the sets of cuts of the Table 5.2. The low masses are suppressed by increasingly stronger cuts which move the center of gravity toward higher mass values.

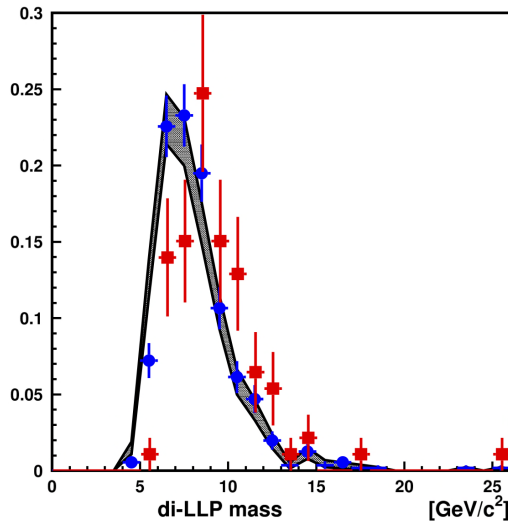


Figure 5.1: Comparison of di-LLP invariant mass distributions for  $b\bar{b}$  MC events selected by increasingly stronger cuts. The grey (1 sigma) band corresponds to condition bb1, blue dots to bb2, and red squares to bb3. The distributions are normalized to one. The statistical uncertainties are correlated.

An attempt to compensate for the bias that appears when using different cuts conditions for data and the  $b\bar{b}$  selection is to leave free the position along the mass of the background pdf. The resulting shift which gives the best fit results is found in the range of 0 and 2 channels. Results of this procedure with 2011 data are given in Figure 5.2 and the corresponding numerical results are given in Table 5.3.



## 5.1. Fitting of key variables distributions

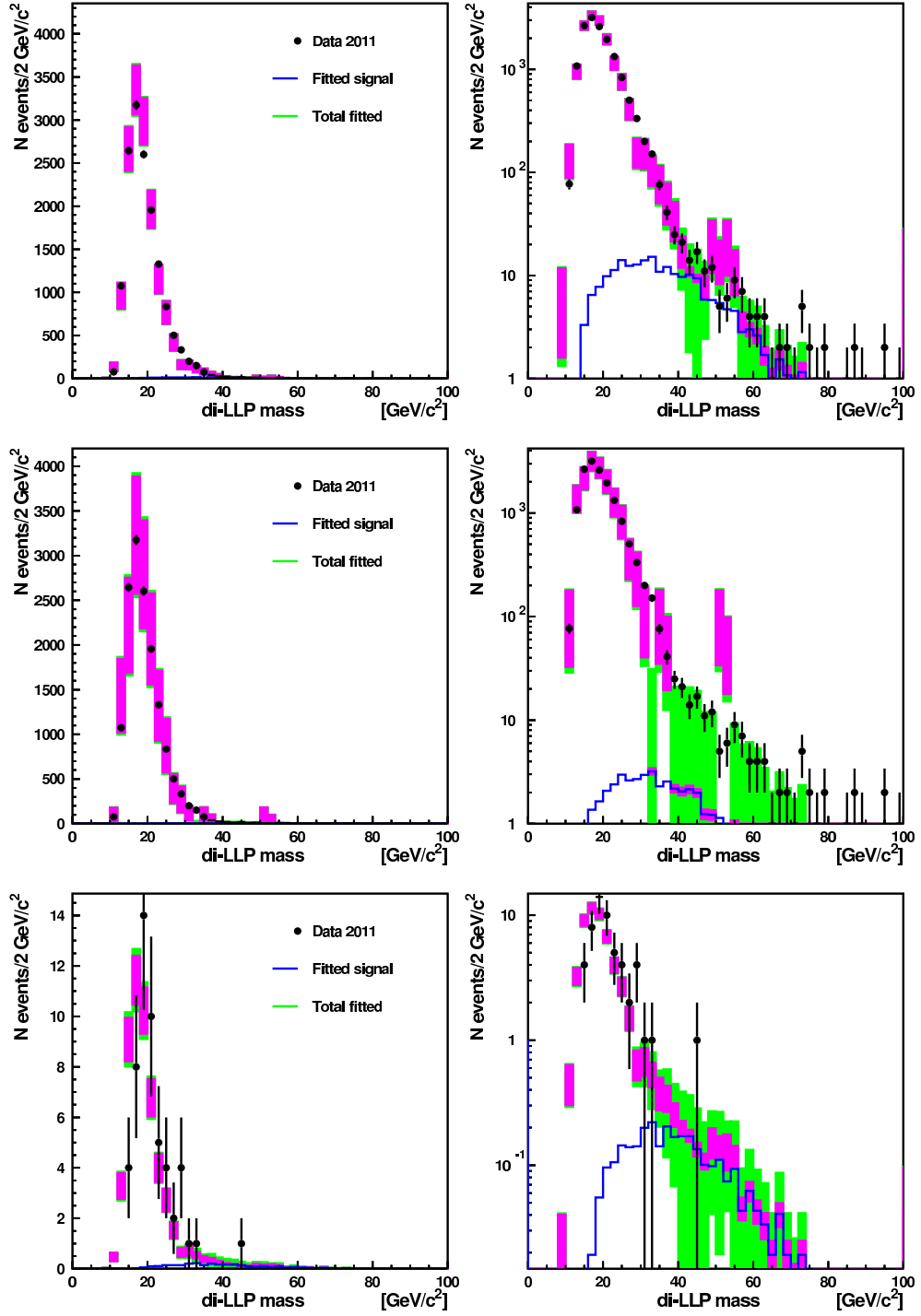


Figure 5.2: Results of the fit of the di-LLP invariant mass distribution for the data events selections given in Table 5.3, linear scale on the left, log scale on the right. The signal component is BV48, the background events are  $b\bar{b}$  MC events selected by the sets of cuts described in the text. The purple error rectangles are the statistical uncertainties propagated from of the original  $b\bar{b}$  events sample and the green rectangles represent the fit uncertainty.

selection name	$N_{min}^{track}$	$M_{min}^{LLP}$	$N_{bb}$
bb1	preSEL	preSEL	877
bb2	4	4	554
bb3	5	5	93
bb4	6	6	0

Table 5.2: Details of the different selections for  $b\bar{b}$  MC events. All HLT2 physical trigger lines have been activated, and  $\Delta\phi > 2$  is imposed.

	data selection	$b\bar{b}$ selection	$N_{data}$	$N_{signal}^{BV48}$	$\chi^2/DoF$
1	s3	bb2	15176	215 (+188, -194)	1.56
2	s3	bb3	15176	45 (+385, -403)	0.50
3	s4	bb2	54	0.7 (+3.4, -3.3)	0.95

Table 5.3: Results of the fit of the di-LLP invariant mass.

### 5.1.2 $\Delta\phi$ angle between the two LLPs

The  $\Delta\phi$  distribution for  $b\bar{b}$  events does not display a significant dependence on the cuts used in the selection. Figure 5.3 shows the comparison of  $\Delta\phi$ , for the bb1, bb2, bb3 selection conditions (without the  $\Delta\phi$  cut).

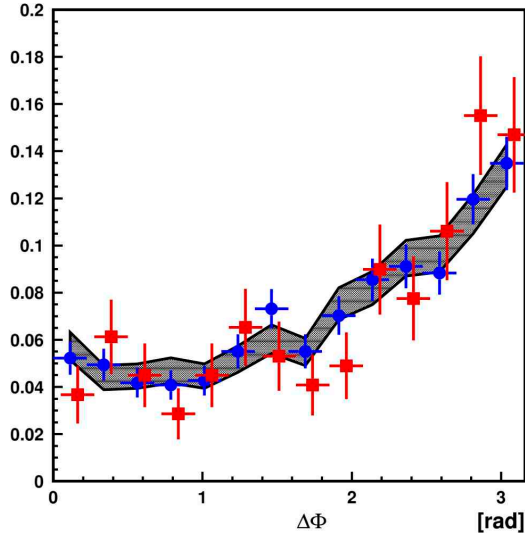


Figure 5.3: Comparison of  $\Delta\phi$  distributions for  $b\bar{b}$  events selected by three different analysis conditions. The grey (1 sigma) band corresponds to condition bb1, condition bb2 is shown by blue dots, and bb3 by red squares. The distributions are normalized to one. The errors of the three distributions are correlated.

Assuming negligible the dependence on the chosen selection, the three distributions can be

taken as background models in the fitting procedure, independently from the data selection. The results of the fits are shown in the three plots of Figure 5.4, for the three  $b\bar{b}$  models obtained under the conditions presented above. The signal model corresponds to BV48, and the normalization is constrained to the 243 events found in the data sample.

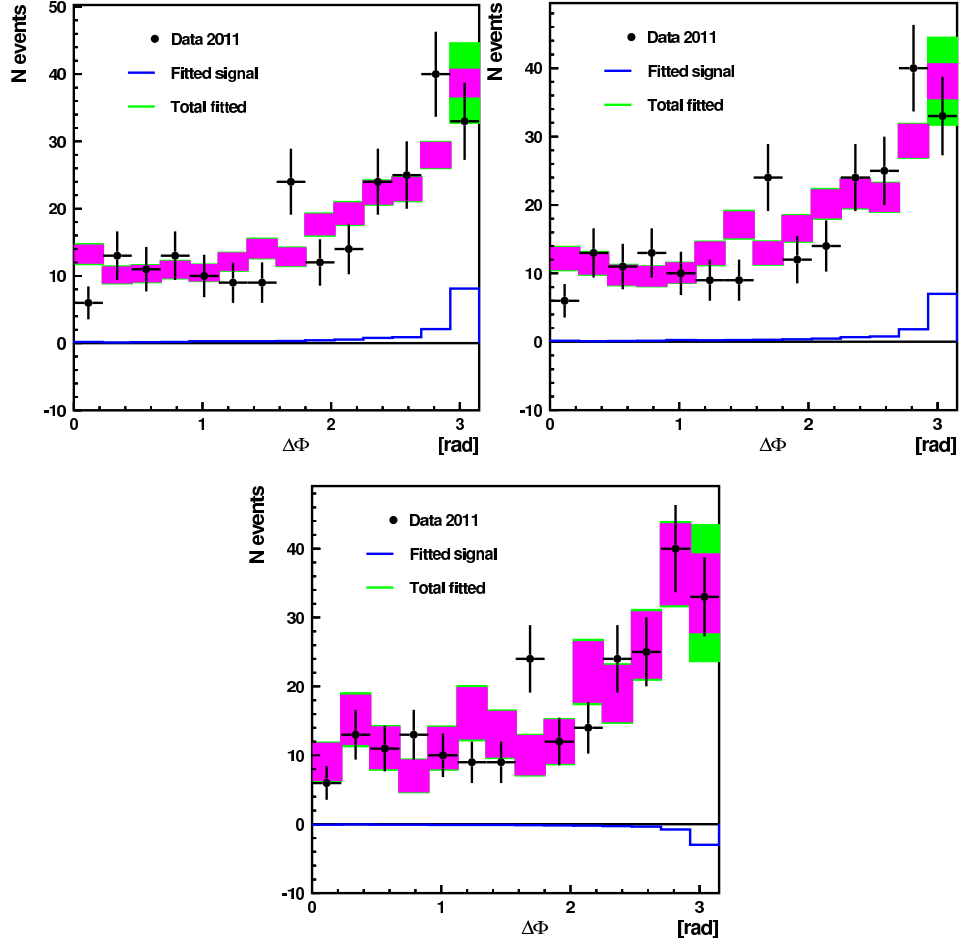


Figure 5.4: The  $\Delta\phi$  data distribution is fitted by a BV48 shape plus a background shape modeled from  $b\bar{b}$  MC events. The data points are shown in black, and the fitted signal component is the histogram in blue. The green and purple rectangles are the total fitted distribution. The purple is the statistical uncertainties propagated from the original  $b\bar{b}$  sample, the green portion is from the fit uncertainty. The three plots assume the background models corresponding to the  $b\bar{b}$  MC selections bb1, bb2, bb3, as described in the text.

The results are all compatible with zero BV48 signal event, as shown in Table 5.4. The BV48 detection efficiency is of  $83.2 \cdot 10^{-4}$  for BV48 events. From the result of the last line of Table 5.4, with a 21% total systematic uncertainty, the cross section times branching ratio 95 % CL upper limit is of 7.28 pb.

	data selection	$\bar{b}\bar{b}$ selection	$N_{data}$	$N_{signal}^{BV48}$	$\chi^2/DoF$
1	s4	bb1	243	14.6 (+13.1, -13.2)	2.2
2	s4	bb2	243	12.6 (+13.7, -13.9)	2.1
3	s4	bb3	243	-5.4 (+18.5, -20.1)	1.2

Table 5.4: Results of the fit of the  $\Delta\phi$  distribution of 243 data events with a signal component for BV48, and a background from  $\bar{b}\bar{b}$  MC events, selected by the three sets of cuts described in the text.

### 5.1.3 $1/\Sigma_R$ versus the di-LLP mass

This is an example of bi-dimensional analysis. The variables considered are the di-LLP invariant mass, and  $\Sigma_R$ , the sum of the  $\sigma_R$  of the two LLP. More precisely, the inverse  $1/\Sigma_R$  is used in the bi-parametric representation of Figure 5.5, left. This variable is also illustrated in Figure 5.6. The background is from  $\bar{b}\bar{b}$  MC events, and the signal sample is BV48.

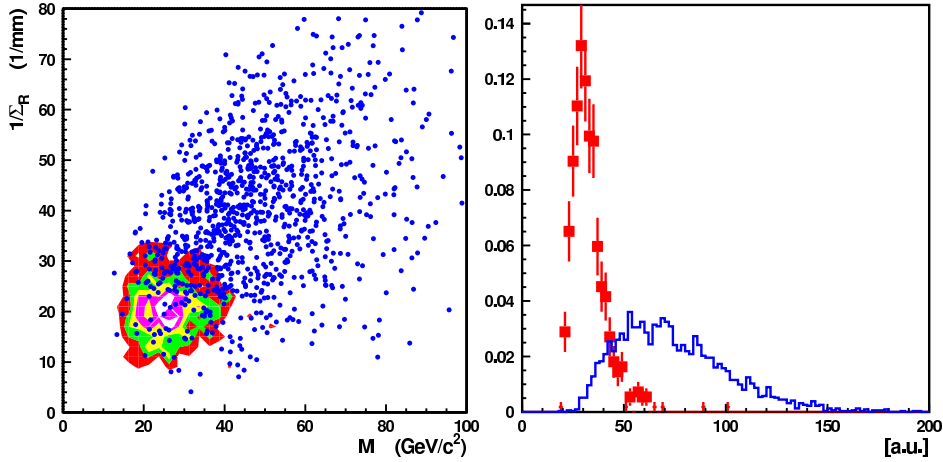


Figure 5.5: Left: background (contour) and BV48 signal (points) in the (di-LLP mass ,  $1/\Sigma_R$ ) plane. Right: normalized distribution of the variable which combines di-LLP mass and  $1/\Sigma_R$ . The red squares are from  $\bar{b}\bar{b}$  MC events, the histogram in blue from BV48.

A correlation is visible in the signal distribution, with a major axis with a slope of about 45 degrees in the plot. The position of the projection of each point on that major axis of the distribution provides a new variable which exploits the correlation. This combined variable has a better separation power than the original observables taken individually. This can be seen in Figure 5.5, right (to be compared with Figure 5.6).

The results of the fits with the analysis conditions of Table 5.5 are shown in Figure 5.7. Like it was the case for the fit of the di-LLP mass alone, when the background sample has been selected with different criteria as compared to the data and signal, the position of the  $\bar{b}\bar{b}$  distribution is left free to float. A shift of 2.5 units toward the right provides the best  $\chi^2$  when

## 5.1. Fitting of key variables distributions

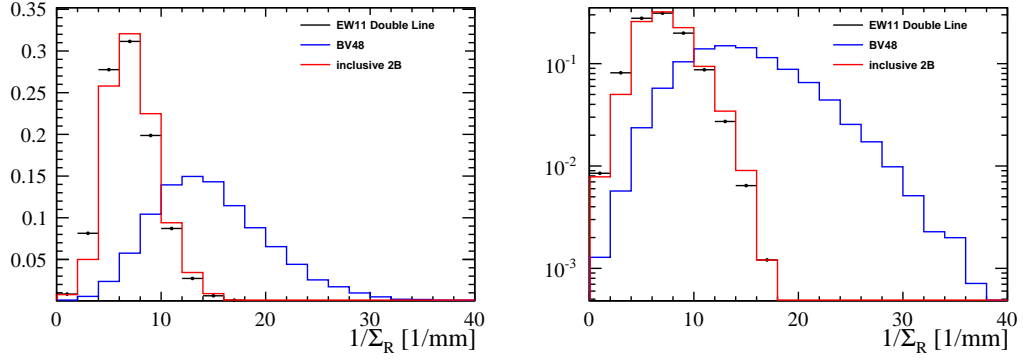


Figure 5.6:  $1/\Sigma_R$  distribution in the s1 scenario. The distribution on the right-hand side is given in logarithmic scale. Distributions have been normalized to one.

	data selection	$b\bar{b}$ selection	$N_{data}$	$N_{signal}$ BV48	$\chi^2/DoF$
1	s2	bb2	51243	195 (+491 -502)	0.92
2	s3	bb3	15176	1282 (+545 -588)	0.84
3	s4	bb3	88	11 (+9 -9)	0.95

Table 5.5: Results of the fit of the variable which combines di-LLP mass and  $1/\Sigma_R$ . For the fit 3, the  $b\bar{b}$  background was shifted by 2 channels, to compensate for the difference in the selection criteria.

bb3 is used to fit s4 selected data. The detection efficiency is of  $63.2 \cdot 10^{-4}$  for BV48 events. From the result of the last line of Table 5.5, with a 21% total systematic uncertainty, the cross section times branching ratio 95 % CL upper limit is of 8.8 pb.

## Chapter 5. Extractions of the Signal Yield from the 2011 Selected Events

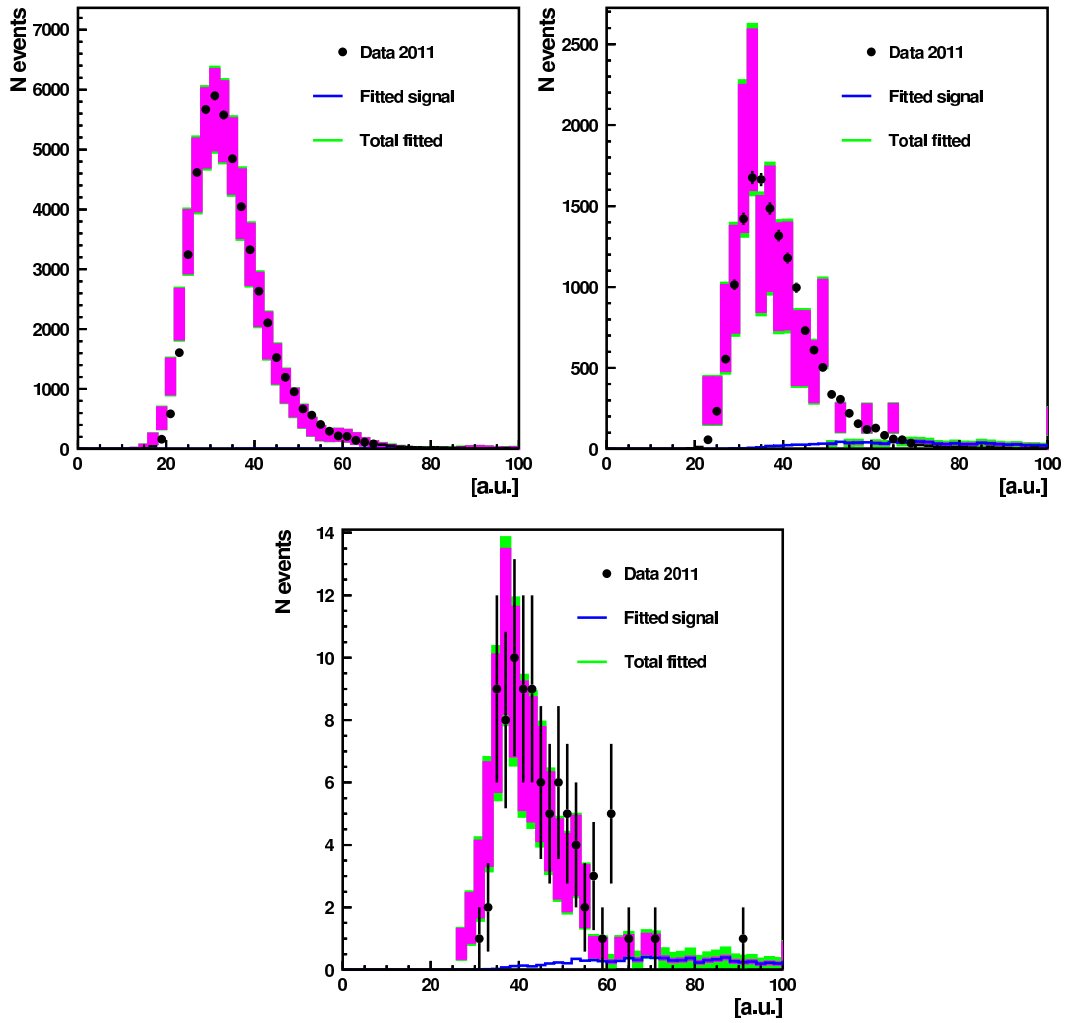


Figure 5.7: Fit of the of the variable which combines di-LLP mass and  $1/\Sigma_R$ , for the three data events and  $b\bar{b}$  events selections as given in Table 5.5. The signal component is from BV48.

## 5.1.4 Analytical PDF fit of the mass of the di-LLP

The goal of this section is to fit the di-LLP candidate mass using two analytical PDFs determined from the histograms of the signal models and of the background sample. First, the di-LLP mass of the BV48 models is fitted with two phenomenological analytical functions, a decay function and a resolution function, see Figure 5.8. The fits are obtained with the set of cuts  $s_3$  and asking for a positive decision of the HLT2 double trigger line.

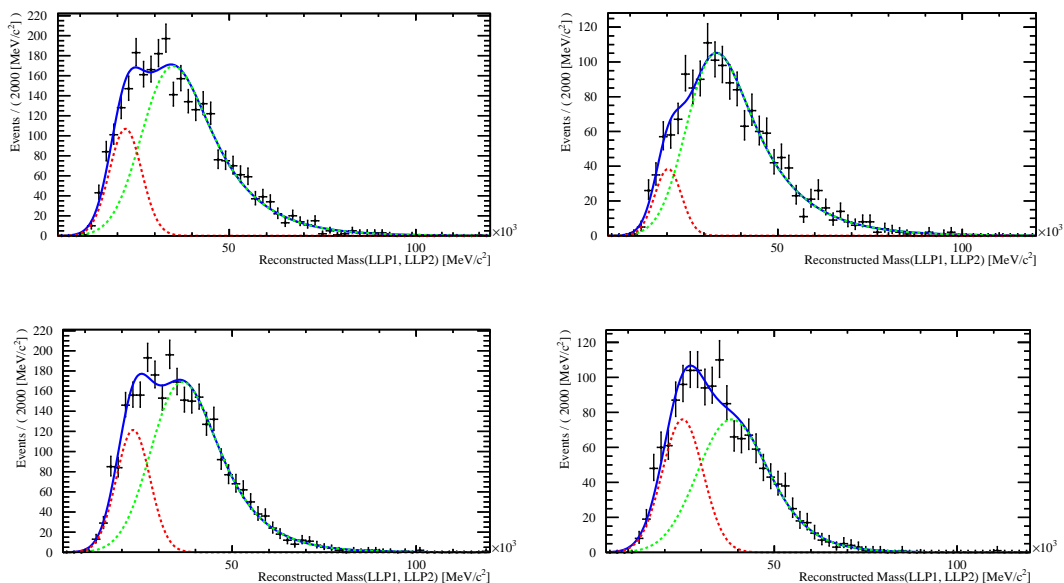


Figure 5.8: Fit of the di-LLP mass for different BV48 model. Top right: BV48 10ps, top left: BV48 5ps, bottom right: BV48 15ps, bottom left: BV48 50ps.

Because the parameters of these different fits are very close (within 5% variation), the signal pdf is reconstructed by adding the BV48 signal samples with 5, 10, 15, 50 ps neutralino lifetimes to benefit from a larger statistics. The signal pdf is presented in Figure 5.9 and the fit parameters are given in Table 5.6.

$\mu_1$	$29502 \pm 551$
$\sigma_1$	$6968 \pm 287$
$\mu_2$	$22688 \pm 459$
$\sigma_2$	$4548 \pm 237$
$\tau_{\text{sum}}$	$10362 \pm 277$
$u$	$0.78 \pm 0.02$

Table 5.6: Fit parameters determined from the addition of BV48 models with  $\chi$  lifetimes of 5, 10, 15 and 50 ps.  $\mu_1$  and  $\mu_2$  are the means of the two gaussian functions,  $\sigma_1$  and  $\sigma_2$  are their respective width,  $\tau_{\text{sum}}$  is the decay function slope and, finally,  $u$  is the fraction between the red and green curves drawn in Figure 5.9

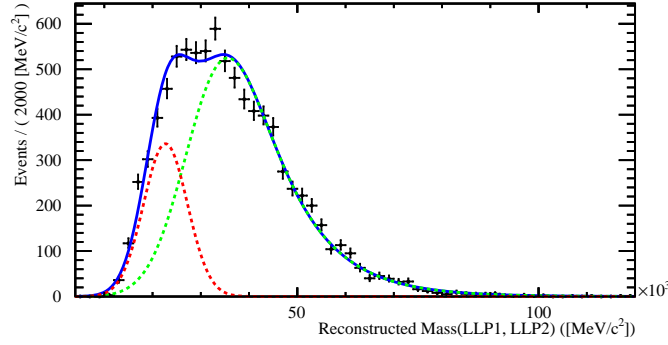


Figure 5.9: Signal PDF from the addition of BV48 models with 5ps, 10ps, 15ps and 50ps neutralino lifetimes.

In order to get a satisfactory model of the background, it is not possible to use the set of MC  $b\bar{b}$  events because the number of event is again too small, especially in the queue of the distribution, where it is important to have a sufficient statistics for the fit to work efficiently. To cope with that, the data with selection cuts s2 are used. Indeed, it is reasonable to assume that the fraction of signal events is negligible at this stage. Going from s2 to s4, the number of  $b\bar{b}$  drops of about a factor 1000 while the efficiency for signal events is reduced by roughly 20%. The obtained fit is given in Figure 5.10 and its parameters are given in Table 5.7.

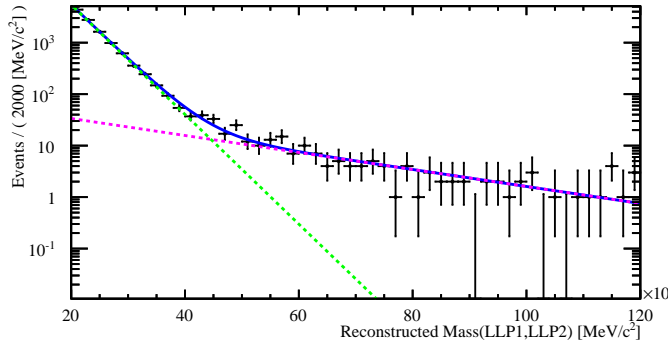


Figure 5.10: Fit of the data in the s2 scenario, used for background modeling. Two exponential functions are used.

$f$	$0.037 \pm 0.005$
$\tau$	$-3.80 \cdot 10^{-5} \pm 4 \cdot 10^{-6}$
$\tau_2$	$-2.453 \cdot 10^{-4} \pm 3 \cdot 10^{-6}$

Table 5.7: Fit parameters determined for the data in the scenario s2. Two exponential functions are used,  $\tau$  and  $\tau_2$  being their respective slopes.  $f$  is the fraction between the two functions.

The background PDF is obtained by the combination of two exponential functions, which is



coherent when fitting the MC  $b\bar{b}$  sample as illustrated on the Figure 5.11.

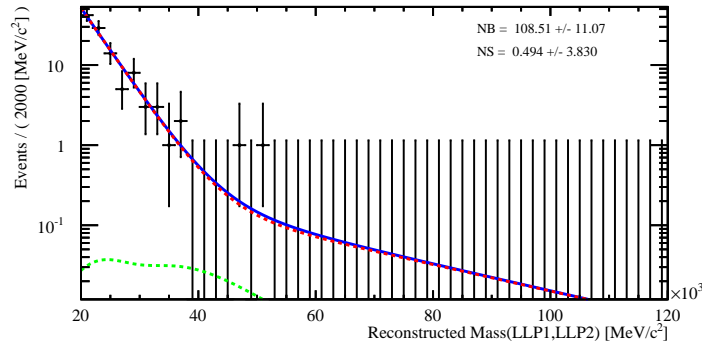


Figure 5.11: Fit of the MC  $b\bar{b}$  sample with the scenario bb1. Two exponentials are used and a signal component has been added to test the coherence of the method. NB and NS are respectively the number of background and signal events determined by the fit.

Then, data events selected by the final selection (s4) from  $20 \text{ GeV}/c^2$  to  $120 \text{ GeV}/c^2$  are fitted by combining the signal and background distributions aforementioned, keeping their respective parameters fixed to the values obtained from their respective data sets. The results of the fit are presented in Figure 5.12.

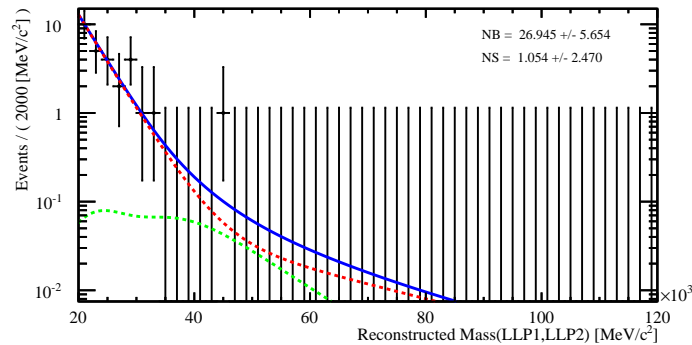


Figure 5.12: Result of the fit of the data after s4 selection using the distributions obtained in Figure 5.9 and 5.10. NB and NS are respectively the number of background and signal events determined by the fit.

Again, the signal component is compatible with zero. It has to be noticed that the given errors are rough estimations. To improve their calculations, variations of the fixed parameters in between their relative error must be done keeping trace of the correlation between the parameters. An alternative way of doing so is presented in the next section and consists in simultaneously fitting the three distributions.

5.1.5 Simultaneous fit of the mass of the di-LLP

The simultaneous fit of signal models, background models and data using the same set of functions as in 5.1.4 allows to infer the total uncertainty. Here, only one signal sample is considered at the time. The fits are made using the unbinned extended likelihood method (see [24]).

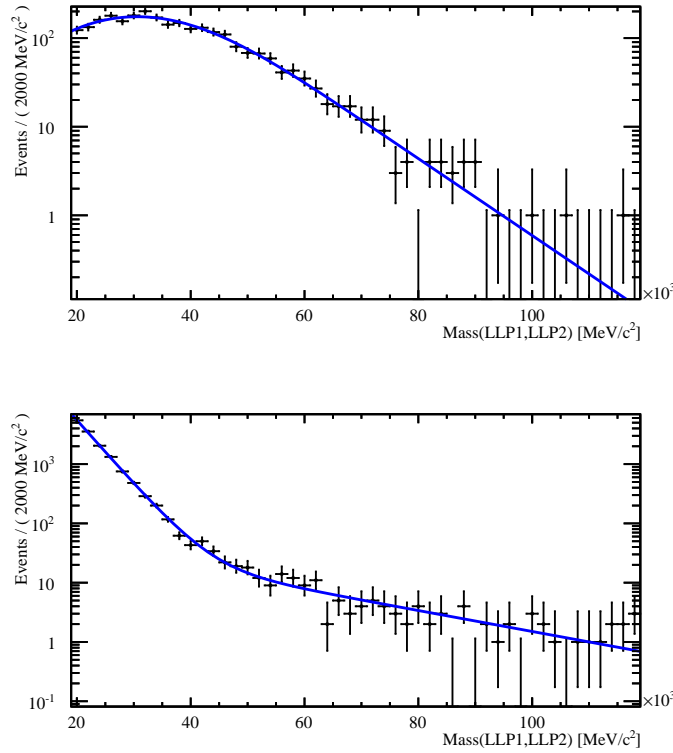


Figure 5.13: Fit of the BV48 MC signal model di-LLP mass (up) and of the data (down) with the selection s2 used as background model.

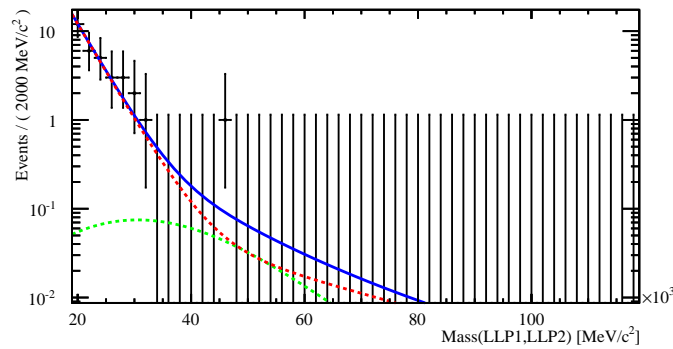


Figure 5.14: Fit of the di-LLP mass for the data in the scenario s4. This is obtained simultaneously with the fits of Figure 5.13.

## 5.1. Fitting of key variables distributions

Table 5.8 gives the detailed lists of fit parameters obtained for the BV48 10ps signal model.

<i>mu1</i>	$23167.35 \pm 702.2$
<i>sigma1</i>	$11893.48 \pm 922.2$
<i>taum</i>	$10006.45 \pm 638.4$
$N_{BV}$	$2613.0 \pm 51.1$
<i>f</i>	$0.034 \pm 0.0044$
<i>rtau</i>	$6.13 \pm 0.63$
<i>tau</i>	$-4.07 \cdot 10^{-5} \pm 4.4 \cdot 10^{-6}$
$N_{Back}$	$14609.0 \pm 120.1$
$N_B$	$31.88 \pm 6.01$
$N_S$	$1.12 \pm 2.34$

Table 5.8: Fit parameters determined by the simultaneous fit of the BV48 signal sample in scenario s3, the background model from data s2 and the data s4. *mu1* and *sigma1* are the mean and width of the signal PDF, *taum* being the slope of its decay function. *tau* is the slope of the first background exponential and *rtau* is the ratio between it and the second exponential slope. *f* is the ratio between the two background exponentials.  $N_{BV}$  is the number of events in the fit of the signal component and  $N_{Back}$  is the computed number of events in the background fit.  $N_S$  and  $N_B$  are respectively the extracted number of signal and background events found in the data s4.

Model	$N_B$	$N_S$
BV48	$31.88 \pm 6.01$	$1.12 \pm 2.34$
BV48 5 ps	$31.97 \pm 5.99$	$1.04 \pm 2.23$
BV48 15 ps	$31.81 \pm 6.02$	$1.19 \pm 2.37$
BV48 50 ps	$31.68 \pm 6.04$	$1.32 \pm 2.49$
BV35	$31.84 \pm 6.02$	$1.16 \pm 2.37$
BV20	$31.90 \pm 5.97$	$1.10 \pm 2.21$
BV48 10 ps $m(h^0)=100$ GeV	$31.74 \pm 6.07$	$1.26 \pm 2.52$
BV48 10 ps $m(h^0)=125$ GeV	$32.08 \pm 5.94$	$0.92 \pm 2.04$

Table 5.9: Results of the simultaneous fits for different BV MC models.  $N_S$  and  $N_B$  are respectively the extracted number of signal and background events found in the data s4.

Table 5.9 gives the results of the simultaneous fits for various BV models with  $1\sigma$  errors. All results are compatible with 0 observed signal event.

Upper limits on production cross sections at 95% CL, assuming 21% total systematic uncertainties, are given along with total efficiencies for the set of MC BV samples in Table 5.10.

In order to test this method, a toy experiment study has been made. 2000 experiments are generated in which 1, 3, 5 and 10 signal events are randomly drawn from the BV48 PDF while the rest of the 33 events are randomly drawn from the background PDF. Then, simultaneous

## Chapter 5. Extractions of the Signal Yield from the 2011 Selected Events

Model	$\epsilon$ [%]	$\sigma_{max}$ [pb]
BV48	0.606	1.83
BV48 5 ps	0.339	3.11
BV48 15 ps	0.635	1.79
BV48 50 ps	0.296	4.08
BV35	0.337	3.35
BV20	0.023	45.98
BV48 10 ps $m(h^0)=100$ GeV	0.348	3.47
BV48 10 ps $m(h^0)=125$ GeV	0.391	2.45

Table 5.10: Total selection efficiency (in [%]) for different BV MC models, with s4 selections and for a di-LLP mass between 20 and 120 GeV/ $c^2$  and upper limits on production cross sections at 95 % CL from the results of the simultaneous fits.

fits are performed for each of those experiments. The number of extracted signal events is compared to the generated one. Results of this procedure are illustrated on Figure 5.15 and pull distributions<sup>1</sup> have been calculated and are illustrated in Figure 5.16.

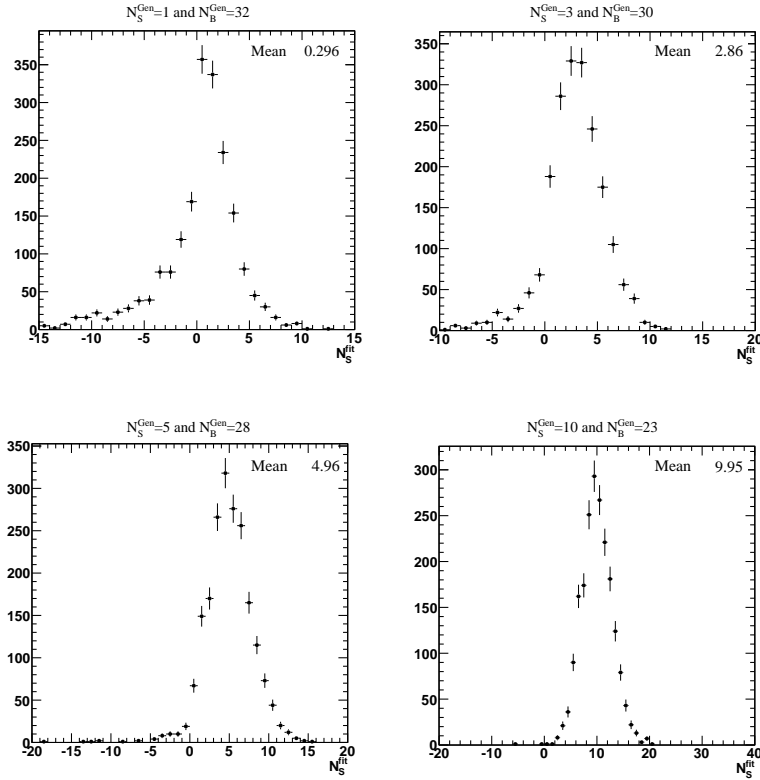


Figure 5.15: Number of signal events extracted from 2000 toy experiments with fixed  $N_S^{Gen}$  signal and  $N_B^{Gen}$  background events.

<sup>1</sup> $(N_S^{fit} - N_S^{Gen})/\text{error on } N_S^{fit}$

## 5.1. Fitting of key variables distributions

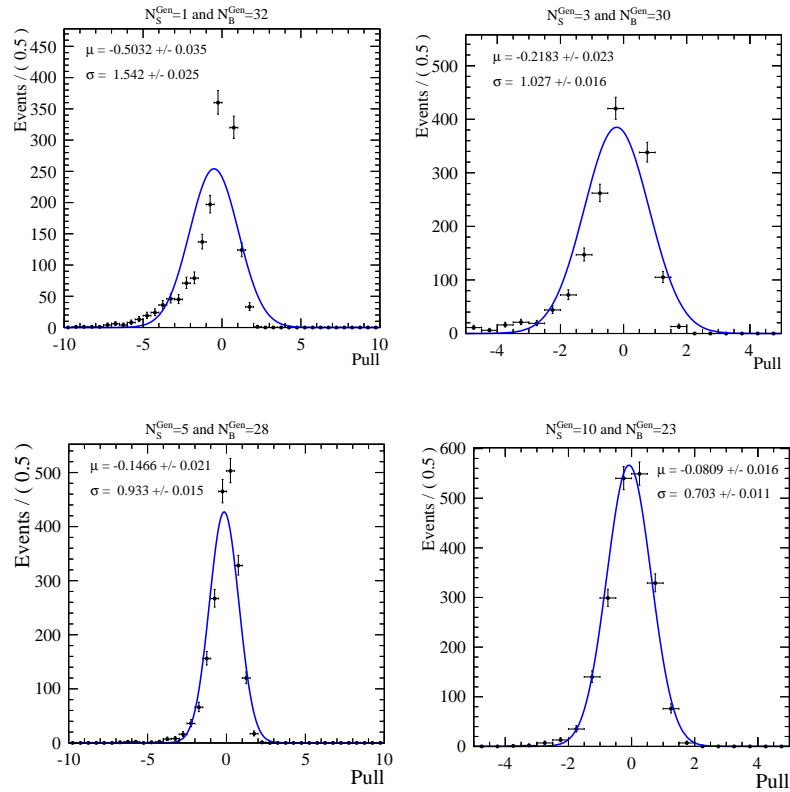


Figure 5.16: Gaussian fits of the pull distributions obtained from the simultaneous fits of 2000 toy experiments with  $N_S^{Gen}$  number of signal events and  $N_B^{Gen}$  number of background events.

These results demonstrate that it is possible to recover the correct amount of signal events, with a bias smaller than 1% for  $N_S$  greater or equal to 5 . In addition, the same toy experiment procedure as been made, but this time adding to the s4 data sample a fixed number of signal events from the BV48 PDF. Again, the method guesses, in average, the correct number of signal events.

## 5.2 ABCD Method

Two variables,  $x, y$ , are chosen to define a bi-dimensional region  $(x, y)$  displaying a separation of the signal and background as large as possible. Two cuts,  $x_l$  and  $y_l$ , are selected to separate the data bi-dimensional distribution into four regions, named A, B, C, and D (see a toy experiment example in Figure 5.20), D being the region where the signal yield will be extracted. The four regions contain a number of events  $N_A, N_B, N_C, N_D$ , respectively. The goal of the ABCD method is to estimate the amount of background events in the region D. Assuming that the background events are uncorrelated in  $x$  and  $y$ , and that a negligible amount of signal falls in the regions A, B, and C, then the estimate of background in D,  $\bar{B}_D$ , (the bar indicates that the number is an estimate) is given by:

$$\bar{B}_D = N_B N_C / N_A, \quad (5.1)$$

and the estimate of the amount of signal in D is then  $\bar{S}_D = N_D - \bar{B}_D$ .

In the case of the couple of variables (di-LLP mass,  $1/\Sigma_R$ ) seen above (in 5.1.3), the background region could be isolated quite efficiently. Unfortunately, the two variables are not uncorrelated. Therefore, a correction should be introduced to mitigate the systematic effect due to the correlation.

Two almost uncorrelated variables are the mass of one of the LLP and the number of tracks of the other LLP. The bi-parametric distributions for the BV48 signal and  $b\bar{b}$  MC events are compared in Figure 5.17. The events selection is s2 (see Table 5.1). Some level of correlation unavoidably subsists because of the  $p_T$  ordering of the two LLPs. This amount can be estimated by comparing the mass distributions for different number of tracks intervals, as shown for the  $b\bar{b}$  MC events and for 2011 data in Figure 5.18. The distributions coincide within statistical fluctuations, which demonstrates a low level of correlation.

On the other hand, for this couple of variables, the second criterion for the validity of the ABCD method is not well satisfied, as the BV48 signal penetrates the background region, and there is no possibility to isolate a background region totally signal free. When an hypothesis can be made on the amount of signal and its distribution, an average value can be subtracted from the counts in the A, B, and C regions, before the calculation of  $\bar{B}_D$ .

The choice of the cut positions for the two variables should be made in order to maximize the significance of the signal defined as  $S_D / \sqrt{S_D + \bar{B}_D}$ . The significance can be estimated by:

$$\text{significance} = S_D / \sqrt{S_D + \bar{B}_D^2 \left( \frac{1}{N_A} + \frac{1}{N_B} + \frac{1}{N_C} \right)} \quad (5.2)$$

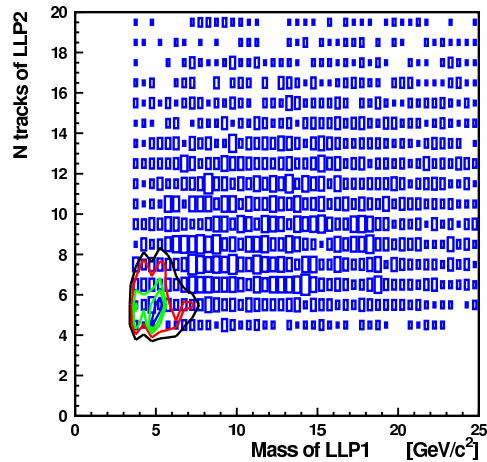


Figure 5.17: Bi-dimensional distribution of the signal BV48 (blue boxes) and  $b\bar{b}$  MC background (curves) in the (mass of LLP1, number of tracks in LLP2) plane.

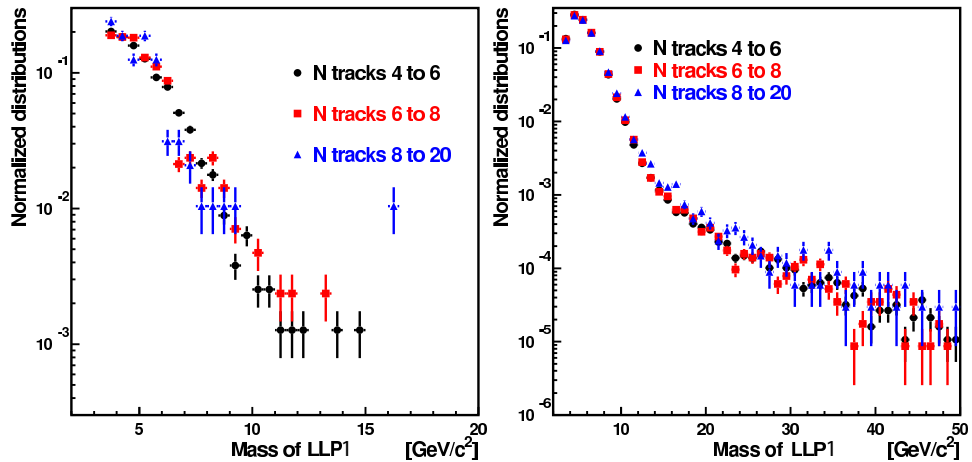


Figure 5.18: Distributions of the invariant mass of the LLP1 for different selections on the number of tracks in LLP2. Left: MC events, right is data. The distributions are normalized to one.

which indicates that the signal has to be maximized, and the background minimized as usual, and, in addition, the counting in A, B, and C should be roughly equal and maximized. The best choice of cuts depends on the signal hypothesis. The results of Figure 5.19 are given for 200 background events and assuming 5 BV48 signal events. A wide region with a maximum significance of 1.7 is found in correspondence of 7–8  $\text{GeV}/c^2$  for the mass, and 7–8 tracks. In general, for increasing signal hypothesis, the optimal cuts move toward harder values.

A toy MC method has been used to optimize the choice of cuts, and to determine the uncertainties on the number of signal events. A series of 1000 experiments are generated and analyzed as a function of the positions of the cuts which are varied over the background region. For illustration, the situation of a particular toy experiment is shown in Figure 5.20. Five signal

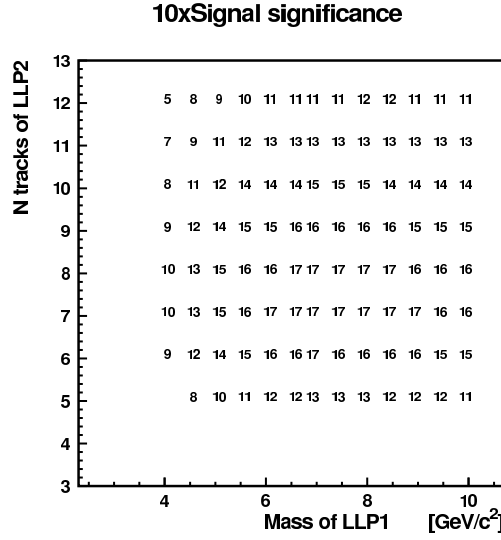


Figure 5.19: Computed significance values for 200 background events and 5 signal events, as a function of the cuts on the mass of LLP1 and number of tracks of LLP2. The values are multiplied by 10.

	A	B	C	D
background	164	7	27	2
signal	0	1	0	4
total	164	8	27	6

Table 5.11: Number of events in the four regions for the toy experiment of Figure 5.20.

events were generated based on the BV48 bi-parametric distribution, and the 200 background events, assuming the  $\bar{b}b$  MC bi-parametric distribution.

For the toy experiment of Figure 5.20, with a mass cut placed at  $7 \text{ GeV}/c^2$  and 8 tracks, four of the five signal events sit in region D, while one event is found in region B, and two background events are found in D. See Table 5.11.

If no correction is applied to take into account the possible contamination of A, B and C by the signal, the method estimates  $\bar{B}_D = 1.15$ , instead of 2, and  $\bar{S}_D = 4.85$  instead of 4.

As previously said, if the amount of signal is assumed known, a correction could be done by subtracting the average expected values. If the hypothesis of a total of 5 signal events is made, for BV48, the average is of 0.2, 0.4, 1.3, and 3.0 events in the four regions. After subtraction, the results for this experiment are  $\bar{B}_D = 1.19$  and  $\bar{S}_D = 4.81$ .

Over 1000 toy experiments an average  $\bar{S}_D = 4.1 \pm 2.0$  is found which is 1.1 larger than the true value of 3, see Table 5.12. The uncertainty is the r.m.s. of the deviations of the computed values with respect to the average obtained. A small reduction of the bias can be obtained by



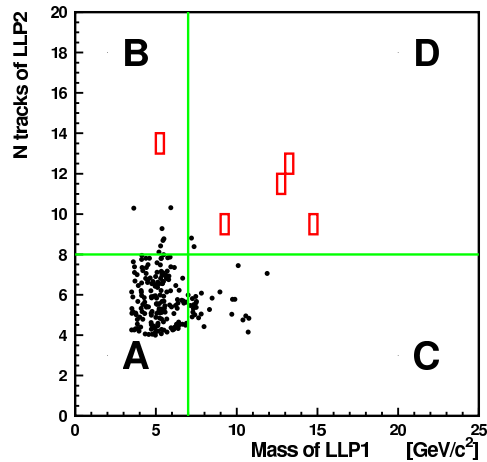


Figure 5.20: Situation of one toy experiment, with 200 background events (black points) and 5 BV48 events (red rectangles). 4 signal events lie in the D region, and one signal event falls in B.

	A	B	C	D
background	160.7	9.1	27.6	2.7
signal	0.2	0.4	1.3	3.0
total	160.9	9.5	28.9	5.7

Table 5.12: Number of events in the four regions, averaged over 1000 toy experiments.

the subtraction of the average signal from A, B, and C: the result is  $\bar{S}_D = 4.0$ . A large portion of the bias is due to the poor statistics of the background model used to generate the events, in particular in the regions B and C. Another contribution comes from some correlations of the two variables.

A first check of the method is performed by using as background model the two distributions for the mass and for the number of tracks (i.e. the projections of the bi-parametric distribution on the two axis). The statistical fluctuations are strongly reduced, and the correlation is lost. In this case the computed average signal is  $\bar{S}_D = 2.9 \pm 2.1$ , with a very small bias.

A second check is made by using the data itself as a high statistics background model. With loose cuts the signal level is certainly negligible, while keeping track of the correlations. Under the same conditions as before, the result is  $\bar{S}_D = 3.3 \pm 2.5$ , a bias of 0.3 events is found. Again using the data, but removing the correlations by using the two projections, the bias disappears. We should conclude that the correlation between the two variables is responsible for an underestimate of 0.3 events in the determination of the background.

Applied to the 172 events of the data sample s4 (cuts on the mass of LLP1, and number of tracks of LLP2 removed), with ABCD boundaries placed at (7, 8), the number of events in A, B, C, and D is 80, 47, 30, and 15 respectively. Without subtraction of signal, the extrapolation to the D region gives 17.6 events. As seen before, a bias of 0.3 events comes from the variable

## Chapter 5. Extractions of the Signal Yield from the 2011 Selected Events

correlation. This value is used for a correction, giving  $\bar{B}_D = 17.9$ , and added to systematics. In conclusion the result is  $\bar{S}_D = -2.9$ . The statistical uncertainties coming from the number of events on the regions A, B, C and D is 5.45 events. From toy MC, with 172 data events, we have an average statistical uncertainty of 6.5 events on the estimates. After adding the systematic contribution from the bias, the result is  $\bar{S}_D = -2.9 \pm 6.8$ . The results for all the signal models are given in Table 5.13.

Model	$\epsilon \times 10^4$	$\sigma_{max}$ [pb]
BV48	53.78	3.81
BV48 5ps	29.16	7.03
BV48 15ps	56.24	3.64
BV48 50ps	26.09	7.86
BV48 mH100	31.71	6.46
BV48 mH125	33.68	6.09
BV35	28.57	7.18
BV20	1.69	120.99
HV10	10.28	19.94

Table 5.13: Upper limits for cross section times branching fraction assuming various theoretical models.  $\epsilon$  is the total selection efficiency. Upper limits are computed at 95 % CL with 21% total systematic uncertainty.

An identical procedure is applied to the complementary couple of variables, the mass of the second LLP and the number of tracks of the first LLP. 261 events are found in the s4 data set with relaxed cuts on the two variables. In this case, the optimization suggests a boundary at 6 GeV/c<sup>2</sup> and 8 tracks, selecting 115, 60, 58, and 28 events in the four regions. Neglecting the contamination from signal events in the A, B, and C regions, the amount of signal in D is estimated at -2.2 events and then at -2.5 after correction for the bias. The toy MC provides the statistical error  $\pm 8.3$  events, and  $\pm 8.6$ , after adding the bias uncertainty. The results are given in Table 5.14 and are consistent with the previous results, but less stringent, due to a larger statistical error.

Model	$\epsilon \times 10^4$	$\sigma_{max}$ [pb]
BV48	56.08	5.02
BV48 5ps	30.60	9.20
BV48 15ps	58.21	4.84
BV48 50ps	28.00	10.06
BV48 mH100	33.00	8.53
BV48 mH125	36.03	7.82
BV35	30.78	9.15
BV20	2.14	131.73
HV10	12.15	23.18

Table 5.14: Same as in Table 5.13 for the complementary couple of variables.

### 5.3 The Neural Net method

The Neural Net (NN) classifier (for reference, see [25]) has been implemented based on the following 13 input variables:

- M1, M2: invariant mass of LLP1, LLP2
- NT1, NT2: number of tracks associated to LLP1, LLP2
- PT1, PT2: their  $p_T$
- R1, R2: their radial distance
- SigR1, SigR2: vertex fit radial uncertainty
- SigZ1, SigZ2: vertex fit longitudinal uncertainty
- Dphi:  $|\Delta\phi|$

Note that the di-LLP invariant mass is not used in the NN, to keep it as a control variable. The distributions of the 13 variables after the s2 selection are shown in Figure 5.21. The variables are used in the NN after a normalization procedure to bring them close to an average value of zero, and to get a width distribution of the order of one, giving the results of Figure 5.22.

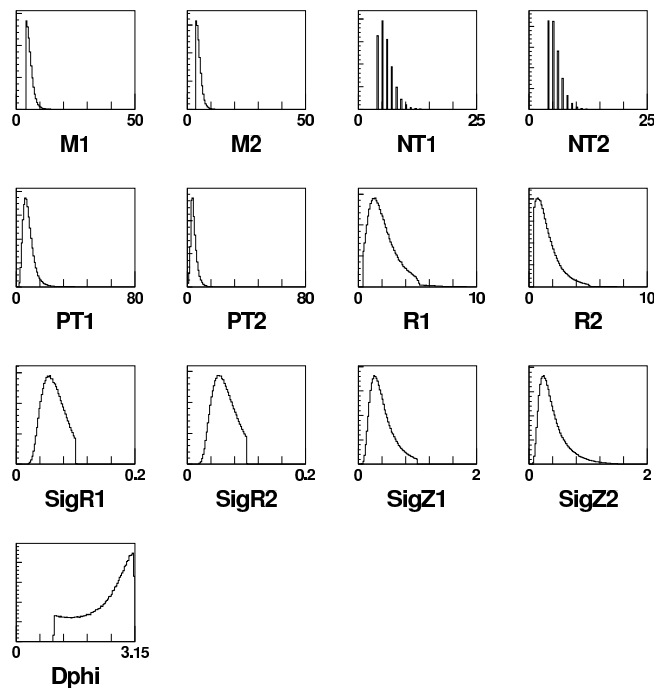


Figure 5.21: Input variables of the NN event classifier.

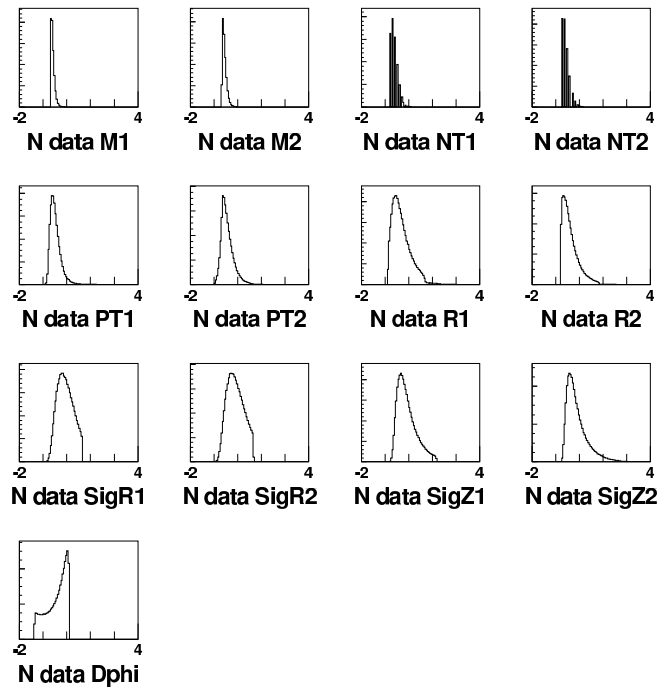


Figure 5.22: Input variables of the NN classifier after normalization.

The recurrent problem is the absence of a model for the background. To cope with that, considering that the amount of signal is small in the data, the technique adopted is to use a portion of the data itself to play the role of background set. This is illustrated in the following example in which the set s1 with a very large amount of data is used. Given that the signal set (BV48) has a about 5 thousand events, the same number is chosen in the data and used as background sample. The average NN error evolution during the training is given in Figure 5.23. Overtraining happens after  $\sim 150$  cycles. The chosen value for this configuration is then 130. The NN answers after training are shown in Figures 5.24, and 5.25. The NN response to the BV48 test set, to the data (the few thousand events used for the training were removed), and also the results for the  $b\bar{b}$  events of the bb1 set are found in the figure. The figure also presents the results for the  $b\bar{b}$  events of the bb1 set showing that they reproduce the data. Figure 5.25 on the left-hand side shows the fraction of events selected by a given NNcut.

In order to estimate the bias introduced by the presence of some signal in the data set used as a background sample, the training is redone with 5% of signal events added to the background sample. The results are compared to the previous one in Figure 5.25 right, demonstrating that the bias is in general small, even for a relatively large "contamination".

The effect of a tight selection  $NN > 0.95$  on the mass and number of tracks of the LLP1, and on the di-LLP mass, is shown in Figure 5.26, for BV48 events. As one can expect, the NN is selecting higher mass candidates.

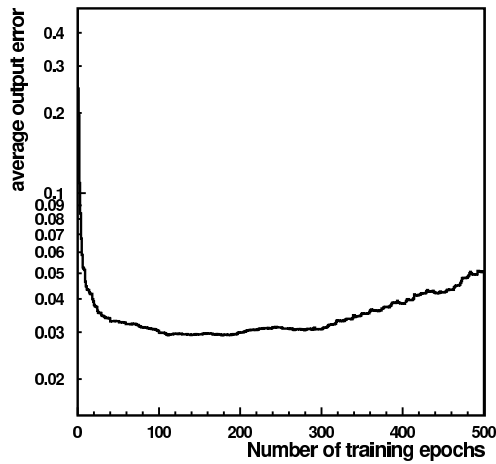
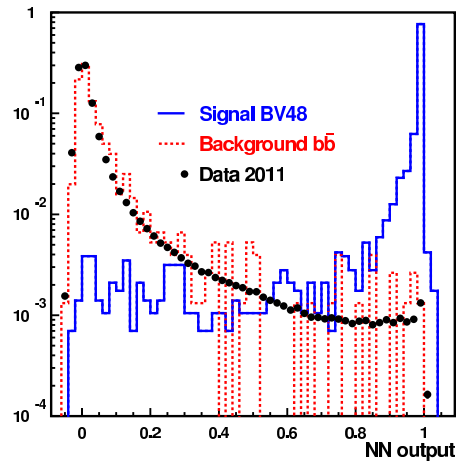


Figure 5.23: Average error evolution during the NN training.

Figure 5.24: NN answer to the BV48 test sample (blue histogram), to the  $b\bar{b}$  sample (red dashed) and to the data 2011 (dots) distributions. The distributions are normalized to unity.

The analysis using conditions s3 must be slightly changed as only 4908 are found in the data. This set is split in two parts, the NN is first trained on the first set and the second half analyzed, then the roles are exchanged, in such a way that the full statistics is preserved. After training, a cut  $NN > 0.85$  selects  $(92.2 \pm 0.5)\%$  of the BV48 events, while the s3 data sample is reduced to 35 events.

### 5.3.1 Di-LLP mass after NN selection

The di-LLP mass plot is fitted to estimate the number of events. In the case of s3, in order to have a background model, the bb2 sample is considered with a NN cut which lives 200 events. The corresponding histogram is fitted by a double exponential, only on its right slope, i. e. for a di-LLP mass larger than  $20 \text{ GeV}/c^2$ . The result is shown in Figure 5.27, left. The parameters

## Chapter 5. Extractions of the Signal Yield from the 2011 Selected Events

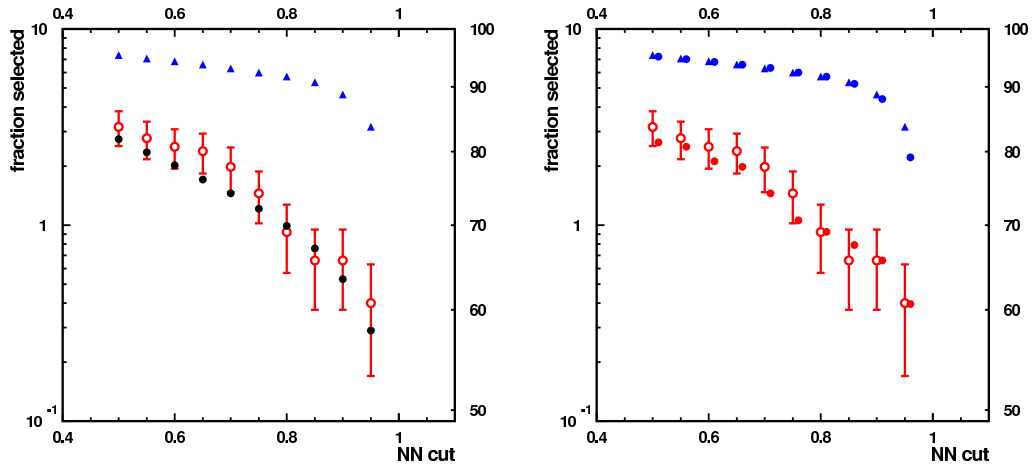


Figure 5.25: Fraction of events selected above a given cut on the NN variable. The left plot shows the BV48 selection efficiencies indicated with blue triangles (use the right scale); the red open circles are the  $b\bar{b}$  MC events, and the black points correspond to the data (use the left scale). On the right figure, the results for BV48 and  $b\bar{b}$  as before, and also obtained with a NN trained with a background polluted by 4% signal events (dots slightly displaced on the right) are shown.

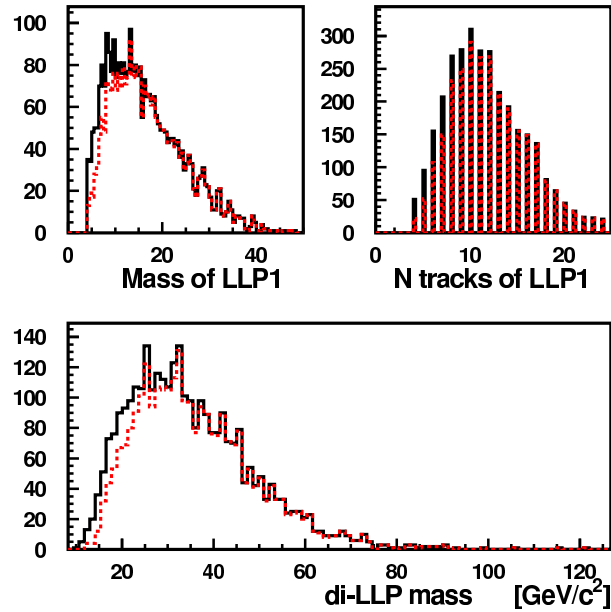


Figure 5.26: Mass and number of tracks of the LLP1 and di-LLP mass for BV48 events, after pre-selection (in black) and after a  $NN > 0.95$  cut (red dashed).

of the two exponentials are then kept fixed and used in the fit of the 35 data events, in which the amounts of BV48 signal and of the parametrized background are left free. The fit suggests a signal contribution of  $0.8 \pm 7.7$  events, with  $\chi^2/\text{NDoF} = 1.1$ .

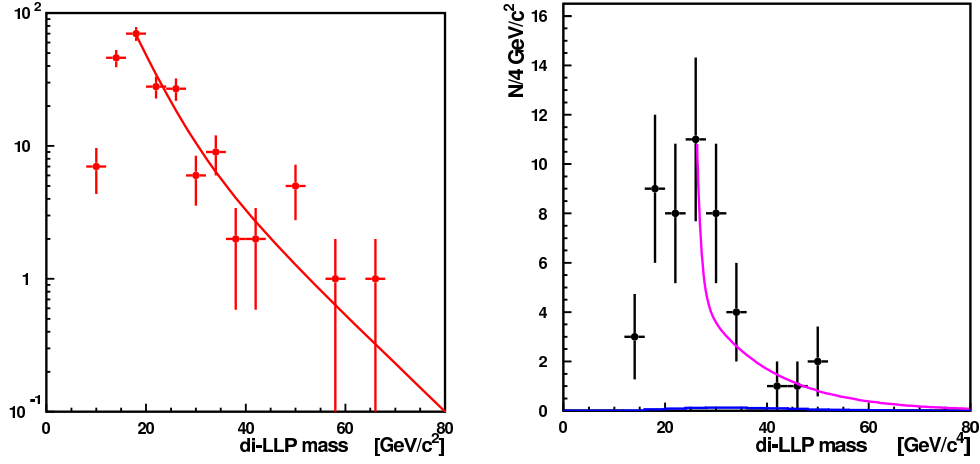


Figure 5.27: Left:  $\bar{b}b$  MC di-LLP mass is fitted by a double exponential. Right: the fit of the NN selected di-LLP candidates (dots with error bars). The result of the fit is shown by the purple curve, and the fitted signal by the 0.8 events contained in the blue histogram.

### 5.3.2 NN applied to other signal models

A similar procedure as the one illustrated in the previous section has been applied to the available full simulated MC samples. The pre-selection  $s_3$  gives the statistics summarized in Table 5.15. After training the selection by  $NN > 0.85$ , the fit provides the estimates of the number of signal events as shown in Table 5.16.

Model	$\epsilon_{gen}$	$N_{gen}$	$N_{s3}$	$\epsilon_{s3}$	$\epsilon_{MC}$
BV48	$28.44 \pm 0.24$	64.2k	2619	$4.08 \pm 0.08$	$1.16 \pm 0.03$
BV48 5ps	$28.44 \pm 0.24$	63.3k	1445	$2.28 \pm 0.06$	$0.65 \pm 0.02$
BV48 15ps	$28.44 \pm 0.24$	62.1k	2597	$4.18 \pm 0.08$	$1.19 \pm 0.03$
BV48 50ps	$28.44 \pm 0.24$	64.0k	1299	$2.03 \pm 0.06$	$0.58 \pm 0.02$
BV48 10 ps $m(h^0)=100$ GeV	$33.41 \pm 0.27$	64.8k	1610	$2.45 \pm 0.06$	$0.83 \pm 0.03$
BV48 10 ps $m(h^0)=125$ GeV	$26.52 \pm 0.23$	300.2k	8271	$2.76 \pm 0.03$	$0.73 \pm 0.01$
BV35 10ps	$26.81 \pm 0.23$	65.4k	1890	$2.89 \pm 0.06$	$0.77 \pm 0.02$
BV20 10ps	$26.38 \pm 0.23$	65.4k	289	$0.44 \pm 0.02$	$0.12 \pm 0.01$
HV10	100.	64.2k	396	$0.62 \pm 0.03$	$0.62 \pm 0.03$
Data 2011			4908		

Table 5.15: Number of events used in the different samples,  $N_{gen}$ , and selected by  $s_3$ ,  $N_{s3}$ .  $\epsilon_{gen}$  is the generator efficiency for the MC samples in %.  $\epsilon_{s3}$  is the fraction  $N_{s3}/N_{gen}$ , also in %. Finally,  $\epsilon_{MC} = \epsilon_{gen} \times \epsilon_{s3}$ .

## Chapter 5. Extractions of the Signal Yield from the 2011 Selected Events

Model	$\epsilon_s^{NN}$	$\epsilon_d^{NN}$	$N_s$	$\chi^2/\text{NDoF}$
BV48	$93.6 \pm 0.4$	$0.95 \pm 0.17$	$0.8 \pm 7.7$	1.1
BV48 5ps	$94.5 \pm 0.6$	$0.95 \pm 0.18$	$-5.6 \pm 7.8$	1.3
BV48 15ps	$93.6 \pm 0.4$	$0.79 \pm 0.17$	$8.7 \pm 10.3$	3.3
BV48 50ps	$95.8 \pm 0.6$	$0.75 \pm 0.17$	$10.0 \pm 8.7$	0.7
BV48 10 ps $m(h^0)=100$ GeV	$93.1 \pm 0.6$	$1.03 \pm 0.21$	$0.5 \pm 7.9$	1.3
BV48 10 ps $m(h^0)=125$ GeV	$93.6 \pm 0.3$	$0.86 \pm 0.21$	$6.6 \pm 7.3$	1.1
BV35	$89.6 \pm 0.7$	$1.06 \pm 0.20$	$2.0 \pm 7.9$	1.9
BV20	$83.0 \pm 2.2$	$3.35 \pm 0.36$	$22 \pm 14$	4.5
HV10	$74.4 \pm 2.2$	$1.90 \pm 0.28$	$12 \pm 11$	3.4

Table 5.16: Fraction (in %) of MC signal and 2011 data events selected by a  $NN > 0.85$  cut.  $N_s$  is the number of signal events from the fit of the di-LLP invariant mass distribution. The last column is the corresponding  $\chi^2/\text{NDoF}$ . The MC and data sets are pre-selected under s3 conditions.

### 5.3.3 Production cross section upper limits

From number of signal events determined by the di-LLP mass fit, the  $\sigma \times \mathcal{B}$  cross section times branching ratio upper limits, 95% CL, are computed as indicated in Table 5.17.  $\int \text{Ldt} = 0.9 \text{ fb}^{-1}$  and a total systematic uncertainty of 21% is assumed.

Model	$\epsilon \times 10^4$	$N_s$	$\sigma_{max}$ [pb]
BV48	108.57	$0.8 \pm 7.7$	2.86
BV48 5ps	61.43	$-5.6 \pm 7.8$	3.12
BV48 15ps	111.38	$8.7 \pm 10.3$	4.93
BV48 50ps	60.54	$10.0 \pm 8.7$	8.67
BV48 10ps $m(h^0)=100$ GeV	77.27	$0.5 \pm 7.9$	4.04
BV48 10ps $m(h^0)=125$ GeV	68.33	$6.6 \pm 7.3$	5.94
BV35	68.99	$2.0 \pm 7.9$	4.94
BV20	9.96	$22.0 \pm 14.0$	96.17
HV10	46.13	$12.0 \pm 11.0$	14.12

Table 5.17: Upper limits for cross section times branching fraction assuming various theoretical models.  $\epsilon$  is the total selection efficiency,  $N_s$  the number of signal events from the di-LLP mass fit. A 21% total systematic uncertainty is assumed.



## 5.4 Summary of the 2011 results

Different methods have been presented throughout this chapter. Upper limits on the production cross sections of Higgs-like bosons decaying into a pair of LLPs have been computed and are summarized in Table 5.18.

Model	$\sigma_{max}^{fit}$ [pb]	$\sigma_{max}^{ABCD}$ [pb]	$\sigma_{max}^{NN}$ [pb]
BV48	1.83	3.81	2.86
BV48 5ps	3.11	7.03	3.12
BV48 15ps	1.79	3.64	4.93
BV48 50ps	4.08	7.86	8.67
BV48 10ps $m(h^0)=100$ GeV	3.47	6.46	4.04
BV48 10ps $m(h^0)=125$ GeV	2.45	6.09	5.94
BV35	3.35	7.18	4.94
BV20	45.98	120.99	96.17
HV10	-	19.94	14.12

Table 5.18: Upper limits for cross section times branching fraction assuming various theoretical models.  $\sigma_{max}^{fit}$  is the upper limit from the simultaneous fit,  $\sigma_{max}^{ABCD}$  from the ABCD method and  $\sigma_{max}^{NN}$  from the neural network, computed at 95% CL.

The fitting procedure with MC inspired PDFs is affected by the lack of statistics for the background model. The ABCD method, in principle, can avoid this problem. On the other hand, this method is quite complex to handle, because of potential correlations between the chosen variables and because of signal contamination in the A, B and C regions. A Neural Network filtering procedure has also been tested providing a clear distinction between signal and background. Nevertheless, the extraction of physical results still requires the fit of the di-LLP mass spectrum.



## 6 Conclusion

During the last few years, a lot of exciting results have been published thanks to the thousand of people working in the CERN community. A turning point has been reached with the discovery of the Higgs boson, announced on the 4th of July 2012 and confirmed on the 15th of March 2013. Nevertheless, as discussed on Chapter 2, various problems still cry out for solutions. With exclusion limits being more and more stringent for "traditional" simple extensions of the SM, for example Supersymmetry with R-parity conservation and its simplest minimal declination, attention has been attracted by models with long-lived particles as discussed in this work. The LHCb experiment has an important role to play in the quest for long-lived exotic particles, its strength residing in the vertex detector and the trigger system that ultimately compensate for limited angular coverage and integrated luminosity. These features allow to be complementary to general purpose detectors.

In Chapter 4, the analysis of the  $0.9 \text{ fb}^{-1}$  of data collected at 7 TeV by LHCb in 2011 has been exposed. The selection of events with LLPs is intended to be as inclusive as possible in terms of lifetimes and masses. Various SUSY and Hidden Valley models have been chosen as guiding points in the very large phase space of theoretical scenario. Total selection efficiencies have been determined at the level of 0.02 to 0.7 % for  $h^0$  masses from 100 to 125  $\text{GeV}/c^2$ , LLP masses from 20 to 48  $\text{GeV}/c^2$  and lifetimes from 5 to 50 ps. The main source of background has been identified to be  $b\bar{b}$  events.

Different methods for background and signal yield estimations have been presented in Chapter 5. Different fitting procedures have been presented for key variables distributions. An "ABCD" method has been implemented to extract the signal yield in a phase space region chosen to maximize the signal significance. An event classifier based on a neural network algorithm has also been developed. These methods have allowed to set upper limits on production cross sections at the level of 1 to 100 pb for various signal models.

In conclusion, it must be noted that the obtained results are complementary to those given

## Chapter 6. Conclusion

---

by ATLAS and CMS and that LHCb has proven to be an important actor in the search for new physics. Pushing further those limits with the 2012 data set, and maybe discovering long-lived particles after the shutdown that will lead the LHC towards collisions at a center of mass energy of 13 TeV is totally in the reach of the LHCb experiment. New physics is potentially hiding just behind the corner.

# A Appendix

## A.1 HLT2 Double line discussion

As illustrated in Chapter 4 section 4.4.1, the behavior of the Hlt2DisplVerticesDouble trigger line is not well understood. It seems that the stripping double selection is looser than the HLT2 cuts and it is quite impossible to reproduce the effect of the online cuts in the offline (stripping) context. The cuts in mass are higher in HLT2 as shown by Table 4.5, but implementing them offline gives inconsistent results. On one hand, HLT2 has a  $\sim 55\%$  acceptance to BV48 reconstructible events. Stripping without HLT2 is nearly 100% efficient. On the other hand the stripped  $b\bar{b}$  MC events are suppressed by a factor 0.98 by the HLT2 double trigger line. Distributions shown in Figure A.1 to A.7 illustrate this effect. BV48 signal sample, MC special  $b\bar{b}$  and 2011 data are shown with and without the requirement of being selected by the HLT2 double trigger line.

There is a rather clear difference in the distribution of the number of tracks. It seems that events with a small number of tracks are less likely to be selected by the double trigger line. A study has been made to also directly compare online and offline candidates and it seems that offline candidates are often reconstructed with less tracks than the online ones. This can be due to different settings of track quality cuts or by differences in clone cuts. It is clear that the track definitions are rather different in both contexts.

A strategy to better understand this unusual behavior would be to re-run the trigger software to bring light on the cut(s) responsible for this discrepancy. The effect of the rather complicated trigger selection cannot be revealed by a single simple explanation. For example, it has not been possible to explain this issue by simply looking at the track with the smallest transverse momentum used by the vertex reconstruction to see if, for example, this track is absent in the trigger context, or gives insufficient transverse momentum to the vertex for it to be selected.

On the bright side, it has been found that the double displaced vertices trigger selection is

## Appendix A. Appendix

efficient to significantly reduce the  $b\bar{b}$  background while keeping a good signal rate. Moreover, the normalization of events, based on the hypothesis of pure  $b\bar{b}$  background is coherent with what is observed in the data, as show in Table 4.8.

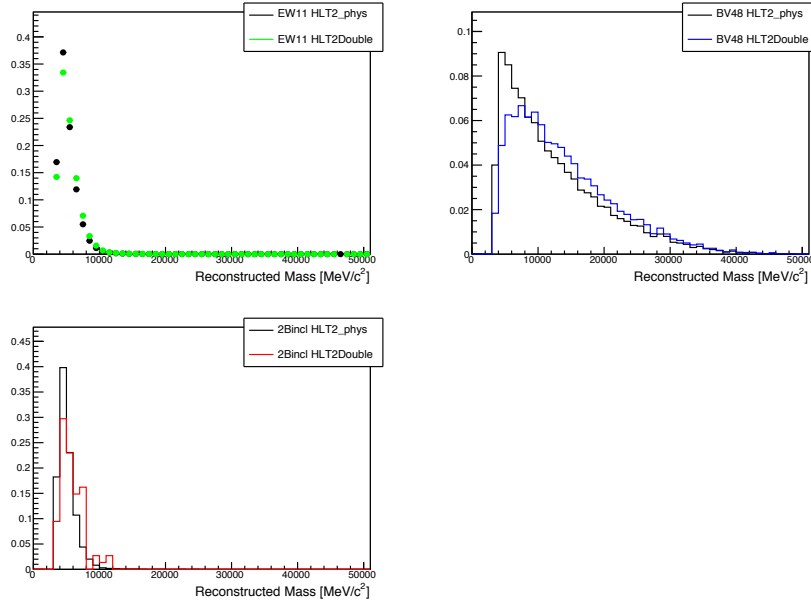


Figure A.1: Mass of the reconstructed  $\text{LLP}$  for (top left) 2011 data events, (top right) BV48 events and (bottom left) special MC  $b\bar{b}$ . Difference between events selected by any HLT2 physical trigger line (HLT2\_phys) and events selected by the HLT2 double lines are illustrated. The distributions contain events selected by the double displaced vertex stripping line and are normalized to unity.

## A.1. HLT2 Double line discussion

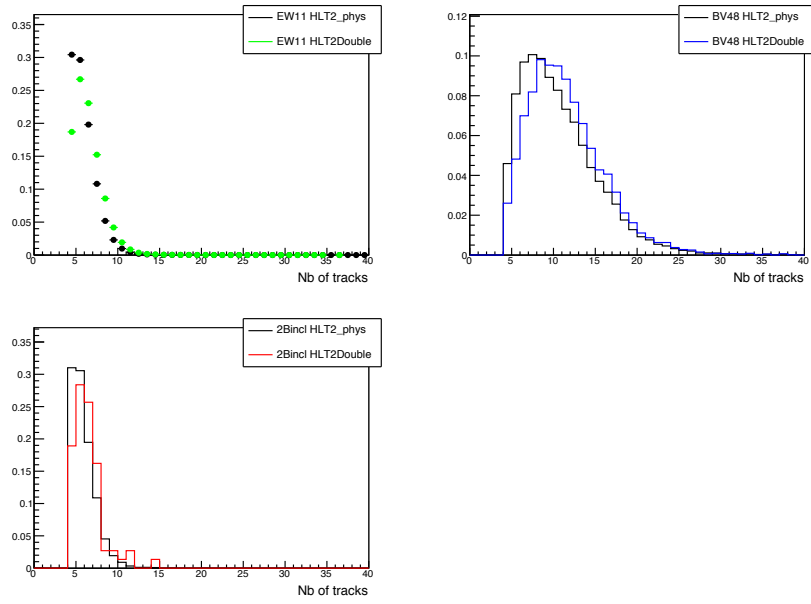


Figure A.2: Same as in Figure A.1 for the number of tracks of the reconstructed LLP for (top left) 2011 data events, (top right) BV48 events and (bottom left) special MC  $b\bar{b}$ .

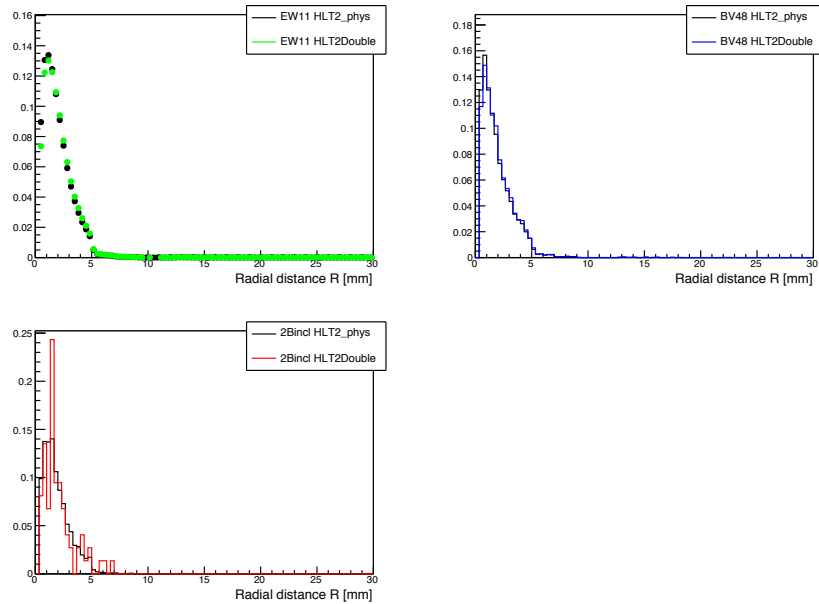


Figure A.3: Same as in Figure A.1 for the radial distance to the beam line of the reconstructed LLP for (top left) 2011 data events, (top right) BV48 events and (bottom left) special MC  $b\bar{b}$ .

## Appendix A. Appendix

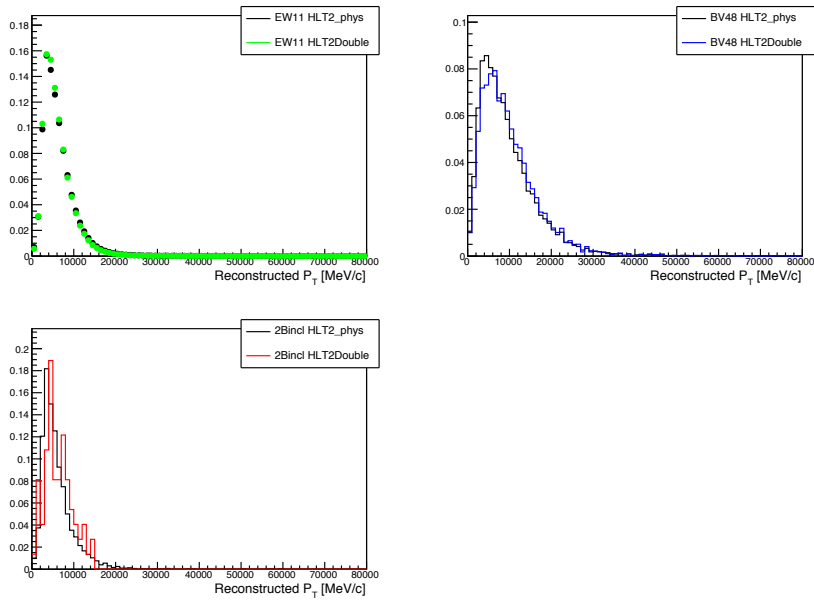


Figure A.4: Same as in Figure A.1 for the transverse momentum of the reconstructed LLP for (top left) 2011 data events, (top right) BV48 events and (bottom left) special MC  $b\bar{b}$ .

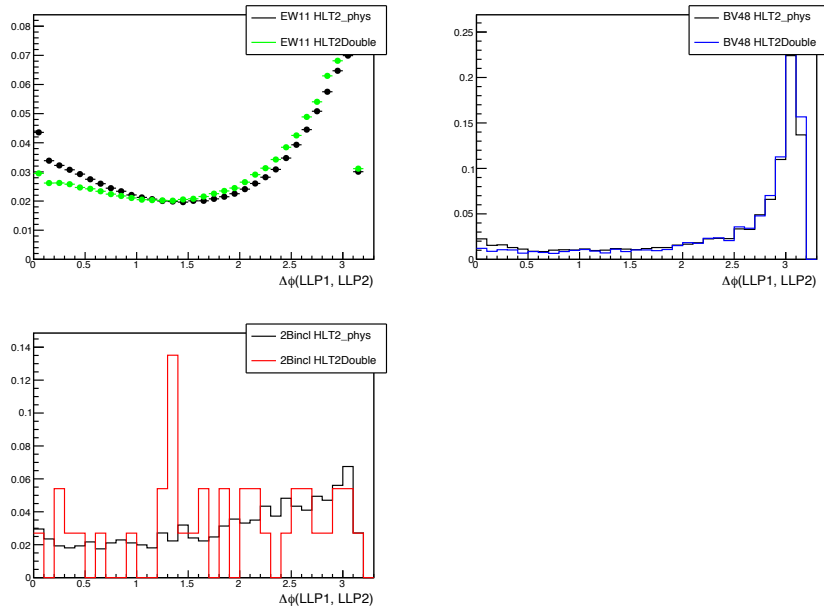


Figure A.5: Same as in Figure A.1 for the  $\Delta\phi$  angle between the pair of reconstructed LLPs for (top left) 2011 data events, (top right) BV48 events and (bottom left) special MC  $b\bar{b}$ .



## A.1. HLT2 Double line discussion

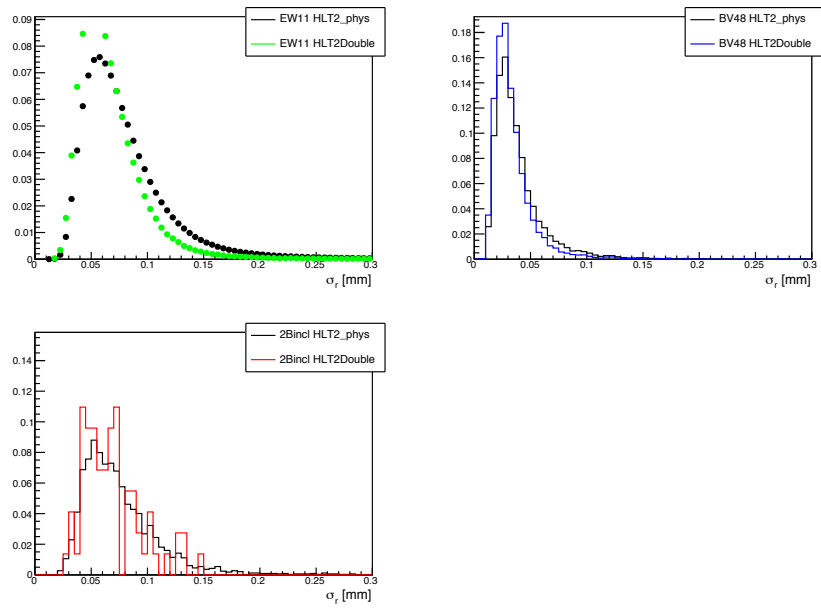


Figure A.6: Same as in Figure A.1 for the vertex position error in  $r$  of the reconstructed LLP for (top left) 2011 data events, (top right) BV48 events and (bottom left) special MC  $b\bar{b}$ .

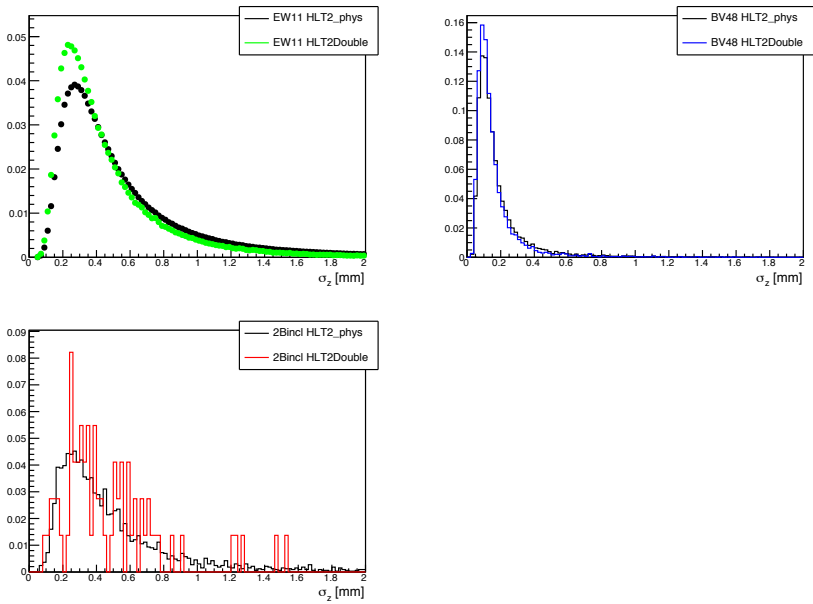


Figure A.7: Same as in Figure A.1 for the vertex position error in  $z$  of the reconstructed LLP for (top left) 2011 data events, (top right) BV48 events and (bottom left) special MC  $b\bar{b}$ .



# Bibliography

- [1] Neal Gauvin. *Search for Higgs Bosons Decaying into Long-Lived Exotic Particles in the LHCb Experiment*. PhD thesis, Ecole Polytechnique Federale Lausanne. CERN-THESIS-2011-012.
- [2] J. Beringer et al. (Particle Data Group). Review of particle physics. *Phys. Rev. D*, 86:010001, 2012, and 2013 partial update for the 2014 edition.
- [3] R. Oerter. *The theory of almost everything: The standard model, the unsung triumph of modern physics*. 2006.
- [4] Edward Witten. *Introduction to Supersymmetry*. 1983.
- [5] R. Barbier, C. Berat, M. Besancon, M. Chemtob, A. Deandrea, et al. R-parity violating supersymmetry. *Phys.Rept.*, 420:1–202, 2005.
- [6] Stephen P. Martin. *A Supersymmetry Primer*. xx, 1997.
- [7] Peter W. Graham, David E. Kaplan, Surjeet Rajendran, and Prashant Saraswat. Displaced Supersymmetry. *JHEP*, 1207:149, 2012.
- [8] Matthew J. Strassler and Kathryn M. Zurek. Echoes of a hidden valley at hadron colliders. *Phys. Lett.*, B651:374–379, 2007.
- [9] Matthew J. Strassler and Kathryn M. Zurek. Discovering the Higgs through highly-displaced vertices. *Phys. Lett.*, B661:263–267, 2008.
- [10] CMS Collaboration. Search for long-lived neutral particles decaying to dijets. 2013.
- [11] The LHCb Collaboration. The lhcb detector at the lhc. *Journal of Instrumentation*, 3(08):S08005, 2008.
- [12] Pierre Jaton. *Recherche directe à LHCb du boson de Higgs en production associée et contribution au développement du nouveau trajectographe à fibres scintillantes*. PhD thesis, Ecole Polytechnique Federale Lausanne, 2013. Thèse N°5900.
- [13] R. Hierk, M. Merk, M. Needham, and R. Van der Eijk. Performance of the LHCb 00 track fitting software. 2000.

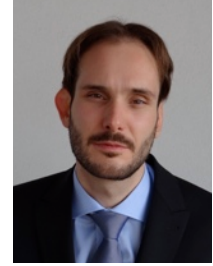
## Bibliography

---

- [14] Torbjörn Sjöstrand, Stephen Mrenna, and Peter Skands. PYTHIA 6.4 Physics and manual. *JHEP*, 05:026, 2006.
- [15] S. Agostinelli et al. GEANT4: A simulation toolkit. *Nucl. Instrum. Meth.*, A506:250, 2003.
- [16] Search for Higgs-like bosons decaying into long-lived exotic particles, Jun 2012. Linked to LHCb-ANA-2012-038.
- [17] Neal Gauvin. *Searching for a Supersymmetric Higgs Boson through displaced Decay Vertices in LHCb*. PhD thesis, Ecole Polytechnique Federale Lausanne, 2007. CERN-THESIS-2007-038.
- [18] Neal Gauvin, Aurelio Bay, Bastien Muster, Julien Rouvinet, Stephane Tourneur, Victor Coco, and Veerle Heijne. Search for (Higgs-like) bosons decaying into long-lived exotic particles. Jun 2012. Linked to LHCb-CONF-2012-014.
- [19] M Kucharczyk, P Morawski, and M Witek. Updated Primary Vertex Reconstruction. Technical Report LHCb-INT-2012-006. CERN-LHCb-INT-2012-006, CERN, Geneva, Feb 2012.
- [20] R. Aaij et al. Measurement of  $J/\psi$  production in  $pp$  collisions at  $\sqrt{s} = 7$  TeV. *Eur. Phys. J.*, C71:1645, 2011.
- [21] R. Aaij et al. Measurement of  $\sigma(pp \rightarrow b\bar{b}X)$  at  $\sqrt{s} = 7$  TeV in the forward region. *Phys. Lett.*, B694:209–216, 2010.
- [22] B. Souza de Paula. Studies on Systematic Effects of the Trigger on Flavour Tagging at the Generator Level. 2009.
- [23] Roel Aaij and Johannes Albrecht. Muon triggers in the High Level Trigger of LHCb. (2011) LHCb-PUB-2011-017, CERN-LHCb-PUB-2011-017.
- [24] Wouter Verkerke and David P. Kirkby. The RooFit toolkit for data modeling. *eConf*, C0303241:MOLT007, 2003.
- [25] Andreas Hocker, J. Stelzer, F. Tegenfeldt, H. Voss, K. Voss, et al. TMVA - Toolkit for Multivariate Data Analysis. *PoS*, ACAT:040, 2007.

# Julien Rouvinet

28 years old, swiss citizen, single  
Ch. de Champ-fleuri 18  
1022 Chavannes-Près-Renens  
Mobile: +41 79 626 49 39  
email: [julien.rouvinet@gmail.com](mailto:julien.rouvinet@gmail.com)



## EDUCATION

**2010-2014 Ph.D in Physics**, Ecole polytechnique Fédérale de Lausanne (EPFL) and CERN

- **Particle physics research** at CERN
- Senior teaching assistant
- Conferences and workshops across Europe and the US

**Summer 2012 Summer School at SLAC** (Stanford SSI 2012, CA)

- Lectures and conferences about various new theoretical and experimental results in particle physics

**2004-2010 Master in Sciences: Physics Engineer, EPFL**

- Master in particle physics, quantum physics, statistical physics and general relativity
- Bachelor in general physics

## EXPERIENCE

**2010-2014 Ph.D thesis** at EPFL in the Laboratory of High Energy Physics and CERN

- **Large data set analysis** with complex statistical and computational methods to determine signal significance, background estimation and rejection. Limit setting on production cross sections of new fundamental particles predicted by models beyond the Standard Model of particle physics
- Presentation of results in international conferences
- **Development, tests and characterization** of a new particle detection device using scintillating fibers. Measurement of detection efficiency and tracking resolution
- Work experience in an **international environment** at Cern within a team of research workers in a large community of people

**2012-2013 Vice-president** of the Musical association at EPFL

- Organization of events such as concerts, management of equipment (music rehearsal room shared by more than 60 people), accounting

**2005-2013 Various assistantships** at EPFL

- Teaching duties covering a large range of topics at the Bachelor and Master levels

## COMPETENCES

### Languages

- French: mother tongue
- English: full professional proficiency, C1
- German: high school level

### Computing skills

- C/C++, Python, Fortran, LaTeX, Root, RooFit, Matlab and Mathematica (basics)
- MacOs, Linux and Windows environments, MS Office
- Experience with large computational facilities (Grid computing at Cern)

## MISCELLANEOUS

Driving license, certified scuba diver, tennis, badminton, classical and rock guitar player, no military service obligation